

SYNTHESIS AND CHARACTERIZATION  
OF MULTIFUNCTIONAL OXIDES FOR  
FORCE AND GAS SENSORS

by

VANEET SHARMA

Presented to the Faculty of the Graduate School of  
The University of Texas at Arlington in Partial Fulfillment  
of the Requirements  
for the Degree of

MASTER OF SCIENCE IN MATERIALS SCIENCE AND ENGINEERING

THE UNIVERSITY OF TEXAS AT ARLINGTON

May 2007

Copyright © by Vaneet Sharma 2007

All Rights Reserved

DEDICATED TO MY PARENTS

MADHU AND JAGDISH

## ACKNOWLEDGEMENTS

I wish to express my sincere gratitude and thanks to my advisor Dr. Shashank Priya for giving me an opportunity of doing research under his guidance. This research is a result of his consistent motivation and guidance. I would also like to express my thanks to Dr. Ali. R. Koymen, whose invaluable support during this research made it a success, and also Maria Hossu for spending her invaluable time for the magnetic measurements.

I sincerely thank Dr. Efstathios Meletis, our chair, for reviewing my thesis work and being a committee member, and also providing us with all necessities in the department. I would also like to thank Dr. Jiechao Jiang for his invaluable and expert guidance in the TEM analysis for my samples, which helped me in understanding a new phenomenon in greater detail. I express my gratitude to all the professors and the department staff for offering their support whenever required, especially our secretaries, Jennifer Standlee and Donna Woodhead for helping me with ordering research supplies and helping me with my academic paperwork.

I appreciate the help of my colleagues and all the friends who motivated me and supported me during my thesis work. I express my thanks to Mr. Rashed Islam, my colleague who taught me from beginning the complete ceramic processing and helped me whenever needed. I thank Mr. Manan Goel, for his consistent support during my entire student career.



Finally I express my heartiest thanks to my parents, my brother and my sister for their love and affection that inspired me to go for higher studies.

December 7, 2006

## ABSTRACT

### SYNTHESIS AND CHARACTERIZATION OF MULTIFUNCTIONAL OXIDES FOR FORCE AND GAS SENSORS

Publication No. \_\_\_\_\_

Vaneet Sharma, M.S.

The University of Texas at Arlington, 2007

Supervising Professor: Shashank Priya

In this research work, the piezoresistivity phenomena in multifunctional oxides of  $\text{La}_{0.8}\text{Sr}_{0.2}\text{MnO}_3$  (LSMO) and composites of  $\text{LSMO}-(\text{Ce}_{0.12}\text{Zr}_{0.88})\text{O}_2$  have been investigated for force sensor application in harsh environments including automobile and aerospace industry. The composite material was tailored to have surface nanoporosity for developing a gas sensor based on difference in oxygen ion conductivity such that the same material can act as force and gas sensor. In automobile and aerospace industry, there is a need of material with high mechanical strength

and multi sensing capabilities. The inherent sensing capabilities allow the material to be implemented in variety of platforms.

Previously, LSMO polycrystalline ceramics have been studied as a cathode material in solid oxide fuel cells (SOFC) [1-4]. Owing to its colossal magnetoresistance properties, this material has also been extensively studied for use in magnetic read heads and magnetic memory devices [5-7]. Significant research has been conducted to further improve the magnetoresistive properties of this material by using doping elements [8-10]. This research invokes some of the results from these prior studies. Recently, the piezoresistivity phenomenon in LSMO has also been reported. In the present research, this property has been investigated in detail and various strategies have been adapted to improve its magnitude including the effect of doping elements.

Trivalent  $\text{Bi}^{3+}$  and monovalent  $\text{Li}^+$  ions were selected as dopants for substitution on La-sites while pentavalent  $\text{Nb}^{5+}$  and divalent  $\text{Cu}^{2+}$  ions were selected for substitution on Mn-sites. The effect of doping concentration on piezoresistivity, electrical properties, magnetic properties and microstructure was characterized. Doped compositions showed improvement in the piezoresistive coefficient as compared to the pure LSMO. The Li doped ceramics were found to exhibit -1.0% change in electrical resistivity, 4 mol% Bi and 6 mol% Bi modified compositions showed a change of -1.8 and -2.4% respectively at 19.2 MPa uniaxial stress [11]. The change in resistivity was found to be in the opposite direction compared to that of pure LSMO. The  $\text{Cu}^{2+}$  ions in low concentration range of 2 mol% did not show any significant enhancement in the piezoresistive properties of LSMO. The  $\text{Nb}^{5+}$  ions were found to have a remarkable

effect on piezoresistive property of LSMO. A giant increase in piezoresistivity was observed for 5 mol% Nb modified LSMO with the total change in electrical resistivity of +3.0% at 19.2 MPa uniaxial stress <sup>[12]</sup>.

Nb-modified LSMO was selected as the force sensor material. A miniature force sensor prototype for demonstrating the force sensing capability of the Nb modified composition was designed, fabricated and characterized. The sensor exhibited maximum output voltage response of 4 mVdc at applied force of 480 N. In order to improve the mechanical strength of this material a composite of ceria stabilized zirconia and Nb-LSMO was synthesized. The mechanical characteristics and piezoresistive properties of the composite were studied. The results showed unstable resistive behavior under stress for the composite material. More investigation is required to optimize the performance of the composite.

Next, the synthesis conditions of the LSMO – ceria – zirconia composites were optimized to achieve a surface nanoporous network in order to make this material suitable for oxygen gas sensor <sup>[13]</sup>. The approach was based upon the strain assisted self assembly achieved through the monoclinic – tetragonal phase transformation. The average diameter of the pores was found to be in the range of 150 – 200 nm. The pore distribution was quite periodic with an average spacing between pores around 50 – 150 nm. This nanoporous surface network was found to exist only on the surface of the material and the porous layer was found to be around 100 nm thick. This material was used to design an oxygen sensor. The sensor data was not very encouraging due to poor oxygen ion conduction.

## TABLE OF CONTENTS

ACKNOWLEDGEMENTS .....	iv
ABSTRACT .....	vi
LIST OF ILLUSTRATIONS .....	xiv
LIST OF TABLES .....	xxii
Chapter	
1. OBJECTIVE OF THIS RESEARCH .....	1
2. INTRODUCTION .....	2
2.1 Piezoresistance.....	2
2.1.1 Definition and history.....	2
2.1.2 Mathematical description.....	3
2.1.3 Effect of symmetry and piezoresistance coefficients.....	4
2.1.4 Piezoresistivity in various materials .....	6
2.2 Lanthanum strontium manganite .....	10
2.2.1 Introduction.....	10
2.2.2 Crystal structure .....	11
2.2.3 Phase diagram .....	11
2.2.4 Magnetic properties – Colossal magnetoresistance .....	13
2.2.5 Electrical properties – piezoresistance.....	14

3. MATERIALS SYNTHESIS AND CHARACTERIZATION .....	21
3.1 Material characterization techniques.....	21
3.2 Experimental procedure .....	22
3.2.1 Ceramic powder processing.....	22
3.2.1.1 Stoichiometric calculations .....	22
3.2.1.2 Powder mixing .....	23
3.2.1.3 Calcination.....	23
3.2.1.4 Sintering .....	24
3.2.2 Sample preparation .....	24
3.2.3 Piezoresistivity measurement technique .....	25
4. PIEZORESISTIVITY IN PURE AND MODIFIED $\text{La}_{0.8}\text{Sr}_{0.2}\text{MnO}_3$ BULK POLYCRYSTALLINE CERAMICS.....	28
4.1 Pure Lanthanum Strontium Manganite .....	28
4.1.1 Crystal structure and phase determination .....	28
4.1.2 Microstructures .....	30
4.1.3 Magnetic properties.....	30
4.1.4 Piezoresistivity .....	34
4.2 Effect of A-site dopants.....	34
4.2.1 Effect of lithium .....	34
4.2.1.1 Crystal structure and phase determination .....	34
4.2.1.2 Microstructures.....	36
4.2.1.3 Magnetic properties .....	36

4.2.1.4 Piezoresistivity .....	40
4.2.2 Effect of bismuth.....	40
4.2.2.1 Crystal structure and phase determination .....	40
4.2.2.2 Microstructures.....	42
4.2.2.3 Magnetic properties.....	42
4.2.2.4 Piezoresistivity .....	47
4.3 Effect of B-site dopants.....	50
4.3.1 Effect of copper.....	50
4.3.1.1 Crystal structure and phase determination .....	50
4.3.1.2 Microstructures.....	50
4.3.1.3 Magnetic properties.....	50
4.3.1.4 Piezoresistivity .....	55
4.3.2 Effect of niobium .....	55
4.3.2.1 Crystal structure and phase determination .....	55
4.3.2.2 Microstructures.....	59
4.3.2.3 Magnetic properties.....	62
4.3.2.4 Piezoresistivity .....	62
5. PIEZORESISTIVITY BEHAVIOR OF $\text{La}_{0.8}\text{Sr}_{0.2}\text{MnO}_3$ – PARTIALLY STABILIZED ZIRCONIA COMPOSITE.....	67
5.1 Mechanical properties of ceria stabilized $\text{ZrO}_2$ .....	67
5.2 Properties of $\text{La}_{0.8}\text{Sr}_{0.2}\text{MnO}_3$ – partially stabilized $\text{ZrO}_2$ composite.....	70
5.2.1 Mechanical properties.....	70

5.2.2 Microstructural properties.....	70
5.2.3 Piezoresistivity .....	71
5.2.4 Problems and success of the composite .....	72
6. MINIATURE FORCE SENSOR FOR AUTOMOBILE APPLICATIONS.....	76
6.1 Material selection .....	76
6.2 Force sensor design.....	76
6.3 Force sensor characterization.....	77
7. NANOPOROUS MATERIAL FOR OXYGEN GAS SENSOR.....	81
7.1 Phase transformation as self assembly technique .....	81
7.2 Experimental procedure .....	82
7.3 Self- assembled nanoporous surface network.....	83
7.4 Crystal structure and phase determination .....	87
7.5 Composition modifications .....	89
7.5.1 LSMO variation .....	89
7.5.2 Ceria variation.....	96
7.6 Oxygen gas sensor.....	96
7.6.1 Gas sensor design.....	96
7.6.2 Gas sensor working principle.....	103
7.6.3 Gas Sensor data.....	106
7.6.4 Discussion .....	106
8. CONCLUSION .....	107
9. FUTURE WORK .....	108



9.1 (Ba,Sr)TiO <sub>3</sub> – CoFe <sub>2</sub> O <sub>4</sub> composite for force sensor .....	108
9.2 Problems associated with LSMO-partially stabilized ZrO <sub>2</sub> composite.....	109
9.3 Force sensor design modifications .....	113
9.4 Oxygen gas sensor modifications.....	114
9.5 Carbon nanotube- LSMO – ZrO <sub>2</sub> multifunctional composites .....	114
9.6 Thin film La <sub>0.8</sub> Sr <sub>0.2</sub> MnO <sub>3</sub> force sensors .....	115
 Appendix	
A. AUTOMOTIVE FORCE AND GAS SENSOR INFORMATION .....	118
B. SILICON MEMS AS FORCE SENSORS .....	122
C. PIEZORESISTIVITY MEASUREMENT SYSTEM .....	127
D. ELECTRONIC COMPONENTS .....	131
E. CHEMICALS USED FROM ALFA AESAR.....	133
F. MULTIMETER AND ELECTROMETER.....	135
REFERENCES.....	138
BIOGRAPHICAL INFORMATION.....	144

## LIST OF ILLUSTRATIONS

Figure	Page
2.1. Piezoresistivity in semiconductor Si single crystals.....	7
2.2. Conduction mechanism in RuO <sub>2</sub> based metal-insulator-metal junctions .....	7
2.3. Piezoresistance and magnetoresistance in La <sub>0.8</sub> Sr <sub>0.2</sub> MnO <sub>3</sub> as a function of temperature. ....	9
2.4. Perovskite unit cell of La <sub>1-x</sub> Sr <sub>x</sub> MnO <sub>3</sub> .....	12
2.5. Effect of Sr amount on the a-axis parameter of La <sub>1-x</sub> Sr <sub>x</sub> MnO <sub>3</sub> . ....	12
2.6. Binary phase diagram of the LaMnO <sub>3</sub> - SrMnO <sub>3</sub> system. ....	15
2.7. Ternary phase diagram of the ZrO <sub>2</sub> – CeO <sub>2</sub> – LaO <sub>1.5</sub> system.....	16
2.8. Temperature dependence of resistivity in La <sub>1-x</sub> Sr <sub>x</sub> MnO <sub>3</sub> with varying Sr amounts... ..	16
2.9. Temperature dependence of resistivity in La <sub>1-x</sub> Sr <sub>x</sub> MnO <sub>3</sub> under varying magnetic field.....	17
2.10. Magnetic phase diagram of La <sub>1-x</sub> Sr <sub>x</sub> MnO <sub>3</sub> .....	17
2.11. (a) Uniaxial pressure dependence of piezoresistance and (b) magnetic field dependence of magnetoresistance in La <sub>1-x</sub> Sr <sub>x</sub> MnO <sub>3</sub> .....	19
2.12. Temperature dependence of resistivity in La <sub>1-x</sub> Sr <sub>x</sub> MnO <sub>3</sub> with external magnetic field and pressure.....	19
2.13. Effect of pressure on the Curie temperature of La <sub>1-x</sub> Sr <sub>x</sub> MnO <sub>3</sub> .....	20
2.14. Change in electrical resistivity of La <sub>0.8</sub> Sr <sub>0.2</sub> MnO <sub>3</sub> with uniaxial stress. ....	20
3.1. Schematic diagram of the samples prepared for piezoresistive measurement.....	27

3.2.	(a) Sample holder design and sample under test and (b) test set-up using Instron® microtester for piezoresistivity measurements. ....	27
4.1.	X-ray diffraction patterns of pure $\text{La}_{0.8}\text{Sr}_{0.2}\text{MnO}_3$ calcined at different temperatures.....	29
4.2.	X-ray diffraction patterns of pure $\text{La}_{0.8}\text{Sr}_{0.2}\text{MnO}_3$ sintered at different temperatures.....	29
4.3.	SEM micrographs of pure $\text{La}_{0.8}\text{Sr}_{0.2}\text{MnO}_3$ sintered at different temperatures (a) $1300^\circ\text{C}$ , 4 hrs, (b) $1400^\circ\text{C}$ , 4 hrs. ....	31
4.4.	SEM micrographs of (a) $\text{La}_{0.75}\text{Sr}_{0.25}\text{MnO}_3$ , and (b) $\text{La}_{0.85}\text{Sr}_{0.15}\text{MnO}_3$ sintered at $1400^\circ\text{C}$ for 6 hrs. ....	31
4.5.	SEM micrographs of pure $\text{La}_{0.8}\text{Sr}_{0.2}\text{MnO}_3$ sintered at (a) $1400^\circ\text{C}$ , 6 hrs, (b) $1450^\circ\text{C}$ , 6 hrs.....	32
4.6.	(a) Temperature dependence of magnetization, and (b) room temperature magnetic hysteresis loop for pure $\text{La}_{0.8}\text{Sr}_{0.2}\text{MnO}_3$ .....	32
4.7.	Effect of pressing time on the XRD peaks of $\text{La}_{0.8}\text{Sr}_{0.2}\text{MnO}_3$ . ....	33
4.8.	Peak shifts of (020) and ( $\bar{2}$ 00) reflections of $\text{La}_{0.8}\text{Sr}_{0.2}\text{MnO}_3$ with pressing time. ....	33
4.9.	Piezoresistivity in pure $\text{La}_{0.8}\text{Sr}_{0.2}\text{MnO}_3$ . ....	35
4.10.	X-ray diffraction patterns of calcined powders of Li-modified $\text{La}_{0.8}\text{Sr}_{0.2}\text{MnO}_3$ compositions. ....	37
4.11.	X-ray diffraction patterns for Li-modified $\text{La}_{0.8}\text{Sr}_{0.2}\text{MnO}_3$ compositions sintered at $1400^\circ\text{C}$ for 6 hrs. ....	37
4.12.	SEM micrographs of 2 mol% Li modified $\text{La}_{0.8}\text{Sr}_{0.2}\text{MnO}_3$ sintered at $1400^\circ\text{C}$ for 6 hrs, (a) at 1 kX, (b) at 5 kX. ....	38
4.13.	SEM micrographs of 4mol% Li modified $\text{La}_{0.8}\text{Sr}_{0.2}\text{MnO}_3$ sintered at $1400^\circ\text{C}$ for 6 hrs, (a) at 1 kX, (b) at 5 kX.....	38
4.14.	SEM micrographs of 6 mol% Li modified $\text{La}_{0.8}\text{Sr}_{0.2}\text{MnO}_3$ sintered at $1400^\circ\text{C}$ for 6 hrs, (a) at 1 kX, (b) at 5 kX. ....	39

4.15.	Temperature dependence of magnetization in lithium modified $\text{La}_{0.8}\text{Sr}_{0.2}\text{MnO}_3$ with varying Li concentration.....	39
4.16.	Room temperature magnetic hysteresis for lithium modified $\text{La}_{0.8}\text{Sr}_{0.2}\text{MnO}_3$ with varying Li concentration..	41
4.17.	Piezoresistivity in lithium modified $\text{La}_{0.8}\text{Sr}_{0.2}\text{MnO}_3$ compositions.....	41
4.18.	X-ray diffraction patterns of Bi modified $\text{La}_{0.8}\text{Sr}_{0.2}\text{MnO}_3$ compositions. ....	43
4.19.	X-ray diffraction patterns of Bi modified $\text{La}_{0.8}\text{Sr}_{0.2}\text{MnO}_3$ sintered compositions .....	43
4.20.	SEM micrographs of 2 mol% Bi modified $\text{La}_{0.8}\text{Sr}_{0.2}\text{MnO}_3$ after sintering at $1400^\circ\text{C}$ for 6 hrs, (a) at 1 kX, (b) at 5 kX. ....	44
4.21.	SEM micrographs of 2 mol% Bi modified $\text{La}_{0.8}\text{Sr}_{0.2}\text{MnO}_3$ after sintering at $1350^\circ\text{C}$ for 6 hrs, (a) at 1 kX, (b) at 5 kX.....	44
4.22.	SEM micrographs of 2 mol% Bi modified $\text{La}_{0.8}\text{Sr}_{0.2}\text{MnO}_3$ after sintering at $1300^\circ\text{C}$ for 6 hrs, (a) at 1 kX, (b) at 5 kX.....	45
4.23.	SEM micrographs of 4 mol% Bi modified $\text{La}_{0.8}\text{Sr}_{0.2}\text{MnO}_3$ after sintering at $1400^\circ\text{C}$ for 6 hrs, (a) at 500 X, (b) at 1 kX.....	45
4.24.	SEM micrographs of 6 mol% Bi modified $\text{La}_{0.8}\text{Sr}_{0.2}\text{MnO}_3$ after sintering at $1400^\circ\text{C}$ for 6 hrs, (a) at 500 X, (b) at 1 kX.....	46
4.25.	Temperature dependence of magnetization in bismuth modified $\text{La}_{0.8}\text{Sr}_{0.2}\text{MnO}_3$ compositions .....	48
4.26.	Room temperature magnetic hysteresis loops for bismuth modified $\text{La}_{0.8}\text{Sr}_{0.2}\text{MnO}_3$ compositions. ....	48
4.27.	Piezoresistivity in Bi modified $\text{La}_{0.8}\text{Sr}_{0.2}\text{MnO}_3$ compositions.....	49
4.28.	X-ray diffraction pattern for 2 mol% Cu modified $\text{La}_{0.8}\text{Sr}_{0.2}\text{MnO}_3$ after calcination at $1025^\circ\text{C}$ for 4 hrs. ....	51
4.29.	X-ray diffraction pattern for 2 mol% Cu modified $\text{La}_{0.8}\text{Sr}_{0.2}\text{MnO}_3$ after sintering at $1400^\circ\text{C}$ for 6 hrs.....	51
4.30.	SEM micrographs of 2 mol% Cu modified $\text{La}_{0.8}\text{Sr}_{0.2}\text{MnO}_3$ after sintering at $1200^\circ\text{C}$ for 4 hrs, (a) at 1 kX, (b) at 5 kX. ....	52

4.31.	SEM micrographs of 2 mol% Cu modified $\text{La}_{0.8}\text{Sr}_{0.2}\text{MnO}_3$ after sintering at 1400°C for 4 hrs pressed at (a) 30 ksi and (b) 40 ksi .....	52
4.32.	SEM micrographs of 2 mol% Cu modified $\text{La}_{0.8}\text{Sr}_{0.2}\text{MnO}_3$ after sintering at 1400°C for 6 hrs, (a) at 5 kX and (b) 15 kX.....	53
4.33.	Temperature dependence of magnetization in 2 mol% Cu modified $\text{La}_{0.8}\text{Sr}_{0.2}\text{MnO}_3$ . .....	53
4.34.	Room temperature magnetic hysteresis loops for 2 mol% Cu modified $\text{La}_{0.8}\text{Sr}_{0.2}\text{MnO}_3$ .....	54
4.35.	Piezoresistivity in 2 mol% Cu modified $\text{La}_{0.8}\text{Sr}_{0.2}\text{MnO}_3$ .....	54
4.36.	X-ray diffraction patterns of calcined powders of Nb modified $\text{La}_{0.8}\text{Sr}_{0.2}\text{MnO}_3$ compositions. ....	56
4.37.	X-ray diffraction patterns of sintered samples of Nb modified $\text{La}_{0.8}\text{Sr}_{0.2}\text{MnO}_3$ compositions after sintering at 1400°C for 6 hrs.....	56
4.38.	Peak shifts in the (020) and ( $\bar{2}$ 00) reflections with B-site modification .....	57
4.39.	Peak shifts in the (022) and (202) reflections with B-site modification.....	57
4.40.	Effect of pressing time on the XRD peaks of $\text{La}_{0.8}\text{Sr}_{0.2}\text{Nb}_{0.05}\text{Mn}_{0.95}\text{O}_3$ at 15MPa uniaxial pressure. ....	58
4.41.	Peak shifts in the (020) reflections of $\text{La}_{0.8}\text{Sr}_{0.2}\text{Nb}_{0.05}\text{Mn}_{0.95}\text{O}_3$ with pressing time at 15 MPa uniaxial pressure. ....	58
4.42.	SEM micrographs for 2 mol% Nb modified $\text{La}_{0.8}\text{Sr}_{0.2}\text{MnO}_3$ after sintering at 1300°C for 4 hrs pressed at (a) 30 ksi and (b) 40 ksi, and 1400°C for 4 hrs pressed at (c) 30 ksi and, (d) 40 ksi. ....	60
4.43.	SEM micrographs of 2 mol% Nb modified composition sintered at 1400°C 6 hrs after pressing at (a) 30 ksi and (b) 40 ksi CIP pressure .....	60
4.44.	SEM micrographs for 5 mol%Nb modified $\text{La}_{0.8}\text{Sr}_{0.2}\text{MnO}_3$ after sintering at 1300°C for 4 hrs at (a) 30 ksi, (b) 40 ksi and 1400°C for 4 hrs pressed at (c) 30 ksi, (d) 40 ksi CIP pressure .....	61

4.45.	SEM micrographs of 5 mol% Nb modified composition sintered at 1400°C for 6 hrs and pressed at (a) 30 ksi and (b) 40 ksi CIP pressure.....	61
4.46.	Temperature dependence of magnetization for Nb modified $\text{La}_{0.8}\text{Sr}_{0.2}\text{MnO}_3$ compositions.....	64
4.47.	Room temperature magnetic hysteresis loops for Nb modified $\text{La}_{0.8}\text{Sr}_{0.2}\text{MnO}_3$ compositions.....	65
4.48.	Piezoresistivity in Nb-modified $\text{La}_{0.8}\text{Sr}_{0.2}\text{MnO}_3$ ceramics at different concentrations of Nb.....	65
4.49.	Comparison of the resistivity values after A and B site modification in $\text{La}_{0.8}\text{Sr}_{0.2}\text{MnO}_3$ ceramics.....	66
4.50.	Comparison of the piezoresistive behavior after A and B site modification in $\text{La}_{0.8}\text{Sr}_{0.2}\text{MnO}_3$ ceramics.....	66
5.1.	12 mol% $\text{CeO}_2$ stabilized $\text{ZrO}_2$ , after sintering at (a) 1350°C and (b) 1400°C for 6 hrs.....	68
5.2.	X-ray diffraction pattern for partially stabilized zirconia, showing a tetragonal structure.....	68
5.3.	Variation of mechanical properties with $\text{CeO}_2$ concentration in $\text{CeO}_2$ stabilized $\text{ZrO}_2$ ceramics.....	69
5.4.	A comparison of the stress-strain behavior of pure LSMO, partially stabilized zirconia and LSMO- $\text{ZrO}_2$ composite.....	69
5.5.	SEM micrographs of the LSMO- partially stabilized composite sintered at 1300°C for 6 hrs at (a) 1 kX and (b) 10 kX respectively.....	73
5.6.	X-ray diffraction pattern of the composite material with and without porous surface layer.....	73
5.7.	Piezoresistivity in $\text{La}_{0.8}\text{Sr}_{0.2}\text{MnO}_3$ – partially stabilized $\text{ZrO}_2$ composite.....	74
5.8.	Piezoresistivity in $\text{La}_{0.8}\text{Sr}_{0.2}\text{Nb}_{0.05}\text{Mn}_{0.95}\text{O}_3$ – partially stabilized $\text{ZrO}_2$ composite.....	74
6.1.	Schematics of the force sensing element.....	78

6.2.	Wheatstone bridge arrangement used in the force sensor circuit. ....	78
6.3.	Force sensor design (top view). ....	79
6.4.	Schematic construction of the force sensor prototype (internal view). ....	79
6.5.	Picture of the miniature force sensor prototype. ....	80
6.6.	Voltage output characteristics of the miniature force sensor prototype. ....	80
7.1.	Self assembled nanoporous network in the $\text{La}_{0.8}\text{Sr}_{0.2}\text{MnO}_3$ – partially stabilized $\text{ZrO}_2$ composite. (a) at 5 kX (b) pore morphology at 100 kX. (c) diameter of the pores (d) thickness of the porous layer. ....	84
7.2.	(a) Fractured cross section and (b) cross section after polishing and etching .....	85
7.3.	TEM images of the surface nanoporous layer in LSMO- $\text{ZrO}_2$ composite, (a) and (b).. ....	85
7.4.	TEM images of the bulk of the LSMO- $\text{ZrO}_2$ composite. ....	86
7.5.	SEM micrograph of a TEM sample prepared after polishing (a) and (b). ....	86
7.6.	Nanoporous composite after varying the sintering temperature (a) 1300°C, (b)1350°C, (c) 1400°C, and (d)1450°C for 6 hrs respectively ...	88
7.7.	X-ray diffraction results for samples with porous layer and after polishing off the layer. ....	90
7.8.	SAED patterns of (a) the grain boundary islands and (b) porous network regions. ....	90
7.9.	Elemental maps for 25wt% LSMO – ceria stabilized $\text{ZrO}_2$ .....	91
7.10.	SEM EDAX pattern for the island grain in LSMO- $\text{ZrO}_2$ nanoporous composite. ....	92
7.11.	SEM EDAX pattern for the porous region of LSMO- $\text{ZrO}_2$ nanoporous composite. ....	92
7.12.	SEM EDAX pattern for the grain boundary in the LSMO- $\text{ZrO}_2$ nanoporous composite. ....	93

7.13.	TEM - EDX analysis on the island grains .....	93
7.14.	TEM- EDX on the porous network region .....	94
7.15.	(a) Temperature dependence of magnetization, and (b) room temperature magnetic hysteresis of the composite with and without porous layer.....	94
7.16.	XRD patterns of $\text{La}_{0.8}\text{Sr}_{0.2}\text{MnO}_3 - (\text{Ce}_{0.12}\text{Zr}_{0.88})\text{O}_2$ composite with varying LSMO content. ....	95
7.17.	Elemental maps for 35.8 mol% LSMO – $(\text{Ce}_{0.12}\text{Zr}_{0.88})\text{O}_2$ composite. ....	97
7.18.	Elemental maps for 5.8 mol% LSMO – $(\text{Ce}_{0.12}\text{Zr}_{0.88})\text{O}_2$ composite. ....	98
7.19.	SEM micrograph of the 5.83 mol% LSMO – $(\text{Ce}_{0.12}\text{Zr}_{0.88})\text{O}_2$ composite sintered at 1400°C for 6 hrs, (a) at 5 kX and (b) at 10 kX.....	99
7.20.	SEM micrograph of the 12 mol% LSMO – $(\text{Ce}_{0.12}\text{Zr}_{0.88})\text{O}_2$ composite sintered at 1400°C for 6 hrs, (a) at 5 kX and (b) at 15 kX .....	99
7.21.	SEM micrograph of the 15.66 mol% LSMO – $(\text{Ce}_{0.12}\text{Zr}_{0.88})\text{O}_2$ composite sintered at 1400°C for 6 hrs, (a) at 5 kX and (b) 15 kX.....	100
7.22.	SEM micrograph of the 17 mol% LSMO – $(\text{Ce}_{0.12}\text{Zr}_{0.88})\text{O}_2$ composite sintered at 1400°C for 6hrs, (a) at 5 kX and (b) 15 kX.....	100
7.23.	SEM micrograph of the 20 mol% LSMO – $(\text{Ce}_{0.12}\text{Zr}_{0.88})\text{O}_2$ composite sintered at 1400°C for 6 hrs, (a) 5 kX and (b) at 20 kX.....	101
7.24.	SEM micrograph of the 35.8 mol% LSMO – $(\text{Ce}_{0.12}\text{Zr}_{0.88})\text{O}_2$ composite sintered at 1400°C for 6 hrs, (a) at 5 kX and (b) at 10 kX.....	101
7.25.	SEM micrograph of the LSMO –10 mol% $\text{CeO}_2$ stabilized $\text{ZrO}_2$ composite, (a) at 5 kX and (b) at 10 kX. ....	102
7.26.	SEM micrograph of the LSMO – 4 mol% $\text{CeO}_2$ stabilized $\text{ZrO}_2$ composite, (a) at 5 kX and (b) at 10 kX.....	102
7.27.	Mechanism of oxygen ion conduction in the LSMO – partially stabilized $\text{ZrO}_2$ composite with a nanoporous surface layer. ....	104
7.28.	Voltage-current characteristics of a limiting-current type oxygen sensor.....	104



7.29.	Schematics of the oxygen gas sensor tested in this research work.....	105
9.1.	(a) La-doped (Br,Sr)TiO <sub>3</sub> after calcination at 1000°C for 2 hrs and (b) CoFe <sub>2</sub> O <sub>4</sub> after calcination at 1000°C for 6 hrs.....	110
9.2.	(a) and (b) Multilayered (Ba,Sr)TiO <sub>3</sub> – CoFe <sub>2</sub> O <sub>4</sub> composite co-sintered at 1300°C for 5 hrs.....	110
9.3.	Schematics of the multilayered (Ba,Sr)TiO <sub>3</sub> – CoFe <sub>2</sub> O <sub>4</sub> composite. ....	111
9.4.	(a) Magnetoelectric coefficient vs dc bias and (b) frequency for the BST – CF composite. ....	111
9.5.	(a) Dielectric loss vs temperature and (b) dielectric constant vs temperature curves for BST – CF multilayer composite at different frequencies.....	112
9.6.	Sample geometry modifications, (a) multilayered and (b) ring type structure. ....	116
9.7.	Oxygen sensor design with an internal volume.....	116
9.8.	Carbon-nanotube LSMO – ZrO <sub>2</sub> multifunctional composites.....	116
9.9.	Piezoresistive LSMO thin film force sensor design example. ....	117
B.1.	Piezoresistive polysilicon pressure sensor.....	125
B.2.	Capacitive (single crystal silicon) pressure sensor. ....	125
C.1.	Lab scale automatic piezoresistivity measurement system design.....	129
C.2.	Block diagram for the automatic piezoresistivity measurement system. ....	130
F.1.	Agilent 34410A 6½ digit, high performance digital multimeter.....	136
F.2.	KEITHLY Model 6517A Electrometer / High resistance meter.....	137

## LIST OF TABLES

Table	Page
1. Piezoresistive coefficients of various materials.....	9
2. The A-site and B-site modified compositions of LSMO .....	26
3. Ionic radii of various elements and their preferred lattice site .....	26
4. Relative density values of A-site modified LSMO ceramics. ....	46
5. Relative density values of B-site modified LSMO ceramics. ....	64
6. Response of the nanoporous surface layer composite oxygen sensor .....	105
7. Off-the-shelf force sensors available from various companies. ....	119
8. Force sensor design/ construction/principle information links.....	120
9. Commercially available automotive and other gas sensors.....	121
10. Worldwide growth for automotive silicon micromachined sensors (from Sullivan1993).....	126
11. Relative merits and demerits of capacitive and piezoresistive silicon pressure sensors. ....	126
12. List of electronic components for piezoresistive force sensors.....	132
13. List of chemicals obtained from Alfa Aesar.....	134

## CHAPTER 1

### OBJECTIVE OF THIS RESEARCH

The following are the main objectives of the present research work:

**Objective I:** To understand the piezoresistance mechanism in  $\text{La}_{0.8}\text{Sr}_{0.2}\text{MnO}_3$  bulk polycrystalline ceramics and to explore the effect of A-site and B-site doping on the piezoresistance behavior. The present research also aims to study the effect of compositional modulation, synthesis condition, concentration of the doping elements and La/Sr ratio on the piezoresistive, magnetic, and electrical properties of  $\text{La}_{0.8}\text{Sr}_{0.2}\text{MnO}_3$ .

**Objective II:** To synthesize a mechanically strong composite material exhibiting large piezoresistive coefficient and investigate its electrical and magnetic properties.

**Objective III:** To design and characterize a miniature force sensor for use in automobile environment using the aforementioned composite material.

**Objective IV:** Synthesis of a nano-porous surface layer in the composite material for obtaining oxygen gas sensing capability.

## CHAPTER 2

### INTRODUCTION

#### 2.1 Piezoresistance

##### *2.1.1 Definition and history*

Piezoresistivity is the linear coupling between mechanical stress and electrical resistivity of a material and is characterized by change in electrical resistivity with applied mechanical stress. Derived from the Greek word “*piezein*” which means to squeeze or press, and combined with “*resistivity*”, which is the inherent property of any material that provides an obstruction to the flow of electrical current in the material (“*specific resistance*”), the word “piezoresistance” or “piezoresistivity” has emerged as an important keyword in most force and pressure sensing applications today.

First discovered by Lord Kelvin in 1856, in metals like copper and iron where he observed that the electrical resistance of these metals changed under an applied external mechanical stress. This effect was attributed to the change in geometrical features of the metals. Later in 1954, Smith in Bell Labs, discovered piezoresistivity in semiconducting silicon and germanium <sup>[14]</sup>. It was found that in these materials the change in electrical resistance was not only due to the change in geometry, but also due to changes in the crystal lattice. As a consequence of this fact, the total change was enormous, as compared to normal metals. Piezoresistance has been observed in poly-

crystalline silicon, amorphous silicon, silicon carbide and single crystal silicon and these materials are currently used in MEMS based pressure sensors.

In 1959, Sauer, Flaschen and Hoesterey, at Bell Telephone Labs, reported an extremely large hydrostatic piezoresistive response of the order of (6450 Pa<sup>-1</sup>) in semiconducting, positive temperature coefficient of resistance (PTCR) (Ba,Sr)TiO<sub>3</sub> and (Pb,Ba)TiO<sub>3</sub> ceramics <sup>[15]</sup>. Later, piezoresistance effect was also discovered in Ruthenium Oxide (ReO<sub>2</sub>) based ‘Metal-Insulator-Metal’ (MIM) structures by Canali et al in 1980 <sup>[16]</sup>. Recently, piezoresistivity has also been reported in two extremely attractive forms of carbon: the hardest material on earth, diamond, in the form of thin films <sup>[17]</sup> and the so called “fourth allotrope of carbon”, the carbon nanotubes” <sup>[18]</sup>.

The constant search for the material with improved piezoresistance coefficient motivates the research on new class of materials. In the next section, the mathematical formulation for the piezoresistance is described to define the coefficients involved.

### 2.1.2 Mathematical description <sup>[19]</sup>

Electrical resistivity ( $\rho$ ) is a second rank polar tensor and is related to the applied electric field ( $E$ ) and resulting current density ( $J$ ) in the material through Ohm’s law as:

$$\mathbf{E}_i = \rho_{ij} \mathbf{J}_j \quad (1)$$

Where  $E_i$  and  $J_j$  being first ranked polar tensors. Piezoresistivity involves the linear and nonlinear relationships between electric field tensor  $E_i$ , electric current density  $J_j$ , and mechanical stress  $X_k$ . Using a McLaurin series expansion in terms of current density  $J_j$ , and mechanical stress  $X_k$  the change in electric field can be expressed as:

$$dE_i = \left( \frac{\partial E_i}{\partial J_j} \right) dJ_j + \left( \frac{\partial E_i}{\partial X_{kl}} \right) dX_{kl} + \frac{1}{2} \left( \frac{\partial^2 E_i}{\partial J_j \partial J_m} \right) dJ_j dJ_m + \frac{1}{2} \left( \frac{\partial^2 E_i}{\partial X_{kl} \partial X_{no}} \right) dX_{kl} dX_{no} \quad (2)$$

$$+ \left( \frac{\partial^2 E_i}{\partial J_j \partial X_{kl}} \right) dJ_j dX_{kl} + \dots$$

In this series expansion the term  $(\partial E_i / \partial J_j)$  represents electrical resistivity  $\rho_{ij}$ ,  $(\partial E_i / \partial X_{kl})$  represents the piezoelectric voltage coefficient,  $g_{ikl}$ ,  $(\partial^2 E_i / \partial J_j \partial J_m)$  is the change in electrical resistivity with current level or the non-linear resistivity,  $(\partial^2 E_i / \partial X_{kl} \partial X_{no})$  which is a fifth ranked tensor represents the stress dependence of the piezoelectric voltage coefficient or the non-linear piezoelectricity. The fifth term in the expansion above,  $(\partial^2 E_i / \partial J_j \partial X_{kl})$  is a fourth rank polar tensor and describes the dependence of electrical resistivity with mechanical stress. It represents the physical quantity, ‘piezoresistance’ which is the topic of interest in the present work.

For a centrosymmetric point group, all odd rank polar tensors should disappear, so as a result Eq. (2) reduces to:

$$dE_i = \rho_{ij} dJ_j + \pi_{ijkl} dJ_j dX_{kl} \quad (3)$$

On integration and rearranging, the change in resistivity under stress can be given as:

$$\Delta \rho_{ij} = \frac{E_i - \rho_{ij} J_j}{J_j} = \pi_{ijkl} X_{kl} \quad (4)$$

### 2.1.3 Effect of symmetry and piezoresistance coefficients <sup>[19]</sup>

For the piezoresistivity tensor  $\pi_{ijkl}$ ,  $i$  and  $j$  are not interchangeable and so are  $k$  and  $l$ , because the energy argument has to be satisfied. The piezoresistivity tensor symmetry is expressed as:

$$\pi_{ijkl} = \pi_{ijlk} = \pi_{jilk} = \pi_{jikl} \quad (5)$$

Using the symmetry conditions of Eq. (5), the number of independent coefficient in the piezoresistivity matrix reduces to 36 from 81. Using the Voigt reduced notation, the piezoresistance coefficient can be written in reduced form as:

$$\pi_{ijkl} = \pi_{mn} \text{ for } (m \text{ and } n = 1,2,3,\dots,6) \quad (6)$$

$$\pi_{mn} = 2\pi_{ijkl} \text{ for } (m \text{ and/or } n = 4,5,6) \quad (7)$$

where  $\pi_{11} = \pi_{1111}$ ,  $\pi_{44} = \pi_{2323}$ ,  $\pi_{16} = 2\pi_{1112}$ ,  $\pi_{12} = \pi_{1122}$ ,  $\pi_{66} = \pi_{1212}$ . In general,  $\pi_{ij} \neq \pi_{ji}$  except for polycrystalline materials (Curie group  $\infty\infty m$ ) which show isotropy, and  $m3m$ ,  $432$ ,  $\bar{4}3m$  cubic groups. For these specific cubic groups there are three independent coefficients, namely  $\pi_{11}$ ,  $\pi_{12}$ , and  $\pi_{44}$ , but for the isotropic polycrystalline materials there are only two independent coefficients because  $\pi_{44} = \pi_{11} - \pi_{12}$ . This can be represented by a matrix relation between the resistivity change and applied stress as:

$$\begin{pmatrix} \Delta \rho_1 \\ \Delta \rho_2 \\ \Delta \rho_3 \\ \Delta \rho_4 \\ \Delta \rho_5 \\ \Delta \rho_6 \end{pmatrix} = \begin{pmatrix} \pi_{11} & \pi_{12} & \pi_{12} & 0 & 0 & 0 \\ \pi_{12} & \pi_{11} & \pi_{12} & 0 & 0 & 0 \\ \pi_{12} & \pi_{12} & \pi_{11} & 0 & 0 & 0 \\ 0 & 0 & 0 & \pi_{44} & 0 & 0 \\ 0 & 0 & 0 & 0 & \pi_{44} & 0 \\ 0 & 0 & 0 & 0 & 0 & \pi_{44} \end{pmatrix} \begin{pmatrix} X_1 \\ X_2 \\ X_3 \\ X_4 \\ X_5 \\ X_6 \end{pmatrix}$$

There are three important experimental configurations in which the measurement of piezoresistivity can be done, depending on the direction of applied stress, voltage and current. These three configurations are described below:

- (1) Uniaxial stress, current and voltage all measured in the common direction, with piezoresistivity coefficient given as :  $\pi_{11} = \Pi_{11} - (s_{11} - 2s_{12})$

- (2) Uniaxial stress measured perpendicular to the direction of current and voltage:  $\pi_{12} = \Pi_{12} + s_{11}$
- (3) Application of hydrostatic pressure ‘p’, with  $\sigma_1 = \sigma_2 = \sigma_3 = -p$ ,  $\sigma_4 = \sigma_5 = \sigma_6 = 0$ , and the hydrostatic piezoresistivity coefficient given as:  $\pi_h = \Pi_h - (s_{11} + 2s_{12})$

where  $s_{ij}$  is the elastic compliance of the material under test, and  $\Pi = \Delta R/R_0$  corresponds to the measured change in resistance. It should be noted that the measured piezoresistance coefficient needs to be corrected for elastic effects. The hydrostatic coefficient is related to the longitudinal and transverse piezoresistance coefficient as:

$$\pi_h = -(\pi_{11} + 2\pi_{12})$$

#### 2.1.4 Piezoresistivity in various materials

The piezoresistance phenomenon has been reported in a wide variety of materials, some of which are reviewed in this section.

**Semiconductors.** Piezoresistive behavior in Si and Ge semiconductors was initially reported by C. Smith at Bells Labs <sup>[14]</sup>. Smiths experiment is schematically shown in Fig. 2.1, where an uniaxial stress is applied to single crystal rods of silicon and germanium and the pressure coefficient of resistance is measured in two possible configurations, i.e. with current and stress parallel and perpendicular to each other. An applied stress is likely to change the atom spacing resulting in a shift in the energy levels. The results indicated that the coefficient  $\pi_{11}/\rho_0$  which was equal to  $-102.2 \times 10^{-11} \text{ Pa}^{-1}$  was larger in n-Si while the coefficient  $\pi_{44}/\rho_0$  was found to be larger in p-Si, n-Ge, and p-Ge being equal to  $+138.3 \times 10^{-11} \text{ Pa}^{-1}$ ;  $-138.1 \times 10^{-11} \text{ Pa}^{-1}$ ; and  $+96.7 \times 10^{-11} \text{ Pa}^{-1}$  respectively.



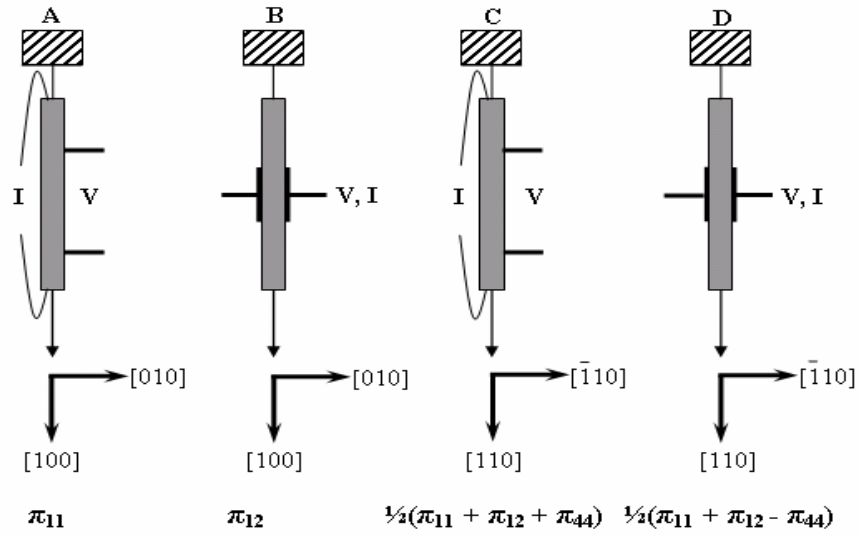


Figure 2.1 Piezoresistivity in semiconductor Si single crystals [14].

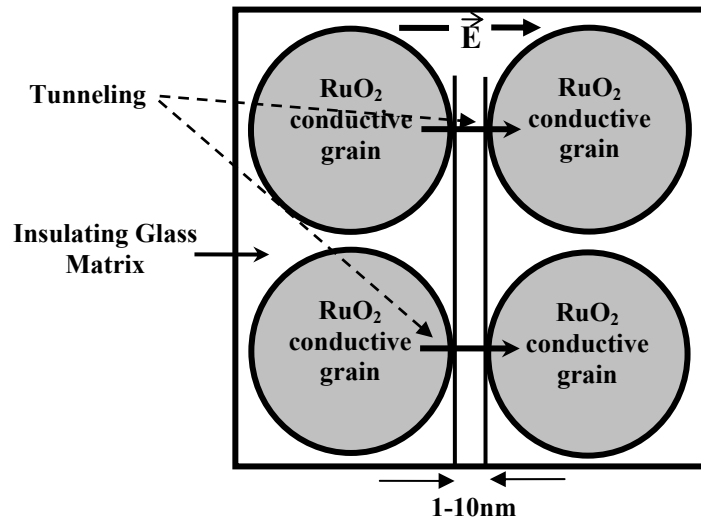


Figure 2.2 Conduction mechanism in RuO<sub>2</sub> based metal-insulator-metal junctions [16].

**Semiconducting ferroelectric ceramics.** Semiconducting barium strontium titanate (Ba,Sr)TiO<sub>3</sub> is known to exhibit a positive temperature coefficient of resistance (PTCR). Undoped BaTiO<sub>3</sub> shows ferroelectric behavior below the Curie temperature with a spontaneous polarization that can be reoriented by applying electric field. But in a semiconducting BaTiO<sub>3</sub> a large increase in resistivity over a small temperature range, above T<sub>c</sub> is observed. The piezoresistive response of this material is quite large as compared to other materials. The piezoresistive coefficients  $\pi_{12}$  and  $\pi_{11}$  for a La-doped (Ba,Sr)TiO<sub>3</sub> has been found to be of the order of  $2500 \times 10^{-12} \text{ Pa}^{-1}$ , whereas the hydrostatic piezoresistance coefficient  $\pi_h$  is around  $7500 \times 10^{-12} \text{ Pa}^{-1}$  at room temperature <sup>[15]</sup>.

**Ruthenium oxide based metal-insulator-metal structures.** Piezoresistivity in RuO<sub>2</sub>-based MIM or metal-insulator-metal structures was first reported by Canali et al <sup>[16]</sup>. The piezoresistive effect in these materials is based on the tunneling effect across the thin insulating grain boundaries. In a typical RuO<sub>2</sub> MIM structure, as shown in Fig. 2.2, the neighboring RuO<sub>2</sub> conducting grains are separated by thin insulating layer of glass, typically 1-10 nm in thickness. The effect of high hydrostatic pressure is to decrease this insulating layer thickness and enhance the tunneling of charge carriers. The resistivity and the barrier height are related by the following equation:

$$\rho = \rho_0 \exp(A\phi^{1/2}x) \text{ and } x \propto 1/\sigma_h$$

where  $\rho$  is resistivity,  $\phi$  the barrier height,  $x$  is insulator thickness and  $\sigma_h$  is hydrostatic pressure.

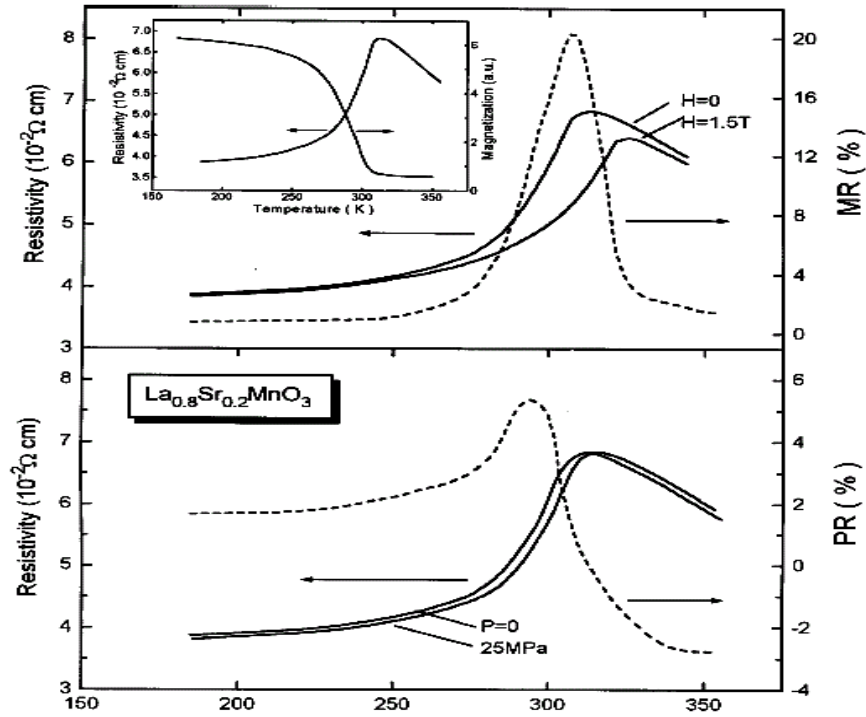


Figure 2.3 Piezoresistance and magnetoresistance in  $\text{La}_{0.8}\text{Sr}_{0.2}\text{MnO}_3$  as a function of temperature<sup>[20]</sup>.

Table 1 Piezoresistive coefficients of various materials.

Material	Resistivity ( $\Omega\text{cm}$ )	Piezoresistance coeff. $\pi_{12}$ ( $10^{-12} \text{ Pa}^{-1}$ )
n-type Si	11.7	530
P-type Si	7.8	-11
Semiconducting (Ba,Sr)TiO <sub>3</sub>	100	2500
$\text{La}_{0.8}\text{Sr}_{0.2}\text{MnO}_3\text{-ZrO}_2$	50	-120
Pure $\text{La}_{0.8}\text{Sr}_{0.2}\text{MnO}_3$	0.032	~ 221
Nb-doped $\text{La}_{0.8}\text{Sr}_{0.2}\text{MnO}_3$	36.78	~ 1500

**Diamond Films:** Thin diamond films have been found to exhibit piezoresistivity that makes them very attractive candidates for use as pressure transducers and accelerometers. These materials exhibit extremely large elastic modulus (>350 GPa), excellent thermal conductivity, high chemical resistance and piezoresistivity even at higher temperatures which makes them very attractive for sensors. Diamond MEMS or D-MEMS based pressure sensors are currently under investigation <sup>[17]</sup>.

**Ferromagnetic oxides:** Ferromagnetic perovskite ceramics based on the general formula,  $\text{La}_{1-x}\text{R}_x\text{MnO}_3$  (R= Ba, Sr, Ca, Pb) have attracted great interest owing to their colossal magnetoresistance (CMR). Figure 2.3 shows a composition close to the insulator metal phase boundary in the system  $\text{La}_{1-x}\text{Sr}_x\text{MnO}_3$  (x=0.20) which exhibits large magnetoresistance (MR) and piezoresistance (PR) effect. The figure also indicates that this composition has maximum PR near room temperature. Piezoresistive  $\text{La}_{0.8}\text{Sr}_{0.2}\text{MnO}_3 - \text{ZrO}_2$  based ceramic composites have been studied by Makino et al. <sup>[21]</sup>, for application in a diaphragm-less miniature force transducer. The composite containing 30 mass%  $\text{La}_{0.8}\text{Sr}_{0.2}\text{MnO}_3$  was found to exhibit excellent properties with high strength with the measured magnitude of piezoresistive coefficients as  $\pi_{12} = 120 \times 10^{-12} \text{ Pa}^{-1}$  and  $\pi_h = -470 \times 10^{-12} \text{ Pa}^{-1}$ .

## 2.2 Lanthanum strontium manganite

### *2.2.1 Introduction*

Lanthanum strontium manganite belongs to a class of materials which are termed as “CMR” or “colossal magnetoresistance” materials as they exhibit large change in resistance on application of magnetic field. Represented by general formula  $\text{R}_1$ .

$_{x}A_{x}MnO_{3}$ , where, ‘R’ is a trivalent rare-earth metal, such as La, Nd, or Pm; and ‘A’, is a divalent cation such as Sr, Ba, Ca, Pb; and x is concentration in mole percent. These series of compounds show an insulator to metal transition and the CMR effect, as mentioned earlier. For ‘R’ = La, the most reactive rare-earth element, and ‘A’ = Sr, it gives rise to a series of compounds  $La_{1-x}Sr_{x}MnO_{3}$ , which exhibit an insulator to metal transition at a critical composition of  $x = 0.175$  [22]. These compounds have been widely studied for use in magnetic memory and magnetic storage devices. Owing to their metallic behavior, catalytic properties and stability at high temperatures,  $La_{1-x}Sr_{x}MnO_{3}$  ceramics have been effectively used in solid oxide fuel cells, as a cathode material.

### 2.2.2 Crystal structure

$La_{1-x}Sr_{x}MnO_{3}$  has a typical perovskite unit cell structure. The La ions occupy the unit cell corners and the Mn ions form octahedra with oxygen ions as shown in Fig. 2.4. The La sites are designated as the ‘A’ sites, and the Mn sites are designated as the ‘B’ sites. The Sr ions substitute on the La sites and due to the difference in valence it causes distortion in the Mn-O bonds, which is responsible for the electronic conduction. The addition of divalent  $Sr^{2+}$  also causes the  $Mn^{3+}$  ions to exist as  $Mn^{4+}$  ions. The effect of Sr amount on the a-axis parameter of  $La_{1-x}Sr_{x}MnO_{3}$  lattice is as shown in Fig. 2.5.

### 2.2.3 Phase diagram

The binary phase diagram of the  $LaMnO_{3} - SrMnO_{3}$  system is as shown in Fig. 2.6.  $LaMnO_{3}$  and  $SrMnO_{3}$  form a complete solid solution for all concentrations, except

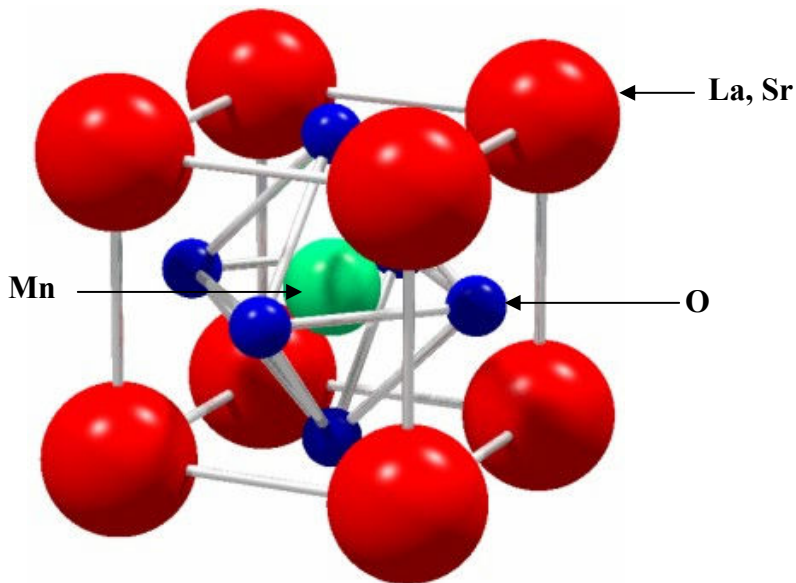


Figure 2.4 Perovskite unit cell of  $\text{La}_{1-x}\text{Sr}_x\text{MnO}_3$  [23].

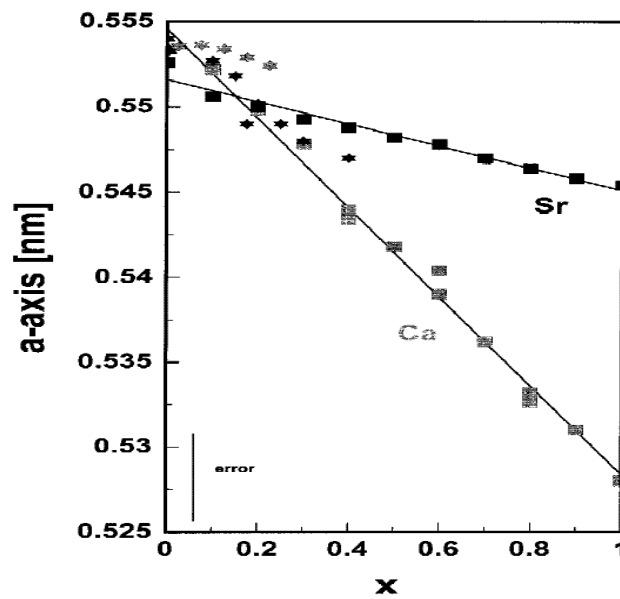


Figure 2.5 Effect of strontium amount on the a-axis parameter in  $\text{La}_{1-x}\text{Sr}_x\text{MnO}_3$  [24].

for the miscibility gap that exists at an intermediate ratio of La:Sr,<sup>[24]</sup>. At low concentrations of Sr, there is a structural transition from rhombohedral to orthorhombic, depending on the temperature. It should be noted that the crystal structure of  $\text{La}_{1-x}\text{Sr}_x\text{MnO}_3$  is dependent on the  $\text{Mn}^{3+}/\text{Mn}^{4+}$  ratio. The composition  $\text{La}_{0.8}\text{Sr}_{0.2}\text{MnO}_3$  has an orthorhombic unit cell at 1400°C and higher temperatures. The compositional phase diagram of the ternary  $\text{ZrO}_2 - \text{CeO}_2 - \text{LaO}_{1.5}$  system has been shown in Fig. 2.7<sup>[25]</sup>.

#### 2.2.4 Magnetic properties – Colossal magnetoresistance

The magnetoresistance ratio is defined as the percentage change in resistance with external magnetic field and is expressed as  $\Delta R/R(0) = (R(0) - R(H))/R(0)$ . The  $\text{La}_{1-x}\text{Sr}_x\text{MnO}_3$  series of compounds are considered to be a large bandwidth subset of the manganese oxides<sup>[13]</sup>. The hopping amplitude of the electrons in the  $e_g$  – band is larger than in other manganites, due to the sizes of ions involved in the composition. The magnetic Curie temperature in these compounds is a function of the hole doping<sup>[26]</sup>. This is shown in Fig. 2.8 which illustrates the temperature dependence of resistivity. The marked arrow on this figure represents the Curie temperature,  $T_c$ .

Figure 2.9 shows that the material goes through an insulator to metal transition, which is also confirmed by the magnetic or electronic phase diagram of  $\text{La}_{1-x}\text{Sr}_x\text{MnO}_3$ , as shown in Fig. 2.10<sup>[14]</sup>. The phase diagram predicts the state of the material at different dopant amount. The various regions that exist in the magnetic or electronic phase diagram, FM and PM stand for ferromagnetic and paramagnetic metal respectively, FI and PI stand for ferromagnetic and paramagnetic insulators and CI is the spin-canted insulator state. The  $T_N$  is the Neel temperature. As predicted by the

phase diagram, above a critical concentration of Sr,  $x = 0.17$  the material is a ferromagnetic metal.

### 2.2.5 *Electrical properties – piezoresistance*

The uniaxial pressure dependence of piezoresistance and magnetic field dependence of magnetoresistance is shown in Fig. 2.11. Similar effects have been found by Tokura et al <sup>[22]</sup> for the temperature dependence of resistivity as a function of pressure and external field variation as shown in Fig. 2.12. The resistivity as a function of temperature increases gradually with decreasing temperature and then drops sharply at the ferromagnetic Curie temperature marked with triangles in Fig. 2.12. The effect of magnetic field was similar but more temperature dependent. This indicates that the external pressure can shift the Curie temperature in these materials. Figure 2.13 depicts this result for different concentrations of Sr. It can be seen that the Curie temperature increased with pressure and the change was much higher at lower concentrations of Sr. A demonstration of the piezoresistive phenomena in  $\text{La}_{1-x}\text{Sr}_x\text{MnO}_3$  from the practical viewpoint has been given by Makino et al. <sup>[21]</sup>. They developed a composite with 30 mass%  $\text{La}_{0.8}\text{Sr}_{0.2}\text{MnO}_3$  dispersed in 12 mol% ceria-partially stabilized Zirconia. The change in resistivity with uniaxial pressure is shown in Fig. 2.14 and was found to be linear. As compared to pure  $\text{La}_{0.8}\text{Sr}_{0.2}\text{MnO}_3$  the composite exhibited high compressive strength and was found to be suitable in high force sensing applications.

SUMMARY:  $\text{La}_{1-x}\text{Sr}_x\text{MnO}_3$  has been widely studied for use in solid oxide fuel cells (SOFC) as a cathode material, owing to its inherently porous nature and metallic behavior



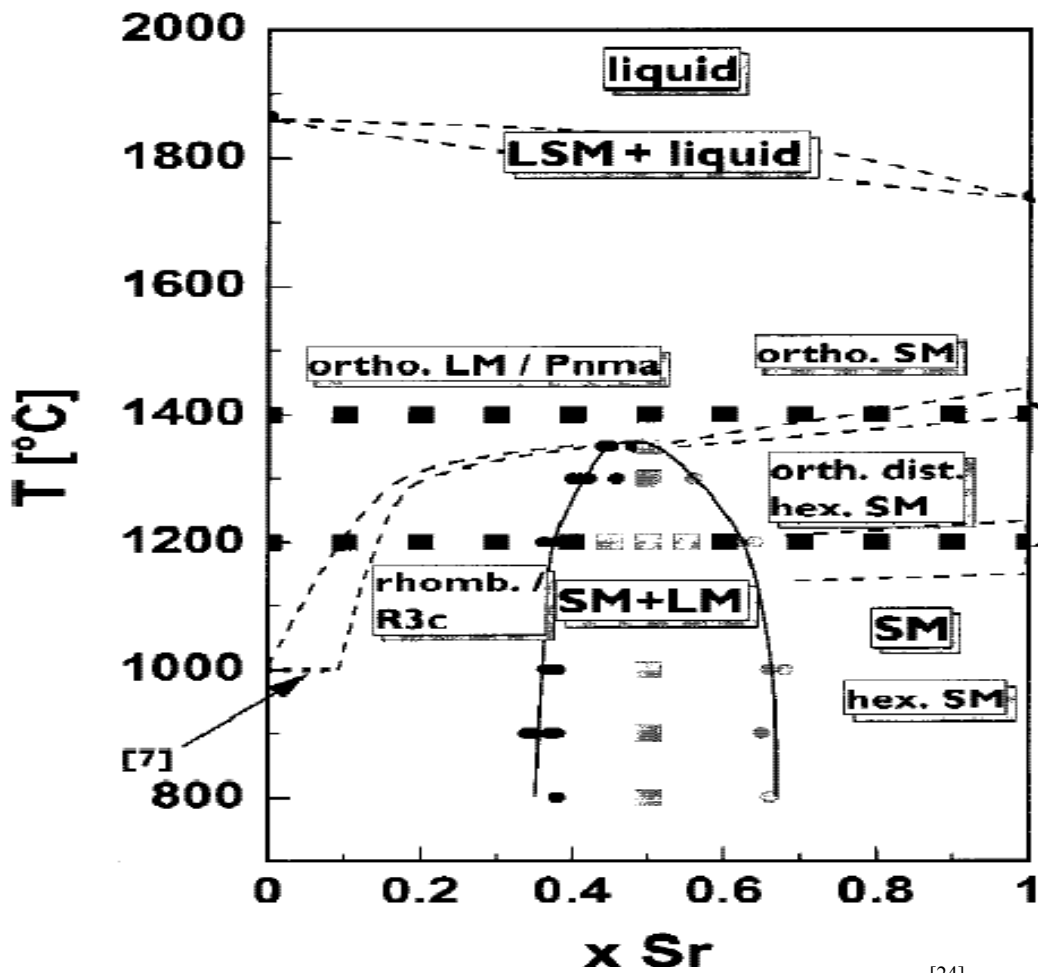


Figure 2.6 Binary phase diagram of the  $\text{LaMnO}_3$  -  $\text{SrMnO}_3$  system <sup>[24]</sup>.

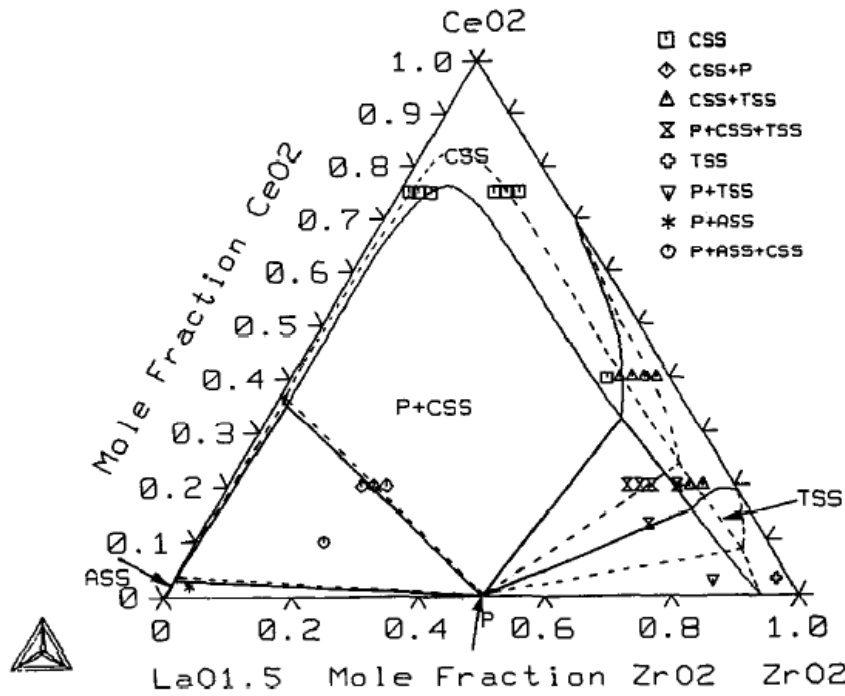


Figure 2.7 Ternary phase diagram of the  $ZrO_2 - CeO_2 - LaO_{1.5}$  system [25].

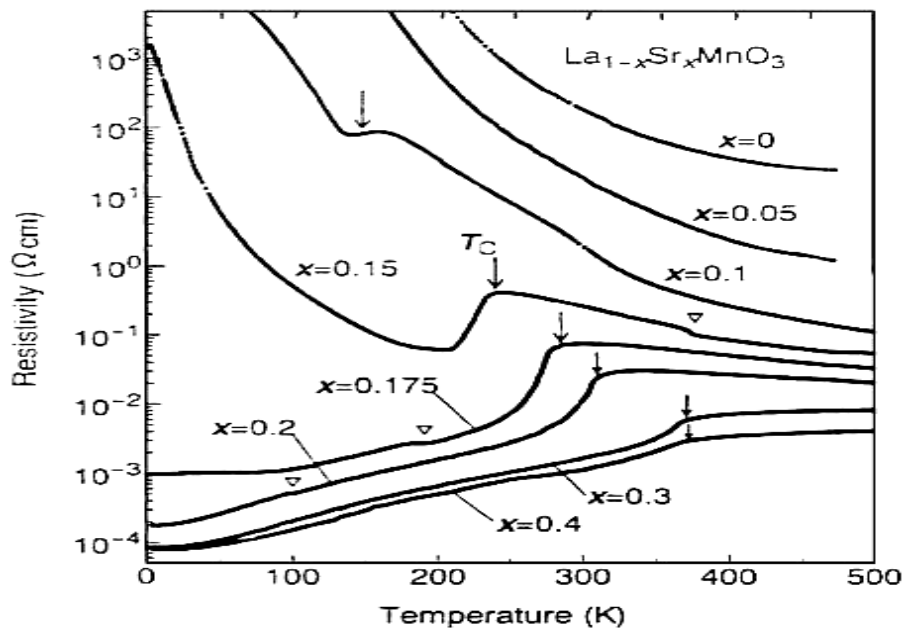


Figure 2.8 Temperature dependence of resistivity in  $La_{1-x}Sr_xMnO_3$  with varying Sr amounts [26].

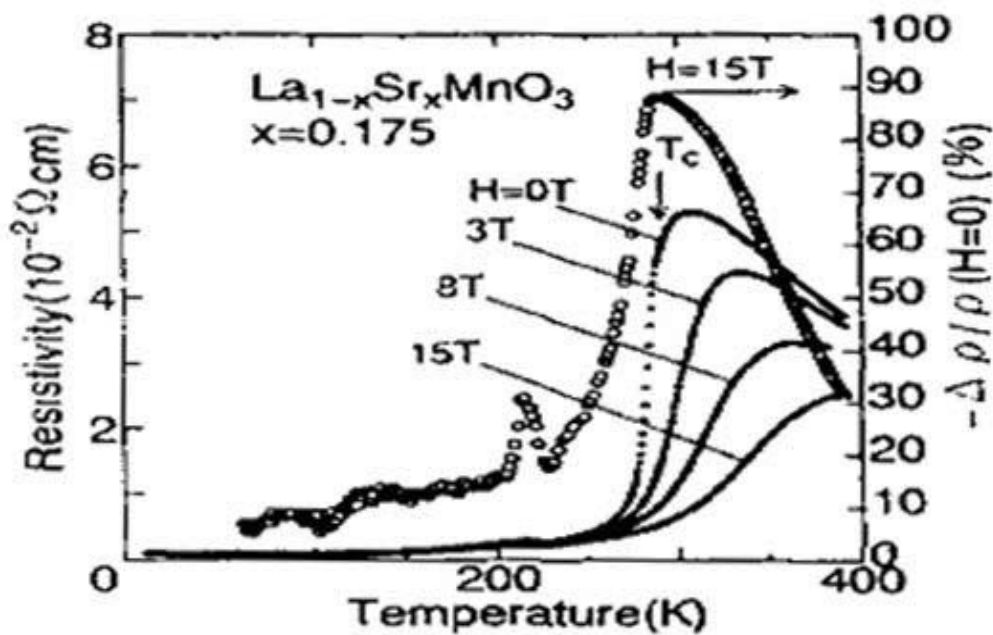


Figure 2.9 Temperature dependence of resistivity in  $\text{La}_{1-x}\text{Sr}_x\text{MnO}_3$  under varying magnetic field <sup>[14]</sup>.

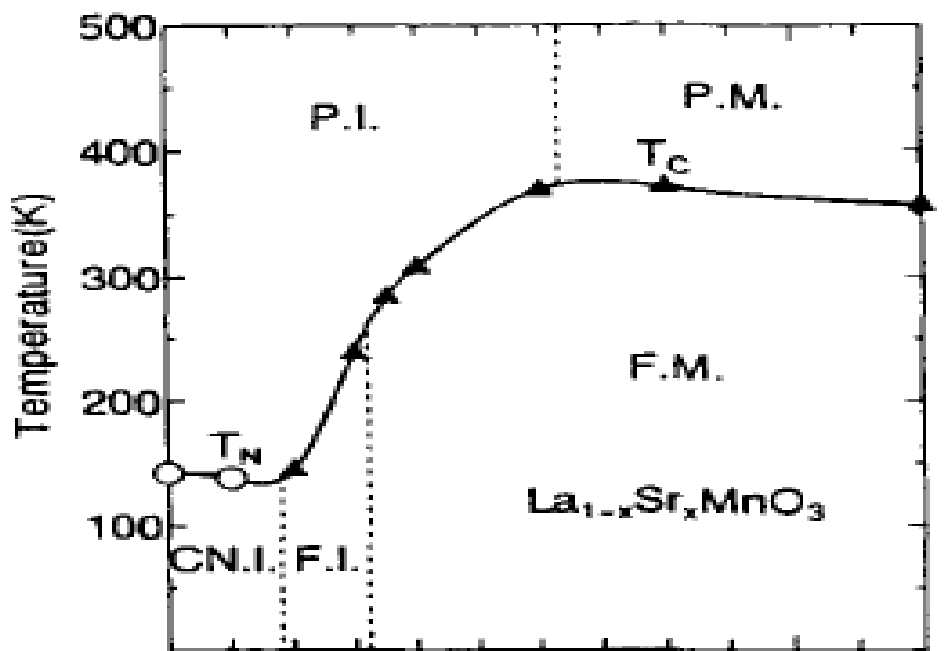


Figure 2.10 Magnetic phase diagram of  $\text{La}_{1-x}\text{Sr}_x\text{MnO}_3$  <sup>[14]</sup>.

at room temperature. This material has also been studied for magnetoresistive properties and the effect of a number of parameters like composition variation, temperature, doping elements, hydrostatic and uniaxial pressure on the CMR behavior have been investigated. However, the piezoresistive behavior of this material has not been explored in detail. Especially, the effect of doping elements and synthesis condition on the magnitude of the piezoresistive coefficient needs to be investigated. The opportunity is enormous as the development of a giant piezoresistive coefficient material will open up new design of force and pressure sensors. Since this material has been found to have an excellent ‘crystal lattice match’ with partially and completely stabilized  $ZrO_2$  [28], the composites of these two systems further provide the opportunity to develop a tough and smart material for applications in harsh environments such as automotive and aerospace.

Motivated from these facts this research focuses on the synthesis of the giant piezoresistive material. The effects of A-site and B-site doping ions on the piezoresistive behavior of  $La_{0.8}Sr_{0.2}MnO_3$  have been investigated and results are analyzed in terms of microstructure and magnetic/electric properties. Further, the composites of  $La_{0.8}Sr_{0.2}MnO_3$  and partially stabilized  $ZrO_2$  were synthesized and investigated to develop a mechanically tough and smart material for a potential application in the automotive field as a force sensing structural member. An attempt was also made to modify the surface characteristic of this material to incorporate the oxygen gas sensing capability such that the same material can act as a structural unit, force sensor, and oxygen gas sensor.

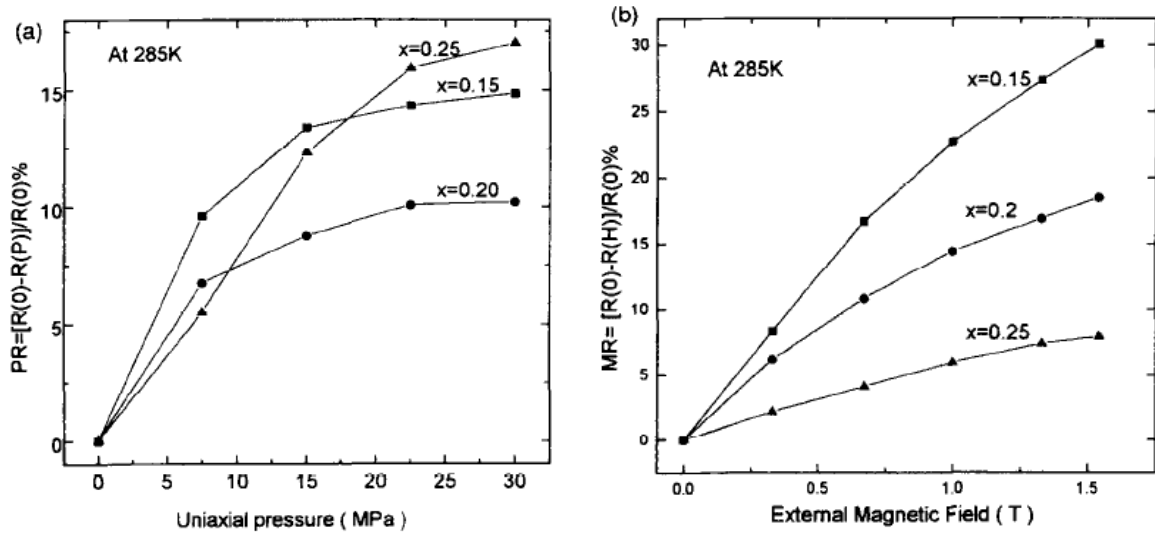


Figure 2.11 (a) Uniaxial pressure dependence of piezoresistance and (b) magnetic field dependence of magnetoresistance in  $\text{La}_{1-x}\text{Sr}_x\text{MnO}_3$  [29].

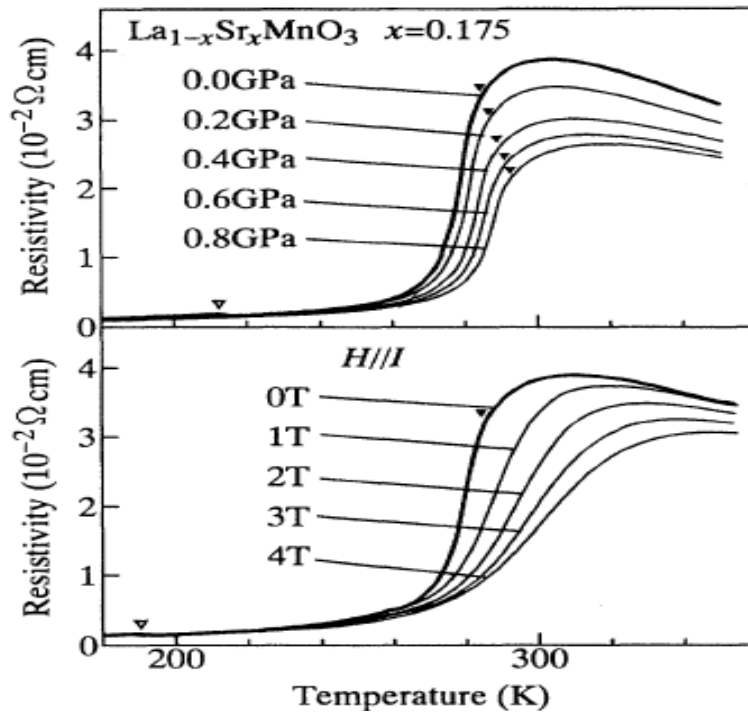


Figure 2.12 Temperature dependence of resistivity in  $\text{La}_{1-x}\text{Sr}_x\text{MnO}_3$  with external magnetic field and pressure [22].

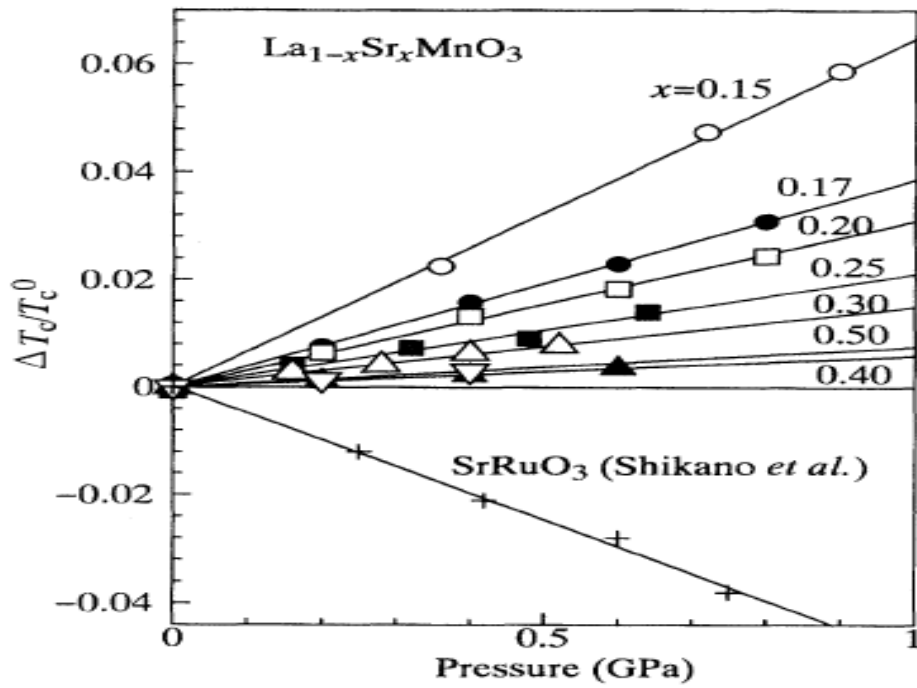


Figure 2.13 Effect of pressure on the Curie temperature of  $\text{La}_{1-x}\text{Sr}_x\text{MnO}_3$  [22].

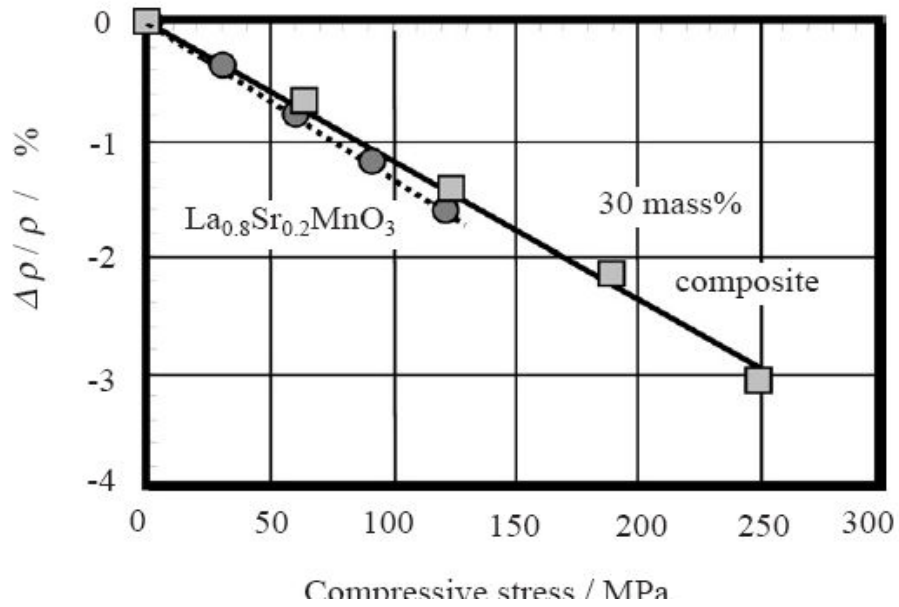


Figure 2.14 Change in electrical resistivity of  $\text{La}_{0.8}\text{Sr}_{0.2}\text{MnO}_3$  with uniaxial stress [21].

CHAPTER 3  
MATERIALS SYNTHESIS AND CHARACTERIZATION

3.1 Material characterization techniques

Various material characterization techniques have been utilized in this research for quantitative and qualitative analysis of the material structure and properties. For the crystal structure determination and phase identification, a Siemens Kryptoflex 810 D500 X-ray Diffractometer, was utilized. The microstructure analysis was conducted using a Zeiss Leo Smart SEM, combined with energy dispersive x-ray spectroscopy (EDAX) for elemental analysis. This equipment is available through the NANOFAB facility at UT Arlington campus. A transmission electron microscopy (TEM) analysis of the surface and bulk grain structure was performed using JEOL 220CX TEM. The resistivity measurements were done using an Agilent 34401A 6½ digit digital multimeter and Keithley 6517A Electrometer, (see Appendix F for details). For piezoresistivity measurements, an Instron® microtester was used, as shown in Fig. 3.2(b).

Magnetic property studies were conducted using a Quantum Design® Superconducting Quantum Interference Device or SQUID. The SQUID is an extremely sensitive and highly precision instrument used for measuring magnetic properties of materials. The device may be configured as a magnetometer to detect extremely small magnetic fields, as small as  $10^{-13}$  T, existing in the human brain.

The great sensitivity of the SQUID is associated with measuring changes in magnetic field associated with one quantum flux. The SQUID magnetometer has been extensively utilized in the present work for determination of magnetic properties of the samples, including magnetization of the samples with applied magnetic field and temperature in the zero field cooled condition, Curie temperature, magnetization loops at room temperature.

### 3.2 Experimental procedure

#### *3.2.1 Ceramic powder processing*

All the ceramic samples in the present work were synthesized via the conventional ceramic powder processing technology. Solid state ceramic processing is a convenient and widely used method to synthesize ceramic materials. In the present work,  $\text{La}_{0.8}\text{Sr}_{0.2}\text{MnO}_3$  powders, both in the pure and A-site and B-site modified state were synthesized using the steps outlined below:

##### *3.2.1.1 Stoichiometric calculations*

Reagent grade  $\text{La}_2\text{O}_3$ ,  $\text{SrCO}_3$ ,  $\text{MnO}_2$ ,  $\text{Li}_2\text{CO}_3$ ,  $\text{Bi}_2\text{O}_3$ ,  $\text{CuO}$ ,  $\text{Nb}_2\text{O}_5$ , and  $\text{CeO}_2$  powders were obtained from Alfa Aesar Co. Massachusetts, USA. The  $\text{ZrO}_2$  powder was obtained from Tosoh Corporation, Japan, under trade name TZ-0. The base composition  $\text{La}_{0.8}\text{Sr}_{0.2}\text{MnO}_3$  (LSMO) was modified at the A-site or La-site by lithium and bismuth. Three different doping concentrations of 2 mol%, 4 mol%, and 6 mol% were selected for both Li and Bi. For the B-site or manganese site copper (Cu) and niobium (Nb) were selected as the modifying elements. Compositions with concentration of 2 mol% Cu atoms and 2 mol% and 5 mol% Nb were synthesized. The



stoichiometric calculations were done to calculate the amount of starting powders required for ball milling. Table 1 shows the chemical formulae for all the compositions investigated in this study. The above mentioned formulations are based on the hypothesis that substitution of dopant ions in the crystal lattice is critically dependent on the size factor and electro-negativity. A general description of the possible lattice site occupancy of various ions are shown in Table 2.

#### *3.2.1.2 Powder mixing*

The powders were mixed in a polyethylene bottle with ZrO<sub>2</sub> grinding balls of 3mm diameter. The ZrO<sub>2</sub> grinding media was obtained from Tosoh Corporation, Japan. Ethanol was used as the solvent for ball milling. Ball milling was done two times (before and after calcination) for each composition for 24 – 36 hrs. For the case of ball milling after calcinations, 10 mm diameter ZrO<sub>2</sub> grinding balls were used to ensure complete breakdown of hard agglomerates and the ball milling period was increased to 36 hrs. After each step of ball milling the ceramic powders slurries were dried in an oven in borosilicate glass vessels at 80°C.

#### *3.2.1.3 Calcination*

After initial mixing of oxide and carbonate powders as per the composition, the dried powders were palletized using a 1 inch diameter stainless steel die and pressed using a mechanical hand press. The pellets were then calcined in alumina crucible starting from 800°C to 1100°C for 2 to 4 hrs. X-ray diffraction (XRD) analysis was conducted after each calcination step to determine the formation of the perovskite phase. It was found that a complete perovskite crystal structure was formed above

1000°C. The optimized calcination temperature and time was found to be 1025°C and 4 hrs. Calcined powders were crushed and ball milled for 36hrs using 10mm diameter grinding media in ethanol.

#### *3.2.1.4 Sintering*

The powders after calcination were ball milled, dried and sieved in a 270 mesh size. The sieved powders ensured uniform starting particle size for better sintering and grain size characteristics. The sieved powders were pressed into uniform bars of size 40 x 12.7 x 1.5 mm<sup>3</sup> in a hardened steel die at 15 MPa pressure. These bars were then isostatically pressed at 207 MPa in a cold isostatic press (CIP) to obtain a green body. The green bodies were sintered in an alumina crucible at a series of temperatures ranging from 1200°C to 1450°C for 2 to 6 hrs. The sintering temperature was optimized between 1350°C and 1400°C for 6 hrs for most samples. The density of the samples was measured using Archimedes principle in de-ionized water. X-ray diffraction (XRD) analysis was conducted for each sintered sample to detect the presence of any second phase and determination of the parent lattice crystal structure.

#### *3.2.2 Sample preparation*

The bars obtained after sintering were sized to appropriate dimensions using a dicing saw. For the SEM specimen a small piece was cut, mirror polished and thermally etched for 1 hr in a Lindberg Blue<sup>®</sup> high temperature furnace. For the magnetic property measurement using SQUID, the sample dimensions were cut to the size of 6.0 x 6.0 x 1.0 mm<sup>3</sup>. The samples for piezoresistivity measurements were prepared by cutting a square piece of dimension 5.0 x 5.0 x 1.5 mm<sup>3</sup> and painting a high temperature silver

electrode Dupont<sup>®</sup> 6160 on the two opposite edges. The painted electrodes were then fired at 850°C for 1 hr to obtain a good electrical contact. Two thin wires were then soldered on the opposite smaller faces for the piezoresistivity measurement. The samples for TEM investigation were a small thin slice mounted on a copper grit, dimple grinded and ion milled for appropriate times to get a thin area suitable for observation.

### *3.2.3 Piezoresistivity measurement technique*

Piezoresistivity measurements were done on the samples by compressing them between two highly polished, flat surfaces using a modified Instron<sup>®</sup> Microtester as shown in Fig. 3.2(b). Figure 3.2(a) shows the sample holder and sample arrangement. A compressive load of up to 480 N maximum was applied uniaxially at the rate of 240N/min, onto the sample. The load was monitored by the Instron<sup>®</sup> software provided by the manufacturer. The resistance change in the samples was recorded by an Agilent<sup>®</sup> 6½ digit multimeter. For each measurement, specific load intervals of 60 N were chosen, and the load was held constant at that value for 3 min allowing the resistance values to be stabilized. After the 3 min holding time the compressive load was resumed at the same rate. The samples were shielded using the electronics packing foil and insulated using alumina stripes for accurate measurements.

Table 2 A-site and B-site modified compositions of LSMO.

A-site modified compositions		B-site modified compositions
$\text{La}_{0.78}\text{Li}_{0.02}\text{Sr}_{0.2}\text{MnO}_3$	$\text{La}_{0.78}\text{Bi}_{0.02}\text{Sr}_{0.2}\text{MnO}_3$	$\text{La}_{0.8}\text{Sr}_{0.2}\text{Cu}_{0.02}\text{Mn}_{0.98}\text{O}_3$
$\text{La}_{0.76}\text{Li}_{0.04}\text{Sr}_{0.2}\text{MnO}_3$	$\text{La}_{0.76}\text{Bi}_{0.04}\text{Sr}_{0.2}\text{MnO}_3$	$\text{La}_{0.8}\text{Sr}_{0.2}\text{Nb}_{0.02}\text{Mn}_{0.98}\text{O}_3$
$\text{La}_{0.74}\text{Li}_{0.06}\text{Sr}_{0.2}\text{MnO}_3$	$\text{La}_{0.74}\text{Bi}_{0.06}\text{Sr}_{0.2}\text{MnO}_3$	$\text{La}_{0.8}\text{Sr}_{0.2}\text{Nb}_{0.05}\text{Mn}_{0.95}\text{O}_3$

Table 3 Ionic radii of various elements and their preferred lattice sites.

Ion	Ionic Radii (pm)	La-site	Mn-site
$\text{La}^{3+}$	117.2	✓	
$\text{Sr}^{2+}$	132.0	✓	
$\text{Li}^{+}$	90.0	✓	
$\text{Bi}^{3+}$	117.0	✓	
$\text{Mn}^{3+}$	72.0		✓
$\text{Cu}^{2+}$	87.0		✓
$\text{Nb}^{5+}$	78.0		✓

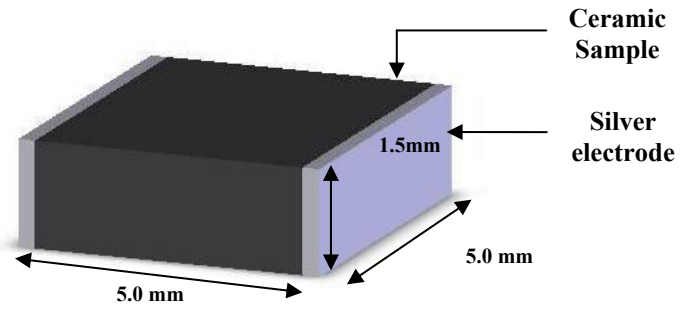


Figure 3.1 Schematic diagram of the samples prepared for piezoresistive measurement.

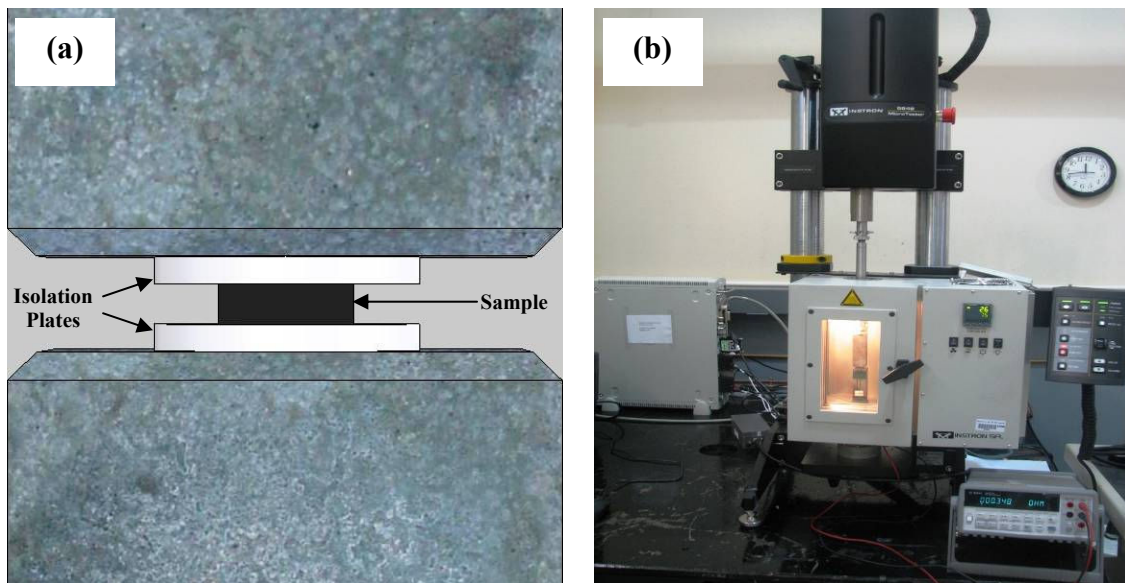


Figure 3.2 (a) Sample holder design and sample under test and (b) test set-up using Instron® microtester, for piezoresistivity measurements.

## CHAPTER 4

### PIEZORESISTIVITY IN PURE AND MODIFIED $\text{La}_{0.8}\text{Sr}_{0.2}\text{MnO}_3$ BULK POLYCRYSTALLINE CERAMICS

#### 4.1 Pure Lanthanum Strontium Manganite

##### *4.1.1 Crystal structure and phase determination*

As mentioned in the experimental section, pure  $\text{La}_{0.8}\text{Sr}_{0.2}\text{MnO}_3$  (LSMO) composition was synthesized from the powders of  $\text{La}_2\text{O}_3$ ,  $\text{SrCO}_3$ , and  $\text{MnO}_2$  [30-33]. An optimum calcination temperature was determined by carrying a series of experiments in conjunction with XRD analysis. In each experiment, the mixed powders were palletized and calcined starting from 800°C for 4 hrs to 1025°C for 4 hrs. XRD results after each calcination step are shown in Fig. 4.1. This figure clearly indicates that at 800°C, a significant fraction of second phases are present and a complete perovskite structure was not formed. After increasing the temperature to 1025°C, the fraction of second phases reduced substantially and a relatively pure perovskite LSMO was formed [34].

Figure 4.2 shows the x-ray diffraction (XRD) patterns for sintered samples of LSMO and illustrates the process for optimization of sintering temperature. At low sintering temperature of 1300°C and a holding time of 4 hrs, a relatively high fraction of LSMO was formed with a minor amount of secondary phase, but the microstructure was found to contain substantial porosity as shown in Fig. 4.3. After increasing the sintering

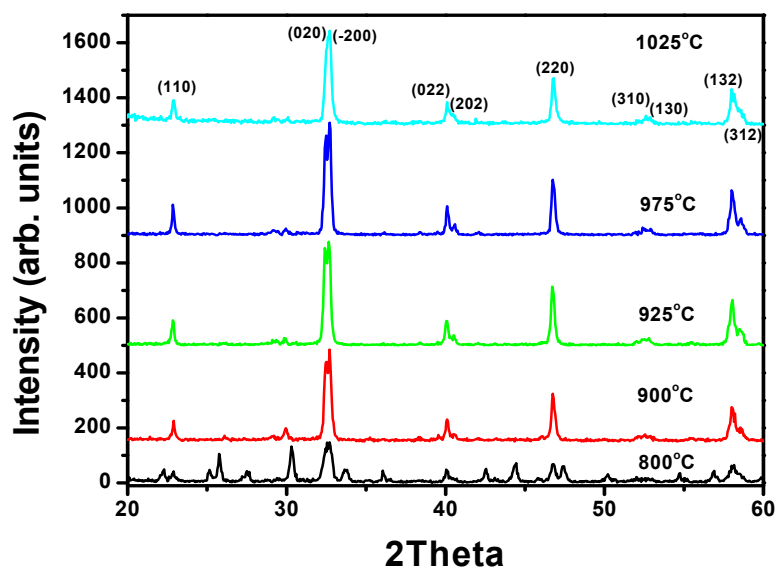


Figure 4.1 X-ray diffraction patterns of pure  $\text{La}_{0.8}\text{Sr}_{0.2}\text{MnO}_3$  calcined at different temperatures.

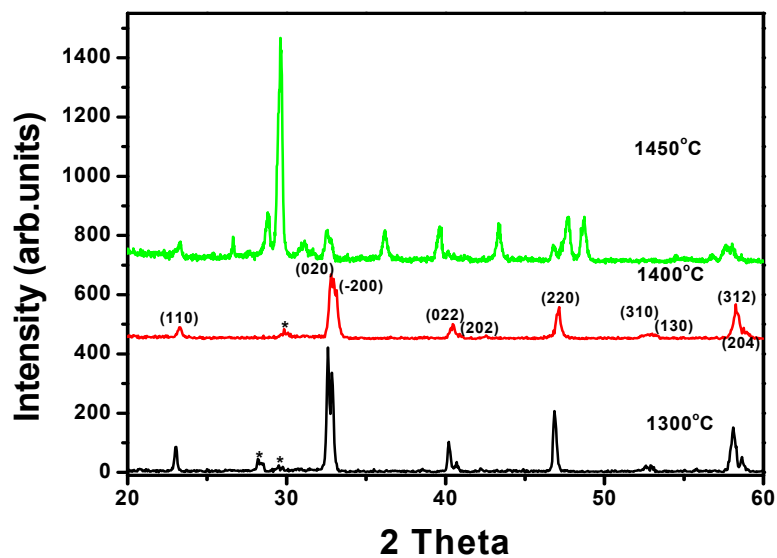


Figure 4.2 X-ray diffraction patterns of pure  $\text{La}_{0.8}\text{Sr}_{0.2}\text{MnO}_3$  sintered at different temperatures.

temperature and time to 1400°C and 6hrs respectively, an optimal microstructure was obtained with minute amount of secondary phase. A relatively dense microstructure can be seen in Fig. 4.5(a). On increasing the sintering temperature to 1450°C, a large fraction of secondary phases reappeared and the major phase did not correspond to perovskite structure. Hence the optimized sintering temperature and time was found to be 1400°C for 6 hrs.

#### *4.1.2 Microstructures*

The  $\text{La}_{1-x}\text{Sr}_x\text{MnO}_3$  series of mixed oxide compounds are inherently porous by nature owing to the multivalent state of Mn ions. A series of compounds with varying percentages of Sr, with 'x' = 0.15, 0.20, and 0.25, were synthesized and found to be porous. The micrographs shown in the Fig. 4.3 illustrate this point. As mentioned earlier, the composition containing 20 mol% Sr is known to exhibit maximum magnitude of the piezoresistivity in this system at room temperature. Thus, the base composition of  $\text{La}_{0.8}\text{Sr}_{0.2}\text{MnO}_3$  (LSMO) was selected and optimum sintering conditions in terms of temperature, time and CIP pressure were determined to obtain dense microstructure.

#### *4.1.3 Magnetic properties*

At room temperature, LSMO is expected to be a ferromagnetic oxide, as predicted from the magnetic phase diagram shown in Fig. 2.10. A zero field cooled (ZFC) temperature dependence of magnetic moment was measured in the temperature interval of 10-390 K under a magnetic field of 200 Oe. Figure 4.6(a) indicates that the ferromagnetic Curie temperature of pure LSMO is around 300 K. Room temperature



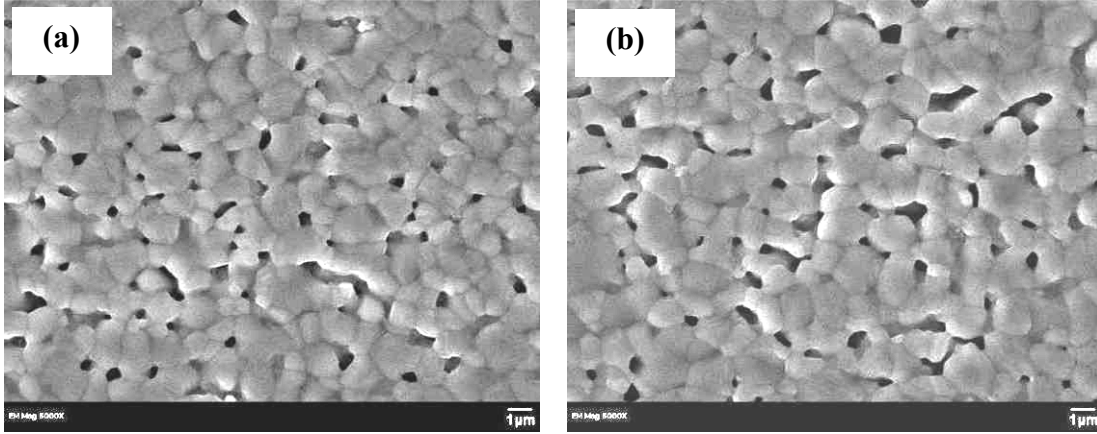


Figure 4.3 SEM micrographs of pure  $\text{La}_{0.8}\text{Sr}_{0.2}\text{MnO}_3$  sintered at different temperatures (a) 1300°C, 4 hrs, (b) 1400°C, 4 hrs.

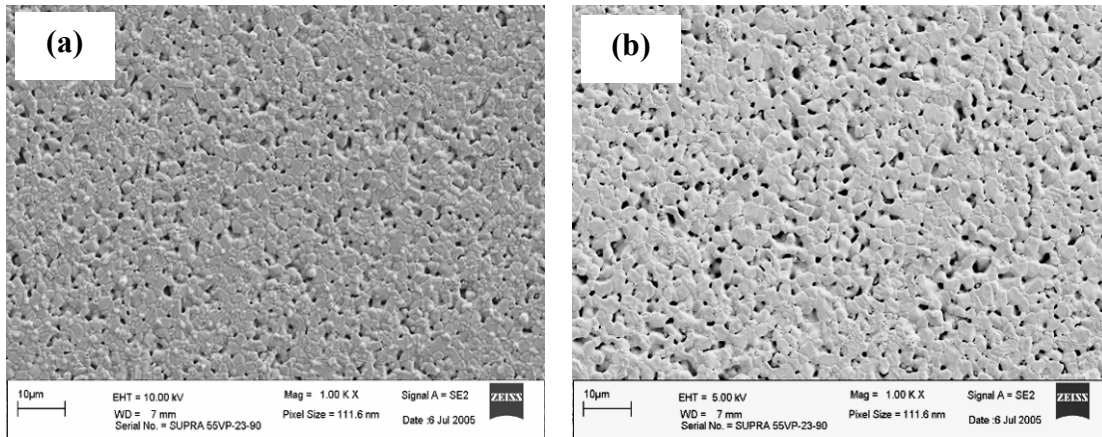


Figure 4.4 SEM micrographs of (a)  $\text{La}_{0.75}\text{Sr}_{0.25}\text{MnO}_3$ , and (b)  $\text{La}_{0.85}\text{Sr}_{0.15}\text{MnO}_3$  sintered at 1400°C for 6 hrs.

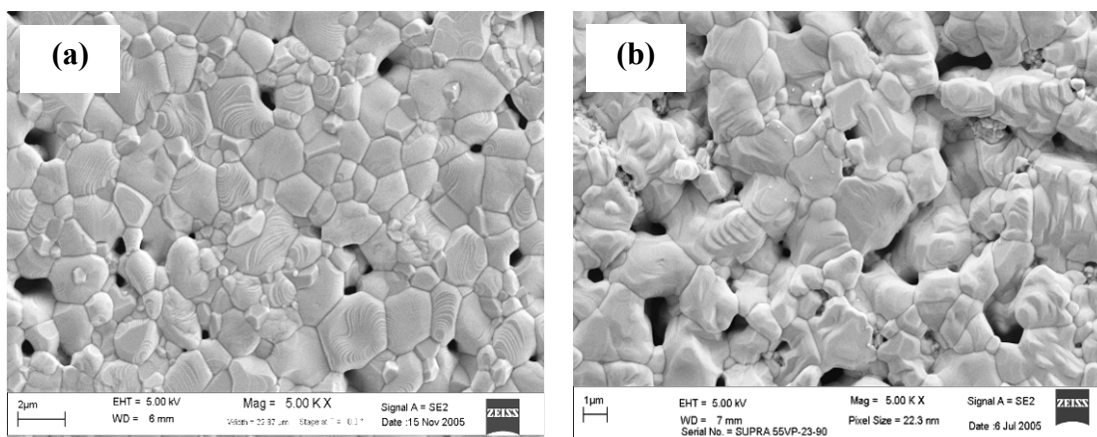


Figure 4.5 SEM micrographs of pure  $\text{La}_{0.8}\text{Sr}_{0.2}\text{MnO}_3$  sintered at (a)  $1400^\circ\text{C}$ , 6 hrs, (b)  $1450^\circ\text{C}$ , 6 hrs.

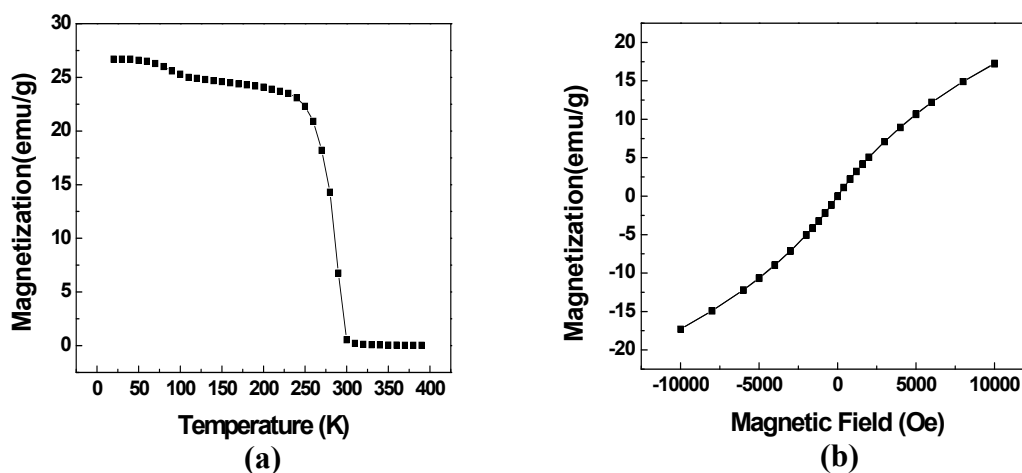


Figure 4.6 (a) Temperature dependence of magnetization, and (b) room temperature magnetic hysteresis loop for pure  $\text{La}_{0.8}\text{Sr}_{0.2}\text{MnO}_3$ .

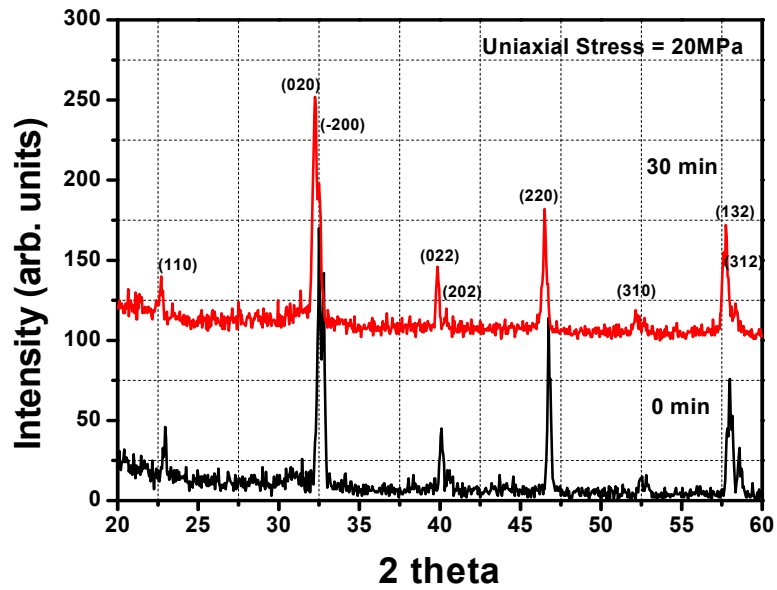


Figure 4.7 Effect of pressing time on the XRD peaks of  $\text{La}_{0.8}\text{Sr}_{0.2}\text{MnO}_3$ .

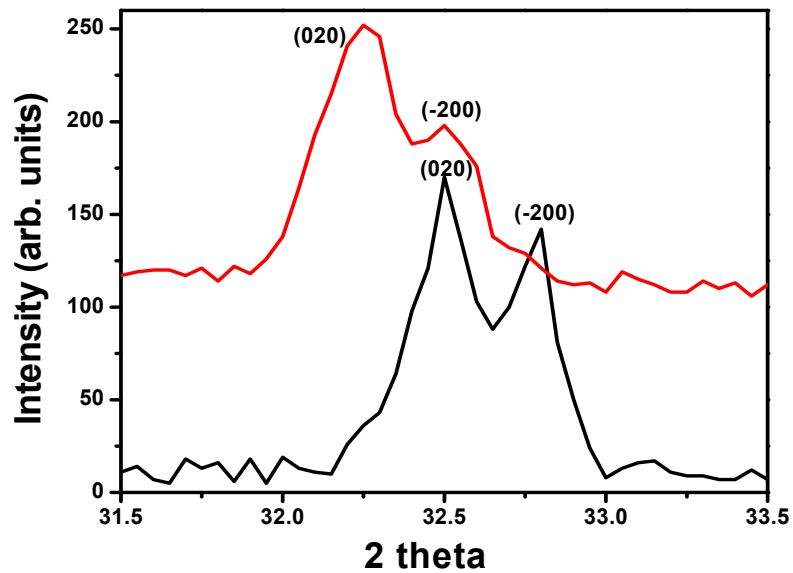


Figure 4.8 Peak shifts of (020) and (-200) reflections of  $\text{La}_{0.8}\text{Sr}_{0.2}\text{MnO}_3$  with pressing time.

magnetic hysteresis for pure LSMO composition is shown in Fig. 4.6(b) and it was found that the saturation magnetic field is more than 1 Tesla.

#### *4.1.4 Piezoresistivity*

The piezoresistive behavior of pure LSMO at uniaxial stress ranging from 0 - 20 MPa is shown in Fig. 4.7. The resistivity of pure LSMO was found to be  $3.15 \times 10^{-2} \Omega\text{cm}$ . The resistivity was found to decrease with applied external uniaxial stress and a total change of  $\sim 0.5\%$  was measured at 19.2 MPa. During the measurement, uniaxial stress was held constant for 3 min so as to obtain a stable change in the resistance value. The change in resistivity for small variation in uniaxial pressure was found to be non-linear. This result indicates that significant improvements in the piezoresistance behavior are required to increase the response at low applied pressure.

### 4.2 Effect of A-site dopants

A-site doping of pure  $\text{La}_{0.8}\text{Sr}_{0.2}\text{MnO}_3$  (LSMO) was done by modifying with 2 mol%, 4 mol% and 6 mol% of Li and Bi ions. The effect of substituting Li and Bi in equi molar amounts on electrical and magnetic properties have been discussed in parallel in the following sections.

#### *4.2.1. Effect of Lithium*

##### *4.2.1.1 Crystal structure and phase determination*

Lithium doping corresponding to 2 mol%, 4 mol% and 6 mol% was done by mixing  $\text{Li}_2\text{CO}_3$  powder before calcination. Figure 4.8 shows the XRD patterns for Li-modified compositions after calcination. Perovskite crystal structure was obtained after calcining at  $1025^\circ\text{C}$  for 4 hrs. A small fraction of secondary phase was also found at

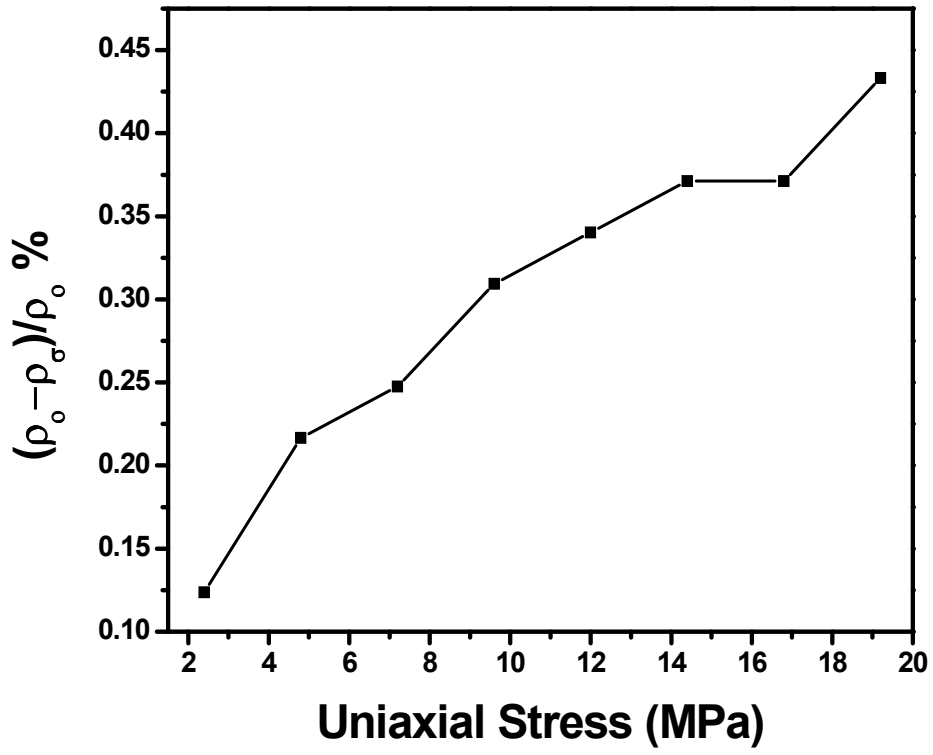


Figure 4.9 Piezoresistivity in pure  $\text{La}_{0.8}\text{Sr}_{0.2}\text{MnO}_3$ .

higher percentages of Li doping. Figure 4.9 shows the XRD patterns for the three selected percentages of Li doping after sintering at 1400°C for 6 hrs. A small fraction of secondary phase was present in the samples as is evident from the XRD patterns.

#### *4.2.1.2 Microstructures*

Figure 4.10 shows the microstructures of 2 mol% Li modified  $\text{La}_{0.8}\text{Sr}_{0.2}\text{MnO}_3$  or  $\text{La}_{0.78}\text{Li}_{0.02}\text{Sr}_{0.2}\text{MnO}_3$  sintered at 1400°C for 6 hrs. It is clear from the XRD pattern shown in Fig. 4.9 and the microstructure that this composition provides perovskite phase with high density, although small amount of porosity is present even after sintering at high temperatures with long holding times. Figures 4.11 and 4.12 show the microstructures of  $\text{La}_{0.76}\text{Li}_{0.04}\text{Sr}_{0.2}\text{MnO}_3$  and  $\text{La}_{0.74}\text{Li}_{0.06}\text{Sr}_{0.2}\text{MnO}_3$  sintered compositions respectively.

It was found that for the same sintering temperature and time as the amount of dopant was increased, a larger grain size was observed. It is to be noted here that the porosity could not be completely eliminated for all the Li-modified compositions and a small fraction of secondary phases were found to be present for 4 and 6 mol% Li-modified LSMO. In order to eliminate the secondary phases completely sintering in the gaseous atmosphere under pressure may be required.

#### *4.2.1.3 Magnetic properties*

The zero field cooled temperature dependence of magnetization at an external magnetic field of 200 Oe is as shown in the Fig. 4.13. It is evident from this figure that as the concentration of lithium was increased from 2 mol% to 6 mol%, the Curie

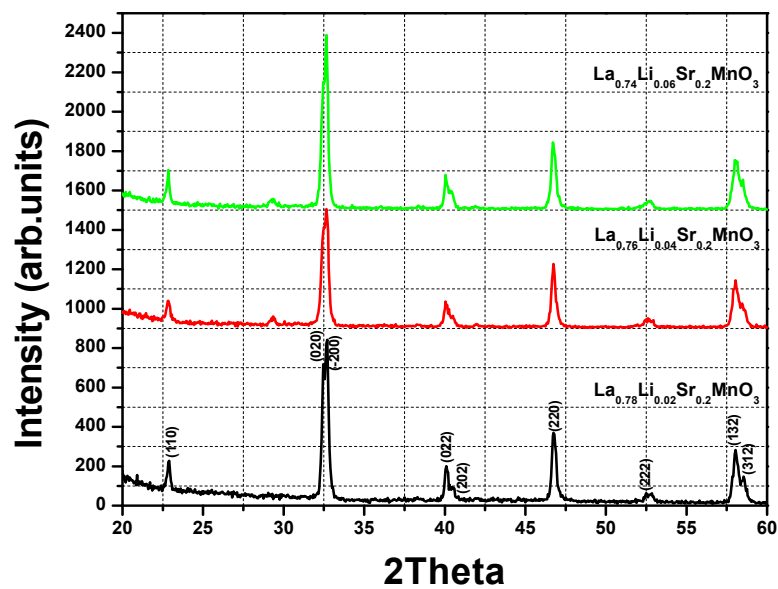


Figure 4.10 X-ray diffraction patterns of calcined powders of Li-modified  $\text{La}_{0.8}\text{Sr}_{0.2}\text{MnO}_3$  compositions.

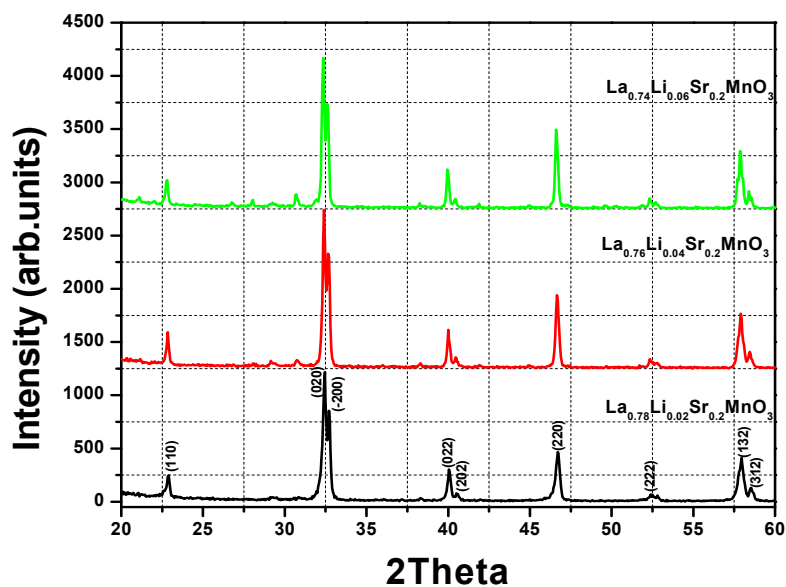


Figure 4.11 X-ray diffraction patterns for Li-modified  $\text{La}_{0.8}\text{Sr}_{0.2}\text{MnO}_3$  compositions sintered at  $1400^\circ\text{C}$  for 6 hrs.

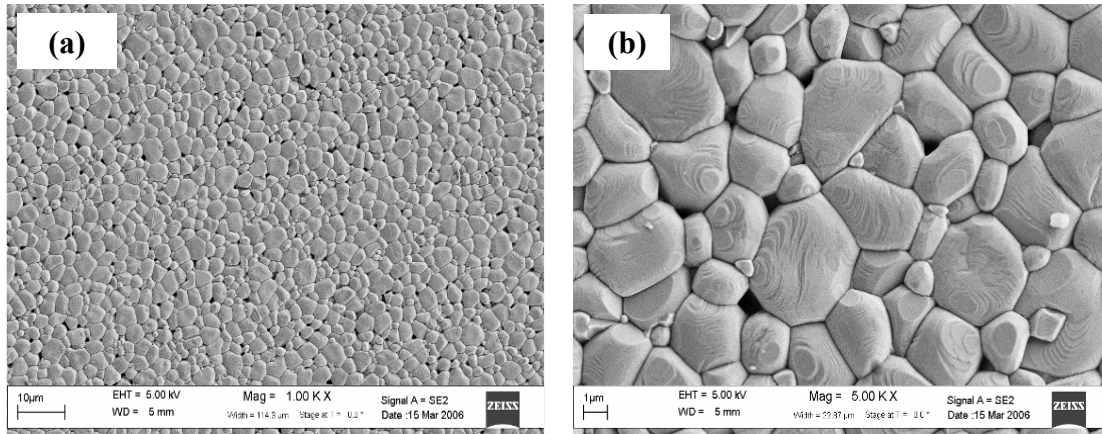


Figure 4.12 SEM micrographs of 2 mol% Li modified  $\text{La}_{0.8}\text{Sr}_{0.2}\text{MnO}_3$  sintered at  $1400^\circ\text{C}$  for 6 hrs, (a) at 1 kX, (b) at 5 kX.

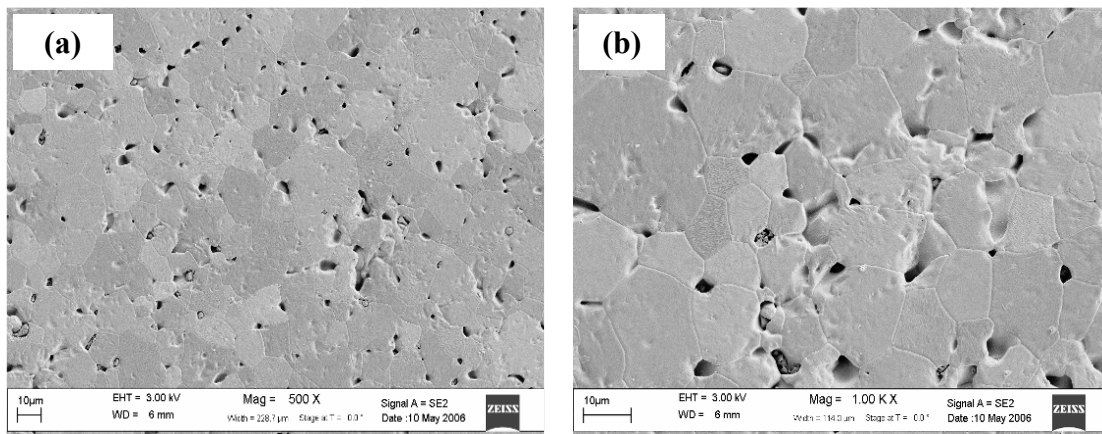


Figure 4.13 SEM micrographs of 4 mol% Li modified  $\text{La}_{0.8}\text{Sr}_{0.2}\text{MnO}_3$  sintered at  $1400^\circ\text{C}$  for 6 hrs, (a) at 1 kX, (b) at 5 kX.



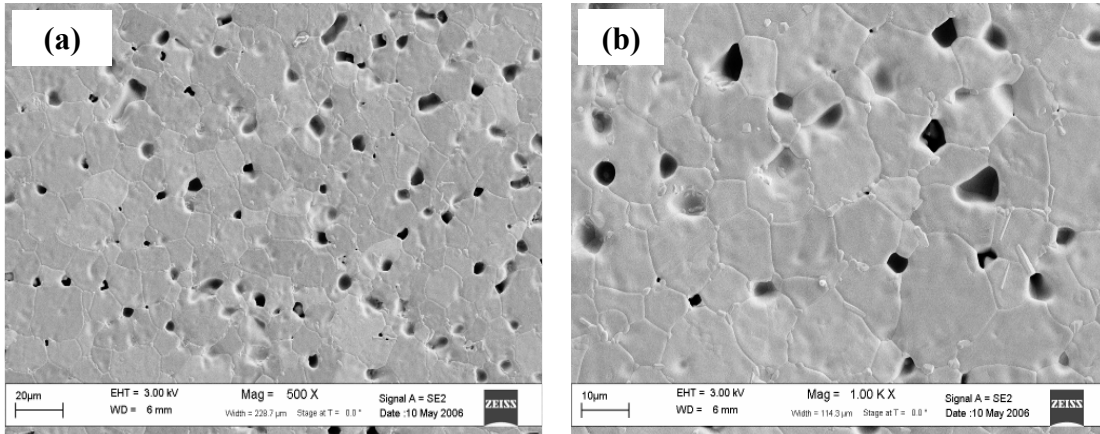


Figure 4.14 SEM micrographs of 6 mol% Li modified  $\text{La}_{0.8}\text{Sr}_{0.2}\text{MnO}_3$  sintered at  $1400^\circ\text{C}$  for 6 hrs, (a) at 1 kX, (b) at 5 kX.

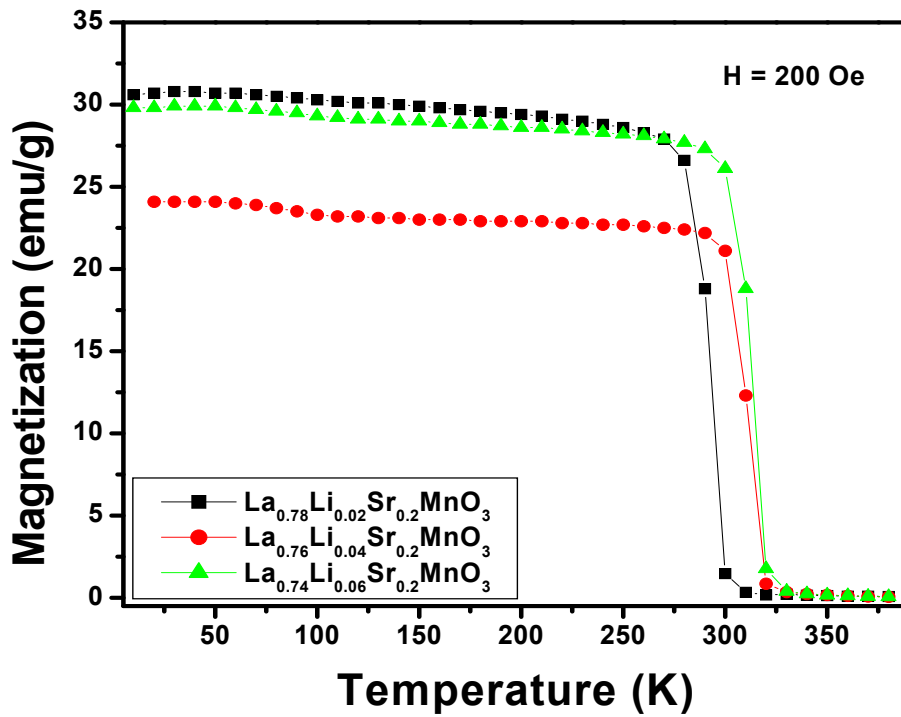


Figure 4.15 Temperature dependence of magnetization in lithium modified  $\text{La}_{0.8}\text{Sr}_{0.2}\text{MnO}_3$  with varying Li concentration.

temperature increased from 300 K for 2 mol% Li to around 325 K for 6 mol% Li. The Curie temperature for pure LSMO is around 300 K. The room temperature magnetic hysteresis loop, exhibiting the change in magnetization with external magnetic field is shown in Fig. 4.14 for the three modified compositions. It was observed that the hysteresis loop for the composition with 2 mol% Li could not be saturated even at external applied magnetic field of 1 T, while the higher concentrations of Li were easily saturated. A general trend of increasing magnetization with the dopant concentration was observed which is also probed by the fact that the Curie temperature increases with the dopant amount.

#### *4.2.1.4 Piezoresistivity*

The piezoresistivity in Li doped compositions is shown in Fig. 4.15. The change in resistivity with applied uniaxial stress was found to be non linear. A negative change in resistivity i.e. an increase in electrical resistivity with applied uniaxial stress was observed for all the compositions. A sudden rise in resistivity magnitude was obtained for applied uniaxial stress in the range of 0 – 2 MPa. As compared to the pure LSMO composition, the Li-modified samples had a nominal increasing effect on the piezoresistivity magnitude and relative percentage change of approximately 1% was observed for all the composition, which is two times of that for pure LSMO.

#### *4.2.2 Effect of bismuth*

##### *4.2.2.1 Crystal structure and phase determination*

Powder diffraction patterns of the calcined powders of Bi modified compositions is shown in Fig. 4.16. Orthorhombic unit cell was indexed based on the

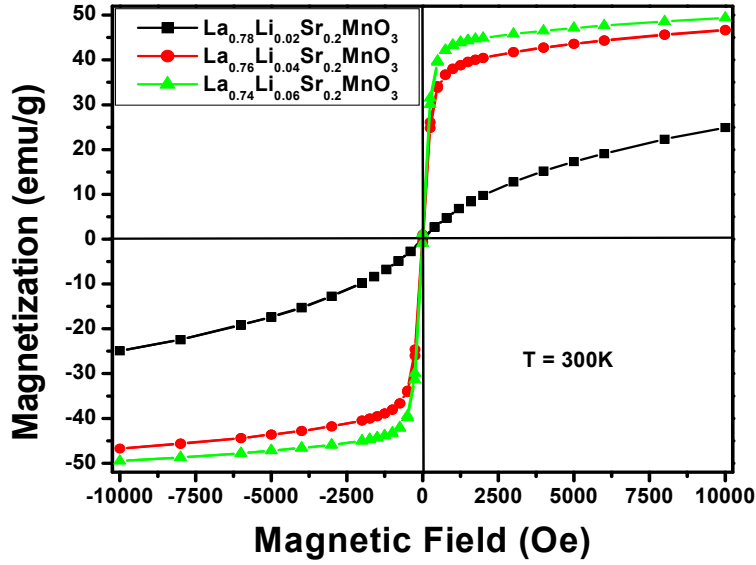


Figure 4.16 Room temperature magnetic hysteresis for lithium modified  $\text{La}_{0.8}\text{Sr}_{0.2}\text{MnO}_3$  with varying Li concentration.

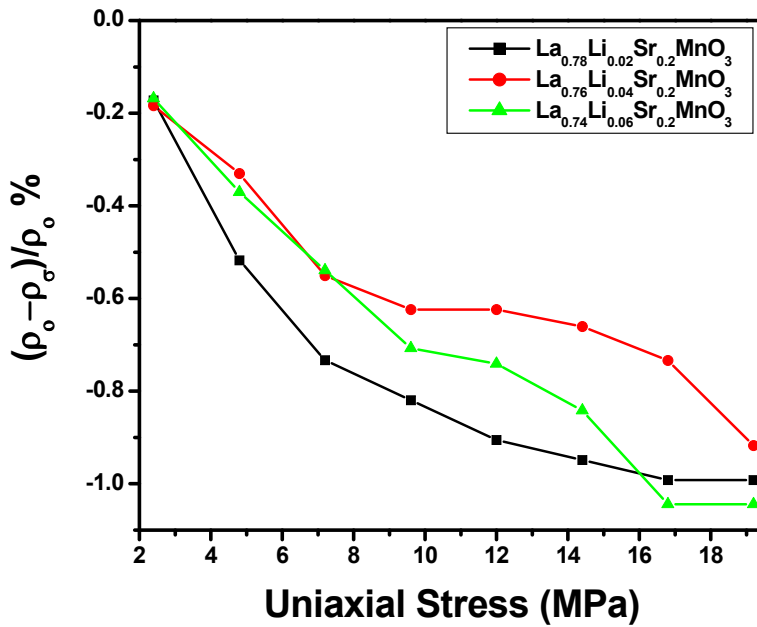


Figure 4.17 Piezoresistivity in lithium modified  $\text{La}_{0.8}\text{Sr}_{0.2}\text{MnO}_3$  compositions.

JCPDS powder diffraction file. A minor fraction of secondary phase was observed in the 2 mol% Bi and 6 mol% Bi doped LSMO powders after calcination. The fraction of the secondary phases increases after sintering in the temperature range of 1300°C to 1400°C for 6 hrs as shown in Fig. 4.17. The presence of secondary phases was related to bismuth rich compounds that precipitate at higher temperatures. Thus, the piezoresistive and magnetic properties are average of the perovskite and secondary phases.

#### *4.2.2.2 Microstructures*

The SEM micrographs for 2 mol% Bi-modified LSMO are shown in the Fig. 4.18. It was found that at 1400°C, a significant amount of liquid second phase was present. Figures 4.19 and 4.20 show that as the sintering temperature was reduced to 1350°C and 1300°C, the second phase was reduced to a large extent, but a nominal porosity was observed. It is evident from Fig. 4.21 that for the composition with 4 mol% Bi a significant amount of second phase was present and could not be eliminated by sintering in air. Bismuth composition of 6 mol% also showed the presence of large amount of bismuth rich second phase. Although the grain structure improved significantly as compared to that of 4 mol% modified sample a significant increase in the grain size also occurred. Some porosity was still present owing to the large grain size after sintering at 1400°C for 6 hrs as shown in Fig. 4.22.

#### *4.2.2.3 Magnetic properties*

The ZFC temperature dependence of magnetization for Bi-modified compositions is shown in Fig. 4.23. The Curie temperature of pure LSMO is

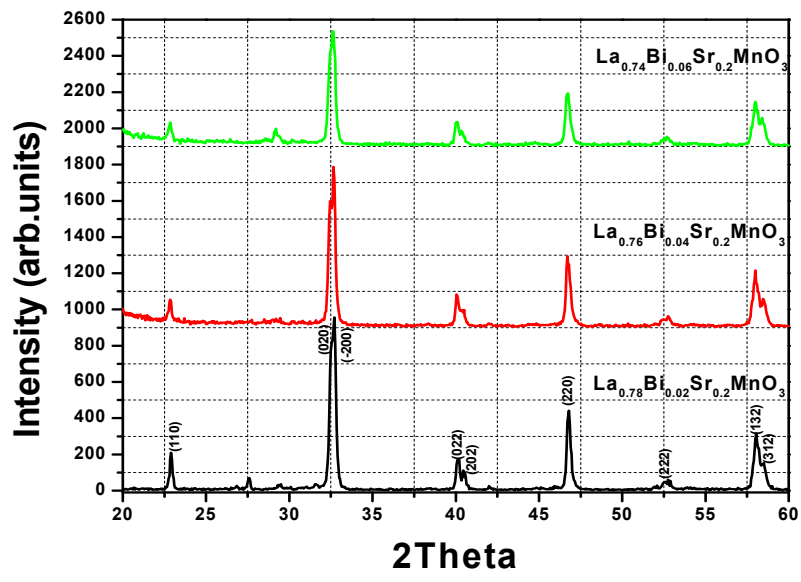


Figure 4.18 X-ray diffraction patterns of Bi-modified  $\text{La}_{0.8}\text{Sr}_{0.2}\text{MnO}_3$  compositions.

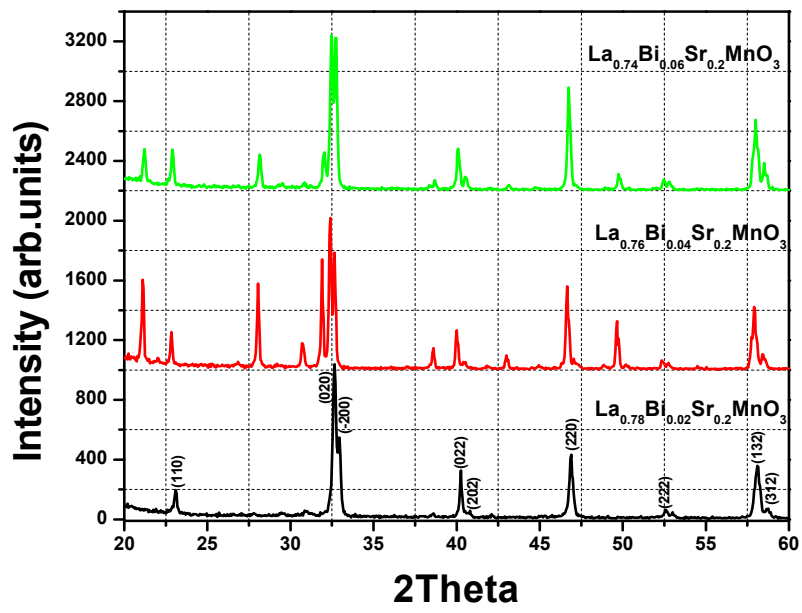


Figure 4.19 X-ray diffraction patterns of Bi-modified  $\text{La}_{0.8}\text{Sr}_{0.2}\text{MnO}_3$  sintered compositions.

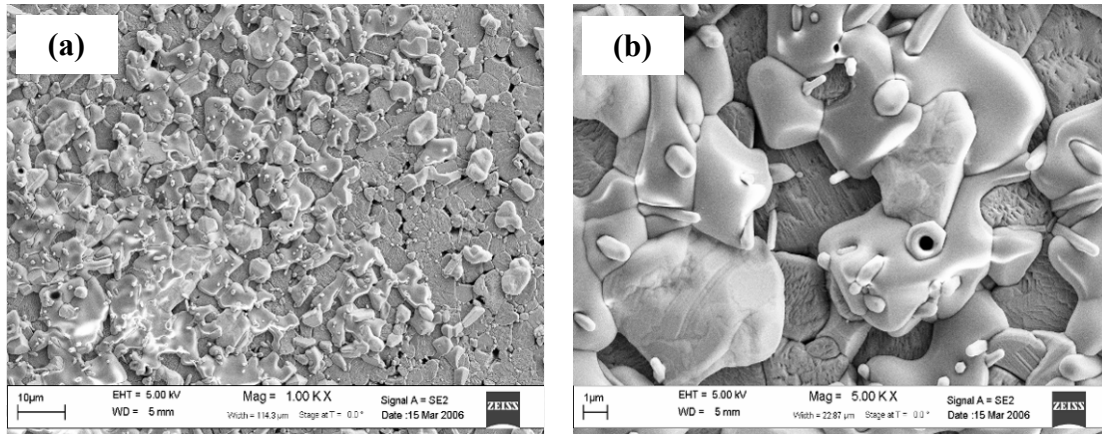


Figure 4.20 SEM micrographs of 2 mol% Bi modified  $\text{La}_{0.8}\text{Sr}_{0.2}\text{MnO}_3$  after sintering at  $1400^\circ\text{C}$  for 6 hrs, (a) at 1 kX, (b) at 5 kX.

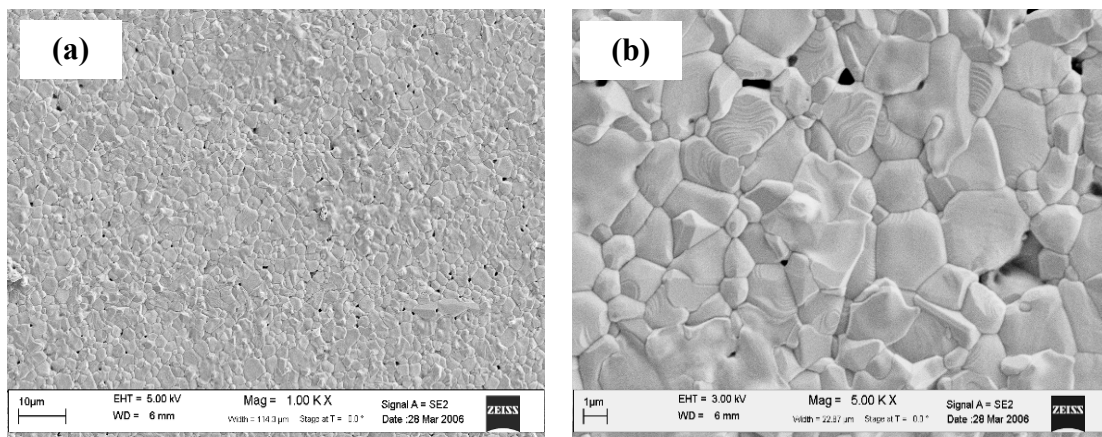


Figure 4.21 SEM micrographs of 2 mol% Bi modified  $\text{La}_{0.8}\text{Sr}_{0.2}\text{MnO}_3$  after sintering at  $1350^\circ\text{C}$  for 6 hrs, (a) at 1 kX, (b) at 5 kX.

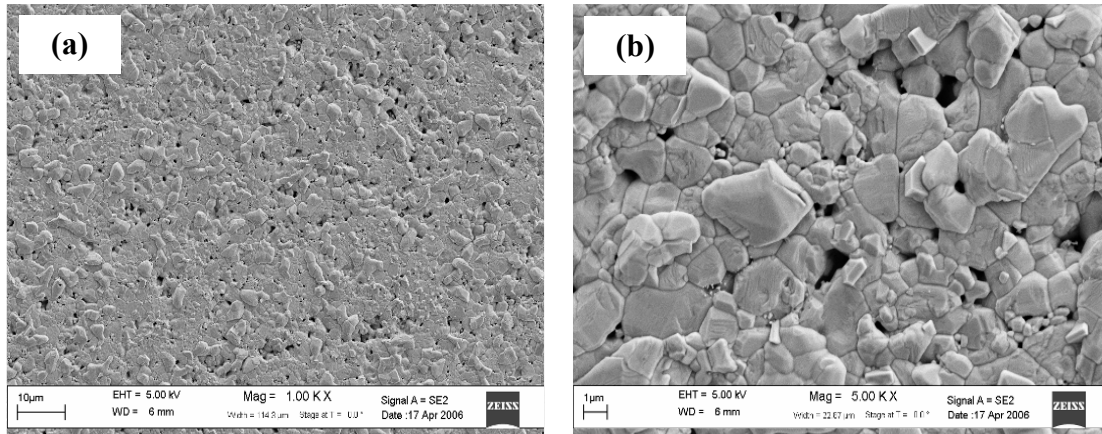


Figure 4.22 SEM micrographs of 2 mol% Bi modified  $\text{La}_{0.8}\text{Sr}_{0.2}\text{MnO}_3$  after sintering at  $1300^\circ\text{C}$  for 6 hrs, (a) at 1 kX, (b) at 5 kX.

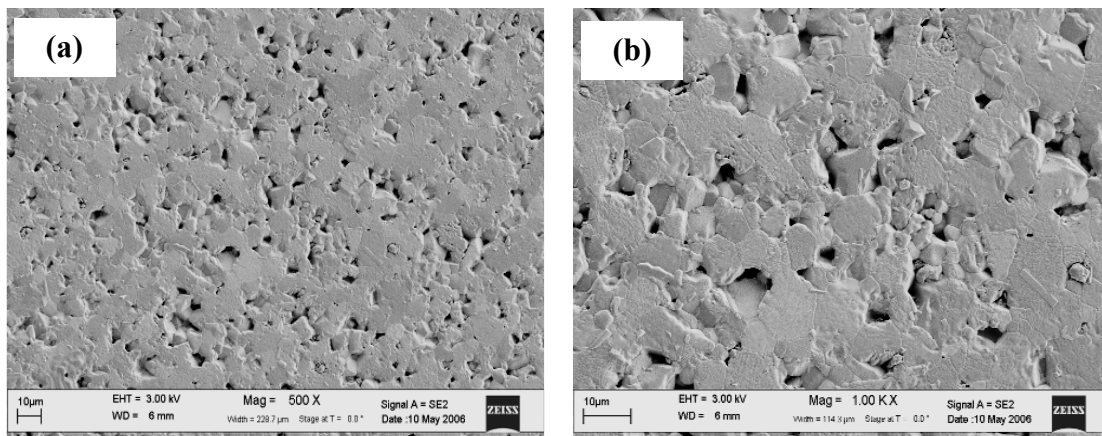


Figure 4.23 SEM micrographs of 4 mol% Bi modified  $\text{La}_{0.8}\text{Sr}_{0.2}\text{MnO}_3$  after sintering at  $1400^\circ\text{C}$  for 6 hrs, (a) at 500 X, (b) at 1 kX.

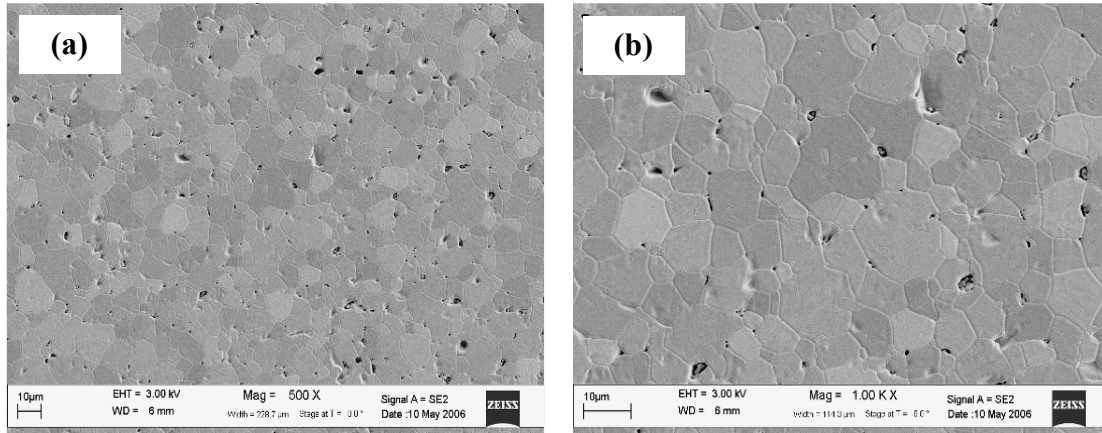


Figure 4.24 SEM micrographs of 6 mol% Bi modified  $\text{La}_{0.8}\text{Sr}_{0.2}\text{MnO}_3$  after sintering at  $1400^\circ\text{C}$  for 6 hrs, (a) at 500 X, (b) at 1 kX.

Table 4 Relative density values of A-site modified LSMO ceramics.

Composition	Density(g/cc)
$\text{La}_{0.78}\text{Li}_{0.02}\text{Sr}_{0.2}\text{MnO}_3$	5.58
$\text{La}_{0.76}\text{Li}_{0.04}\text{Sr}_{0.2}\text{MnO}_3$	6.27
$\text{La}_{0.74}\text{Li}_{0.06}\text{Sr}_{0.2}\text{MnO}_3$	6.1
$\text{La}_{0.78}\text{Bi}_{0.02}\text{Sr}_{0.2}\text{MnO}_3$	6.11
$\text{La}_{0.76}\text{Bi}_{0.04}\text{Sr}_{0.2}\text{MnO}_3$	6.18
$\text{La}_{0.74}\text{Bi}_{0.06}\text{Sr}_{0.2}\text{MnO}_3$	6.36



~300 K and it was observed that modification with 2 and 4 mol% Bi ions did not result in any significant change. As the Bi concentration was increased to 6 mol%, the Curie temperature was found to increase to around 325 K. The room temperature magnetic hysteresis loops with increasing percentage of Bi are shown in the Fig. 4.24. The samples with 2 mol% and 4 mol % were hard to saturate even with 1 Tesla applied magnetic field. The magnetic moment was found to increase with an increase in Bi percentage although for 4 mol% Bi it showed a decrease. The reason for this decrease is associated to the presence of large fraction of secondary phase. The trends for the Bi-modification should be interpreted from the data reported for the 2 and 4 mol% Bi-modification.

#### *4.2.2.4 Piezoresistivity*

The change in resistivity with external uniaxial pressure for Bi-modified samples is shown in Fig. 4.25. There is an increasing trend in resistivity with applied stress with an increase in Bi concentration. It was found that compared to the pure LSMO which shows a 0.5% change in resistivity at 19.2 MPa, 2 mol% Bi-modified samples showed a change in resistivity to 1.2%. The sign of the change in resistivity was opposite to that for pure LSMO. In general an increasing trend of piezoresistivity was found with increase in the dopant concentration. For 4 mol% Bi-modified LSMO the fractional change in resistivity increased to 1.8% and for 6 mol%Bi, it further increased to 2.4%. The change in resistivity with uniaxial stress was found to be non-linear.

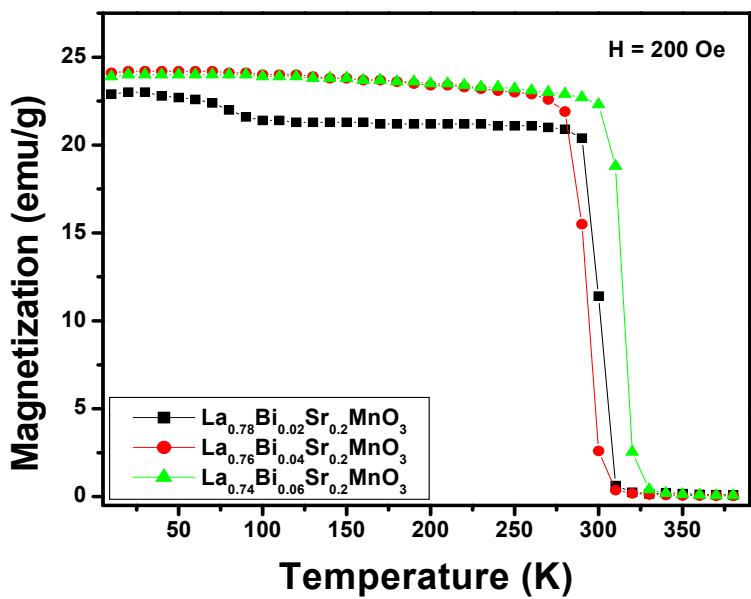


Figure 4.25 Temperature dependence of magnetization in bismuth modified  $\text{La}_{0.8}\text{Sr}_{0.2}\text{MnO}_3$  compositions.

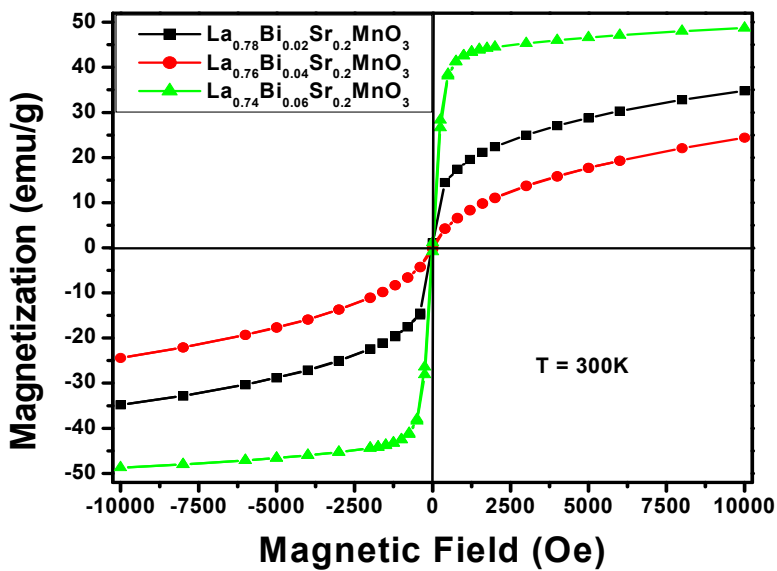


Figure 4.26 Room temperature magnetic hysteresis loops for bismuth modified  $\text{La}_{0.8}\text{Sr}_{0.2}\text{MnO}_3$  compositions.

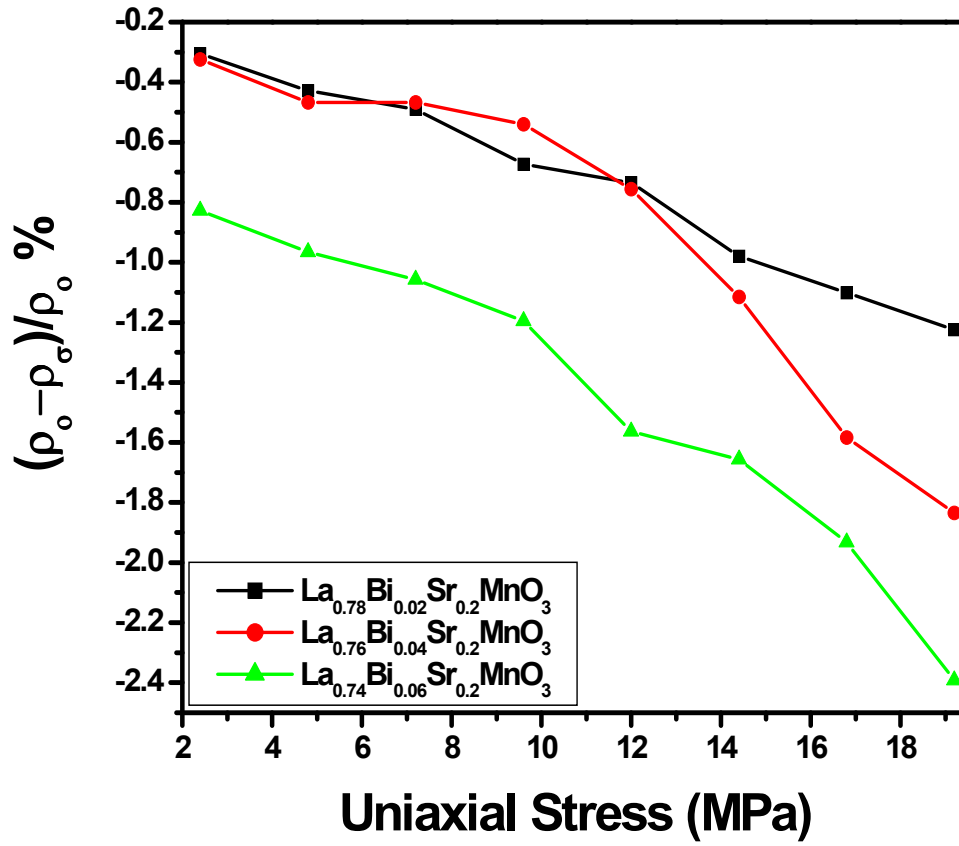


Figure 4.27 Piezoresistivity in Bi modified  $\text{La}_{0.8}\text{Sr}_{0.2}\text{MnO}_3$  compositions.

## 4.3 Effect of B-site dopants

### *4.3.1 Effect of copper*

#### *4.3.1.1 Crystal structure and phase determination*

The XRD pattern of calcined 2 mol% Cu-modified LSMO powder is shown in Fig. 4.26. The fraction of secondary phase was significantly small for powder calcined at 1025°C for 4 hrs. The XRD pattern of sintered samples is shown in Fig. 4.27 where the secondary phases are marked with an asterisk. Various sintering conditions were tried to obtain a relatively dense and pure perovskite phase. The optimized sintering condition was selected for synthesizing the samples which were used to measure the electrical and magnetic properties.

#### *4.3.1.2 Microstructures*

The effect of various sintering profiles on the microstructure development of 2 mol% Cu modified LSMO was characterized using SEM. Figure 4.28 shows that after sintering at 1200°C for 4 hrs, the sintering was not complete and no grain structure was developed. For enhancing the sintering, the powders were initially pressed into green bodies, under a cold isostatic pressure of 30 ksi and 40 ksi and the sintering temperature was raised to 1400°C for 4 hrs. The resulting microstructures are shown in Fig. 4.29. Figure 4.30 shows the optimized microstructures of the 2 mol% Cu composition, after optimizing the sintering temperature and time to 1400°C for 6 hrs. It was found that the level of porosity reduced significantly.

#### *4.3.1.3 Magnetic properties*

Since 2 mol % Cu modification in LSMO did not have an appreciable effect on

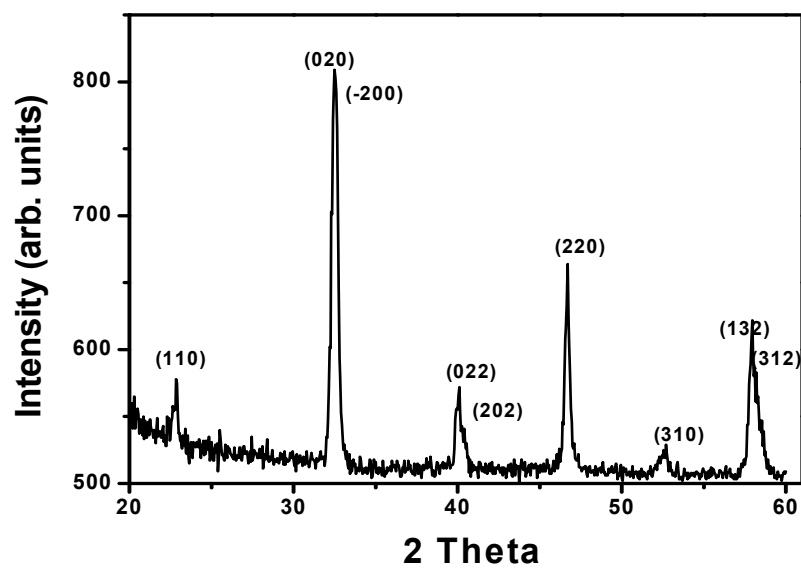


Figure 4.28 X-ray diffraction pattern for 2 mol% Cu modified  $\text{La}_{0.8}\text{Sr}_{0.2}\text{MnO}_3$  after calcination at  $1025^\circ\text{C}$  for 4 hrs.

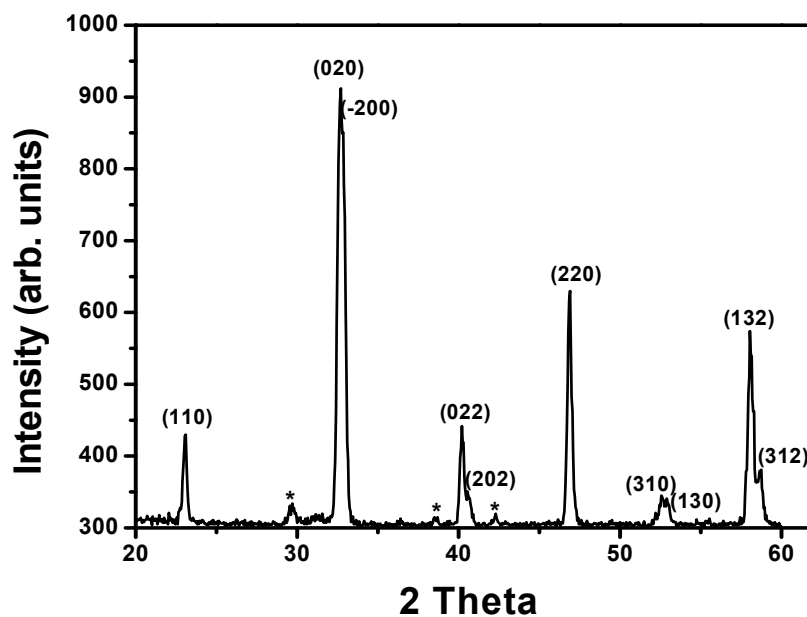


Figure 4.29 X-ray diffraction pattern for 2 mol% Cu modified  $\text{La}_{0.8}\text{Sr}_{0.2}\text{MnO}_3$  after sintering at  $1400^\circ\text{C}$  for 6 hrs.

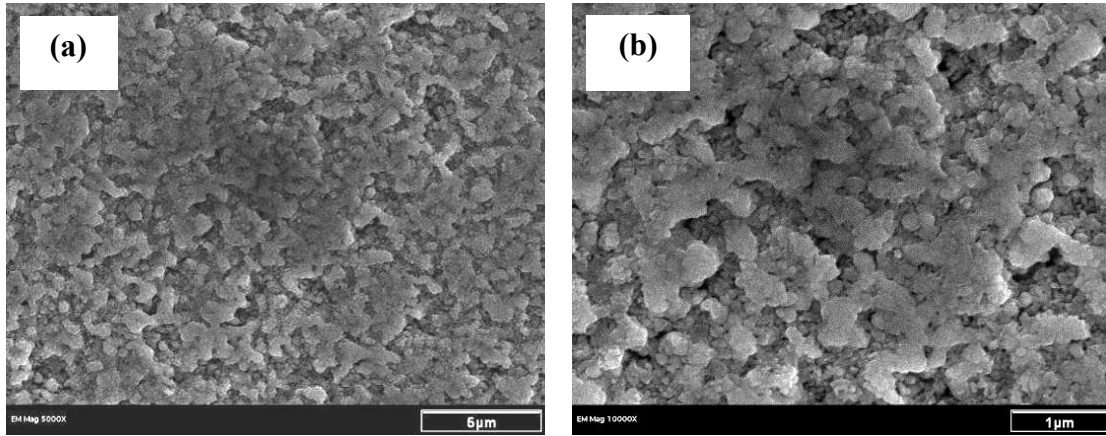


Figure 4.30 SEM micrographs of 2 mol% Cu modified  $\text{La}_{0.8}\text{Sr}_{0.2}\text{MnO}_3$  after sintering at  $1200^\circ\text{C}$  for 4 hrs, (a) at 1 kX, (b) at 5 kX.

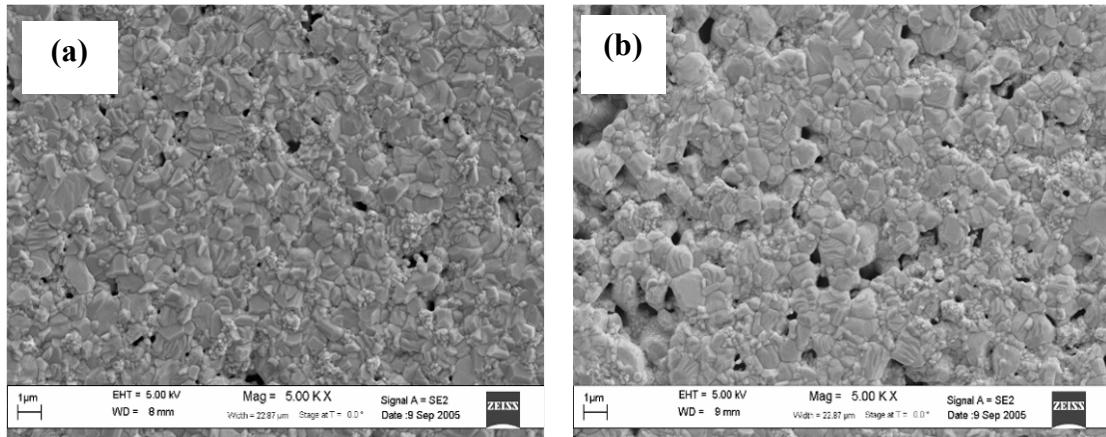


Figure 4.31 SEM micrographs of 2 mol% Cu modified  $\text{La}_{0.8}\text{Sr}_{0.2}\text{MnO}_3$  after sintering at  $1400^\circ\text{C}$  for 4 hrs pressed at (a) 30 ksi and (b) 40 ksi.

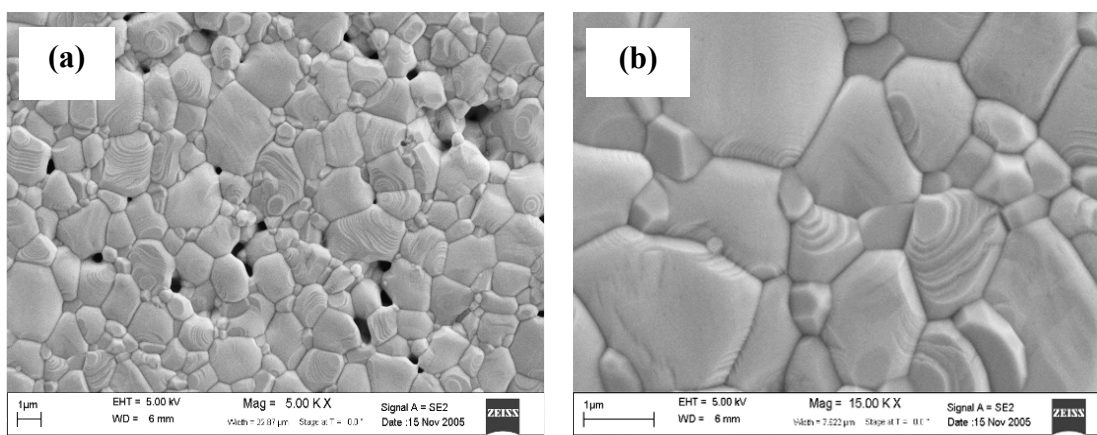


Figure 4.32 SEM micrographs of 2 mol% Cu modified  $\text{La}_{0.8}\text{Sr}_{0.2}\text{MnO}_3$  after sintering at  $1400^\circ\text{C}$  for 6 hrs, (a) at 5 kX and (b) 15 kX.

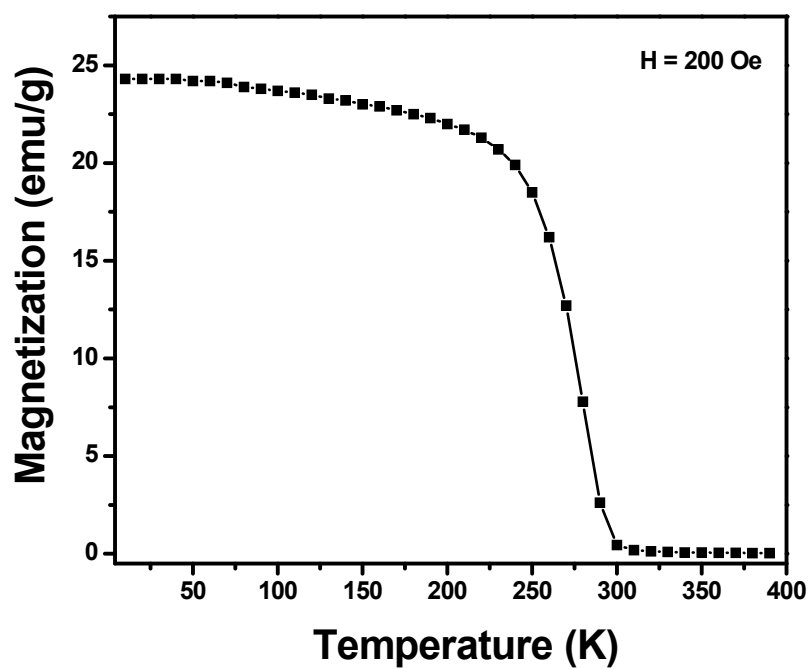


Figure 4.33 Temperature dependence of magnetization in 2 mol% Cu modified  $\text{La}_{0.8}\text{Sr}_{0.2}\text{MnO}_3$ .

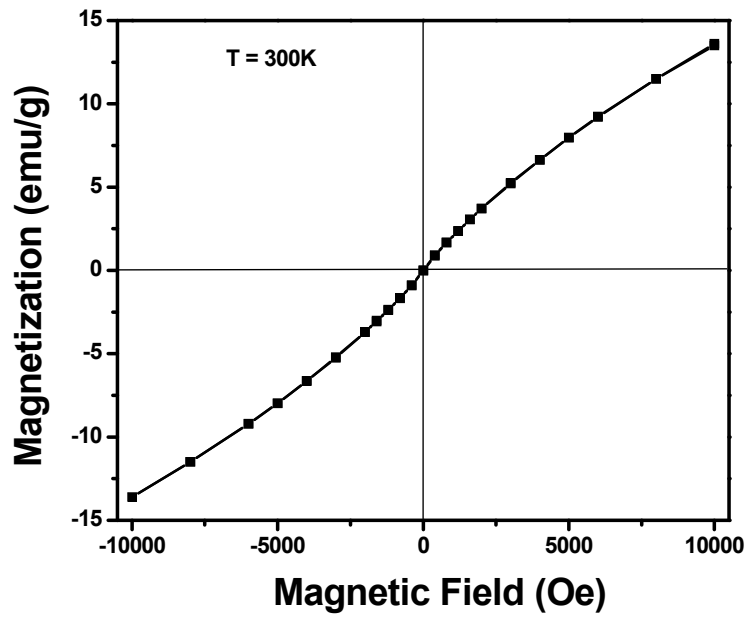


Figure 4.34 Room temperature magnetic hysteresis loops for 2 mol% Cu modified  $\text{La}_{0.8}\text{Sr}_{0.2}\text{MnO}_3$ .

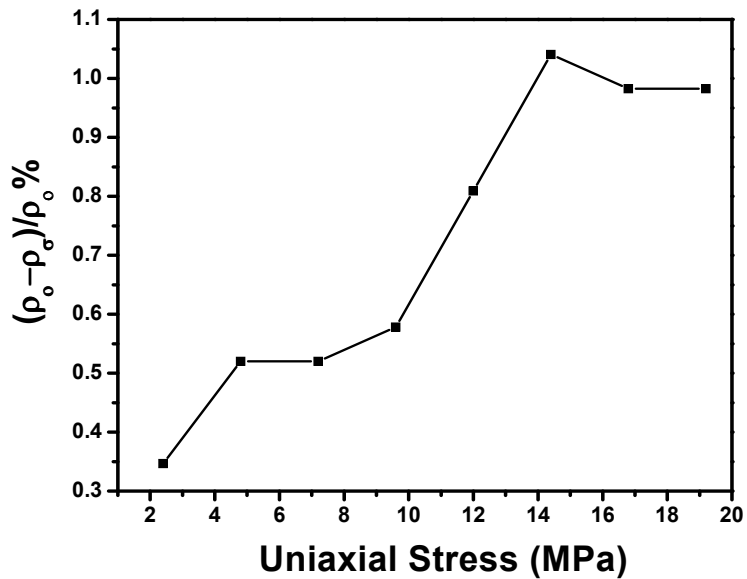


Figure 4.35 Piezoresistivity in 2 mol% Cu modified  $\text{La}_{0.8}\text{Sr}_{0.2}\text{MnO}_3$ .



the ferromagnetic Curie temperature. The Curie temperature after copper doping remained near 300K which is close to that of pure LSMO. The room temperature magnetic hysteresis loop is shown in Fig. 4.32 which demonstrates that the magnetization decreased as compared to that of pure composition and the material remained ferromagnetic at room temperature.

#### *4.3.1.4 Piezoresistivity*

The change in resistivity with uniaxial stress was found to be positive for Cu-modified composition similar to the case of pure LSMO. It was found that although the addition of 2 mol% Cu increased the fractional change in resistivity, the change was found to be non linear, and the data was not suitable for use in a force sensing application. The total fractional change in resistivity at a uniaxial stress of 19.2 MPa, in pure composition was around +0.5%, while after doping 2 mol% Cu, it increased to around +1.0 %. The piezoresistivity of Cu modified LSMO is shown in Fig. 4.33.

#### *4.3.2 Effect of niobium*

##### *4.3.2.1 Crystal structure and phase determination*

The XRD patterns for both the 2 mol% and 5 mol% modified LSMO powders calcined at 1025°C for 4 hrs are shown in Fig. 4.34. A presence of a secondary phase was detected after calcination. After sintering at 1400°C for 6 hrs in air under atmospheric pressure, small amount of secondary phase was inevitable. The x-ray diffraction pattern of the sintered Nb modified ceramics is shown in Fig. 4.35. The effect of B-site doping with Cu and Nb on the XRD peaks of pure  $\text{La}_{0.8}\text{Sr}_{0.2}\text{MnO}_3$

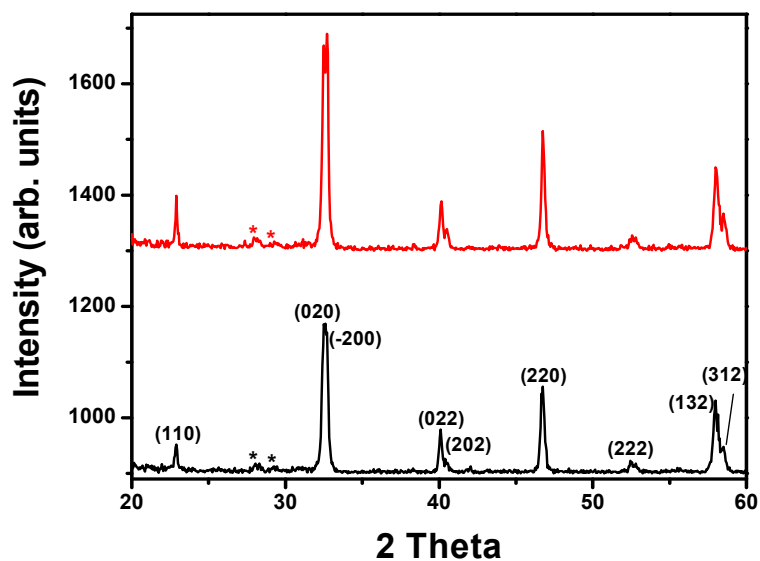


Figure 4.36 X-ray diffraction patterns of calcined powders of Nb modified  $\text{La}_{0.8}\text{Sr}_{0.2}\text{MnO}_3$  compositions.

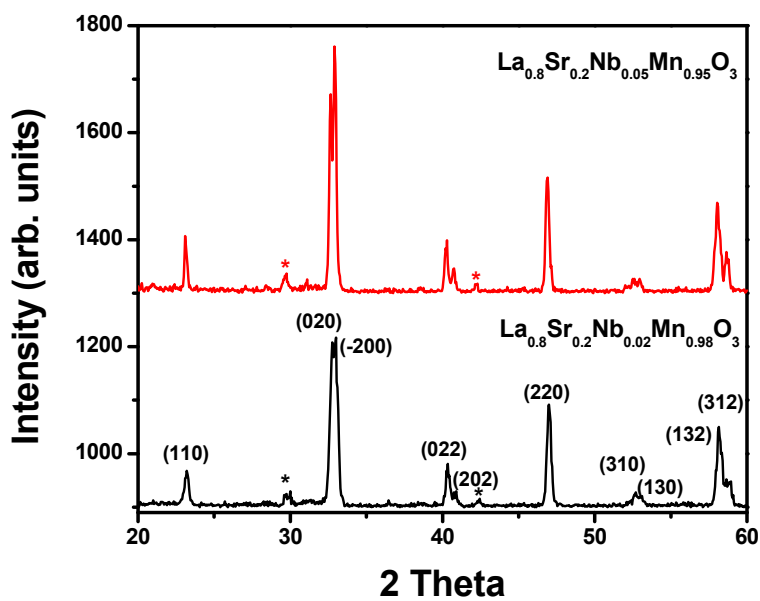


Figure 4.37 X-ray diffraction patterns of sintered samples of Nb modified  $\text{La}_{0.8}\text{Sr}_{0.2}\text{MnO}_3$  compositions, after sintering at  $1400^\circ\text{C}$  for 6 hrs.

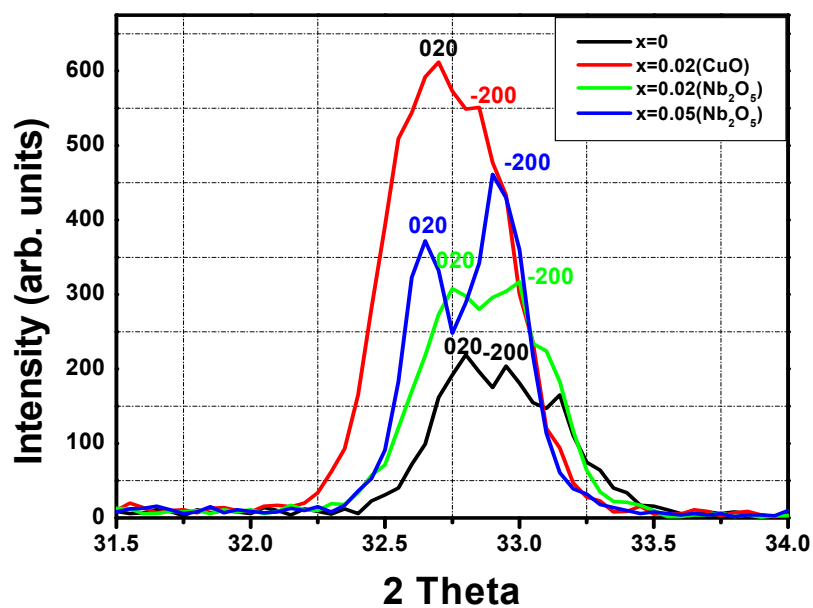


Figure 4.38 Peak shifts in the (020) and ( $\bar{2}00$ ) reflections with B-site modification.

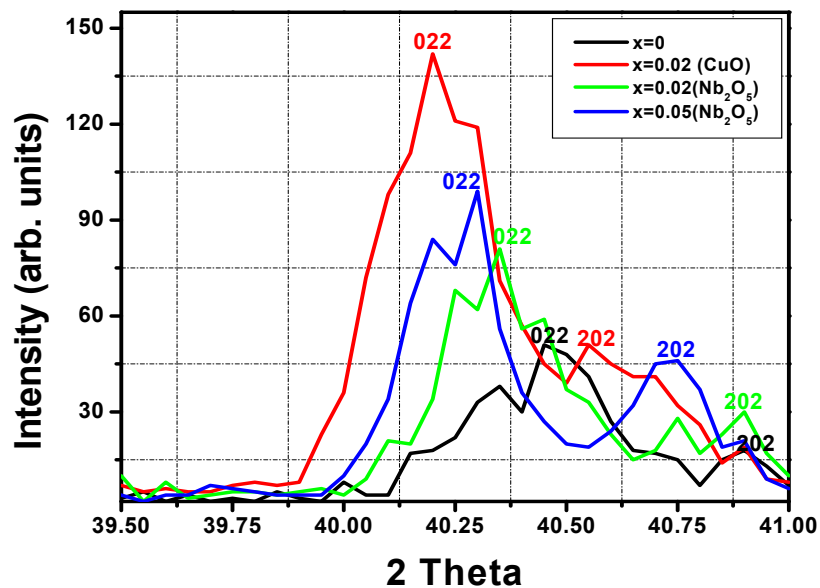


Figure 4.39 Peak shifts in the (022) and (202) reflections with B-site modification.

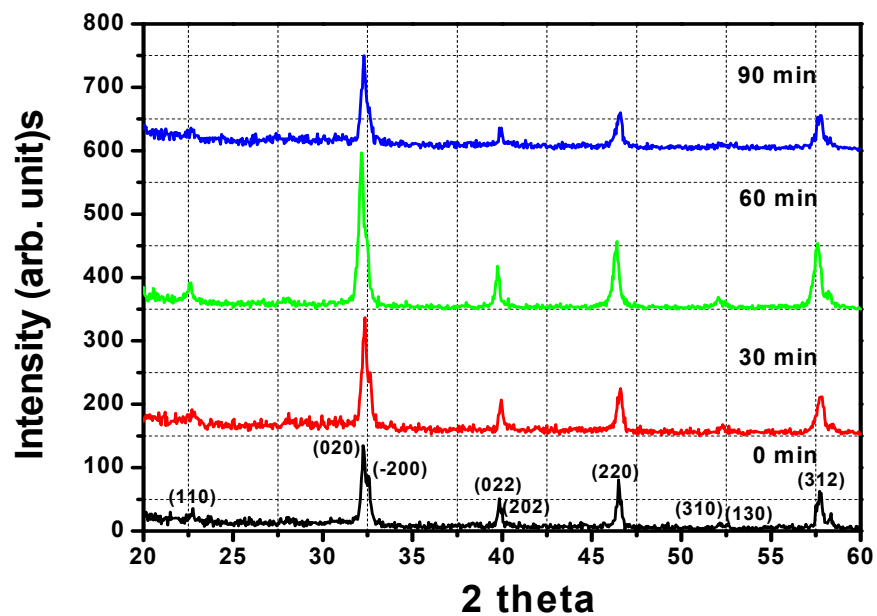


Figure 4.40 Effect of pressing time on the XRD peaks of  $\text{La}_{0.8}\text{Sr}_{0.2}\text{Nb}_{0.05}\text{Mn}_{0.95}\text{O}_3$  at 15 MPa uniaxial pressure.

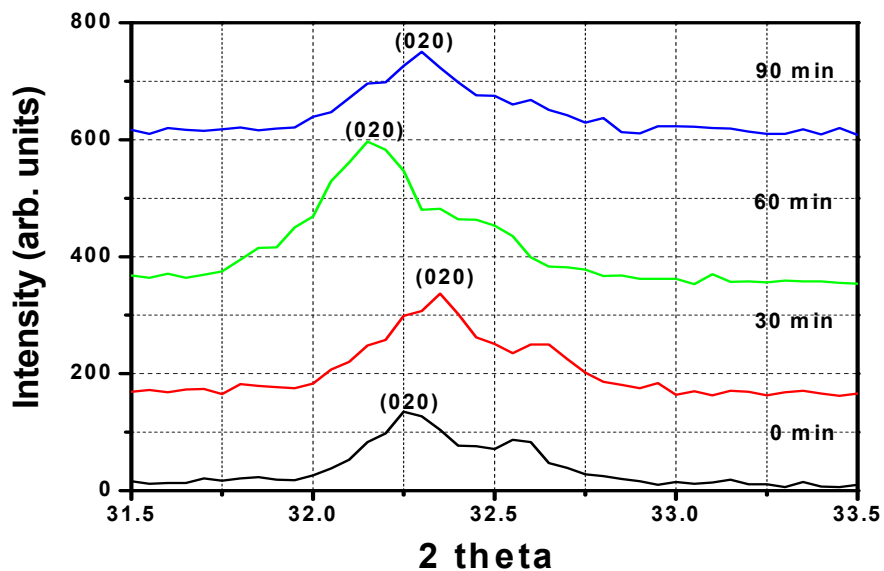


Figure 4.41 Peak shifts in the (020) reflections of  $\text{La}_{0.8}\text{Sr}_{0.2}\text{Nb}_{0.05}\text{Mn}_{0.95}\text{O}_3$  with pressing time at 15 MPa uniaxial pressure.

are compared in the Figs. 4.36 and 4.37. It can be seen that with doping on the Mn-sites, the high intensity peaks are from (020) and (-200) planes are shifted to lower  $2\theta$  values. A similar trend was found for the other two reflections from the (022) and (202) planes.

#### *4.3.2.2 Microstructures*

A series of experiments were carried out for optimizing the sintering conditions of the Nb-modified LSMO compositions. The sintering temperature was varied from 1300°C to 1400°C with varying holding times from 4 hrs to 6 hrs. It was found that the magnitude of cold isostatic pressure has an appreciable effect on the sintering, which was varied from 30 ksi to 40 ksi. For 2 mol% Nb, the results for sintering at 1300°C and 4 hrs are shown in the Figs. 4.38 (a) and 4.38(b). Figures 4.38(c) and 4.38(d) show that, after increasing the sintering temperature to 1400°C the density of the samples increased, with significant improvement in the microstructures. Next, the sintering temperature was kept the same, at 1400°C and the holding time was increased to 6 hrs, and a significant improvement in the sintering was observed after CIP at 40 ksi as is evident from the micrographs shown in Fig. 4.39.

The compositions with 5 mol% Nb were also synthesized under various sintering conditions. It was found that the CIP pressure, sintering time and temperature had a significant effect on the microstructures of these compositions. Figures 4.40 (a) and 4.40(b) shows the effect of sintering at 1300°C for 4 hrs at 30 ksi and 40 ksi respectively. The effect of increasing the sintering temperature to 1400°C and pressing pressure from 30 ksi to 40 ksi is shown in Figs. 4.40 (c) and 4.40(d). The sintering

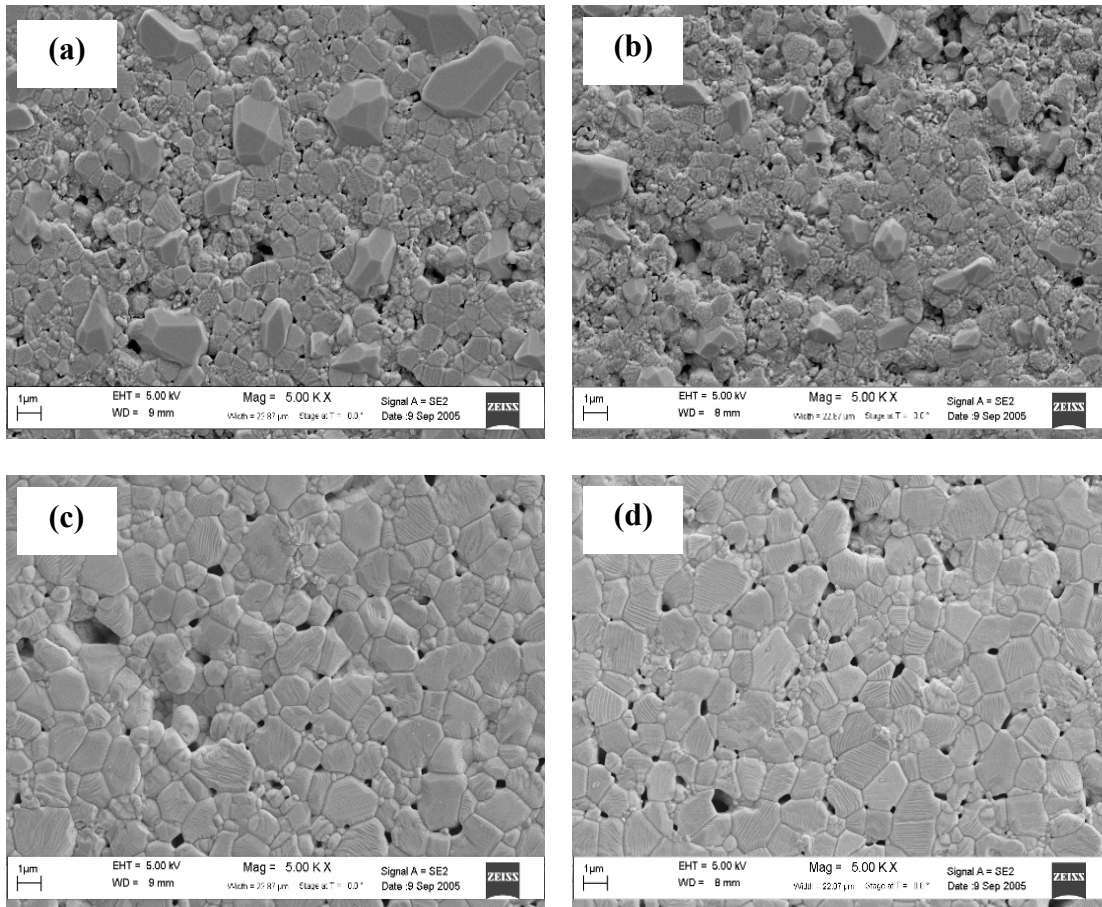


Figure 4.42 SEM micrographs for 2 mol% Nb modified  $\text{La}_{0.8}\text{Sr}_{0.2}\text{MnO}_3$  after sintering at  $1300^\circ\text{C}$  for 4 hrs pressed at (a) 30 ksi and (b) 40 ksi; and  $1400^\circ\text{C}$  for 4 hrs pressed at (c) 30 ksi and, (d) 40 ksi.

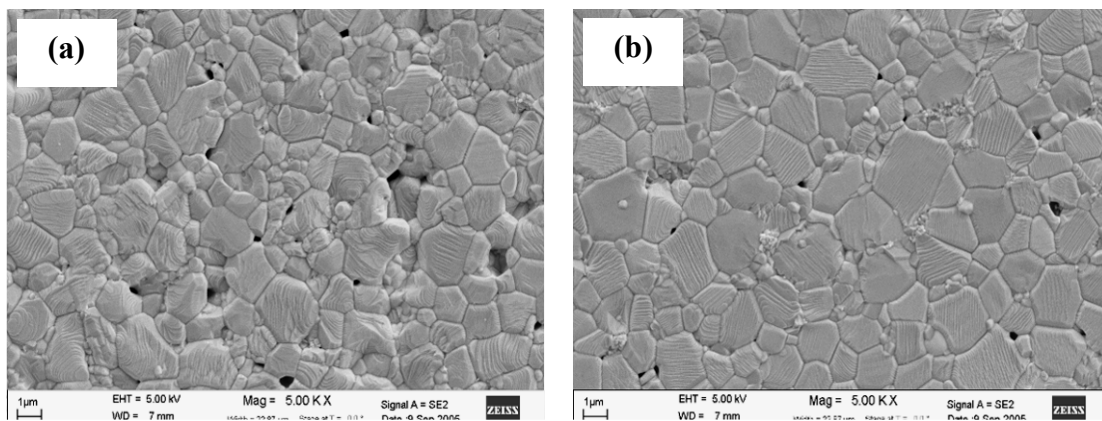


Figure 4.43 SEM micrographs of 2 mol% Nb modified composition sintered at  $1400^\circ\text{C}$  6 hrs after pressing at (a) 30 ksi and (b) 40 ksi CIP pressure.

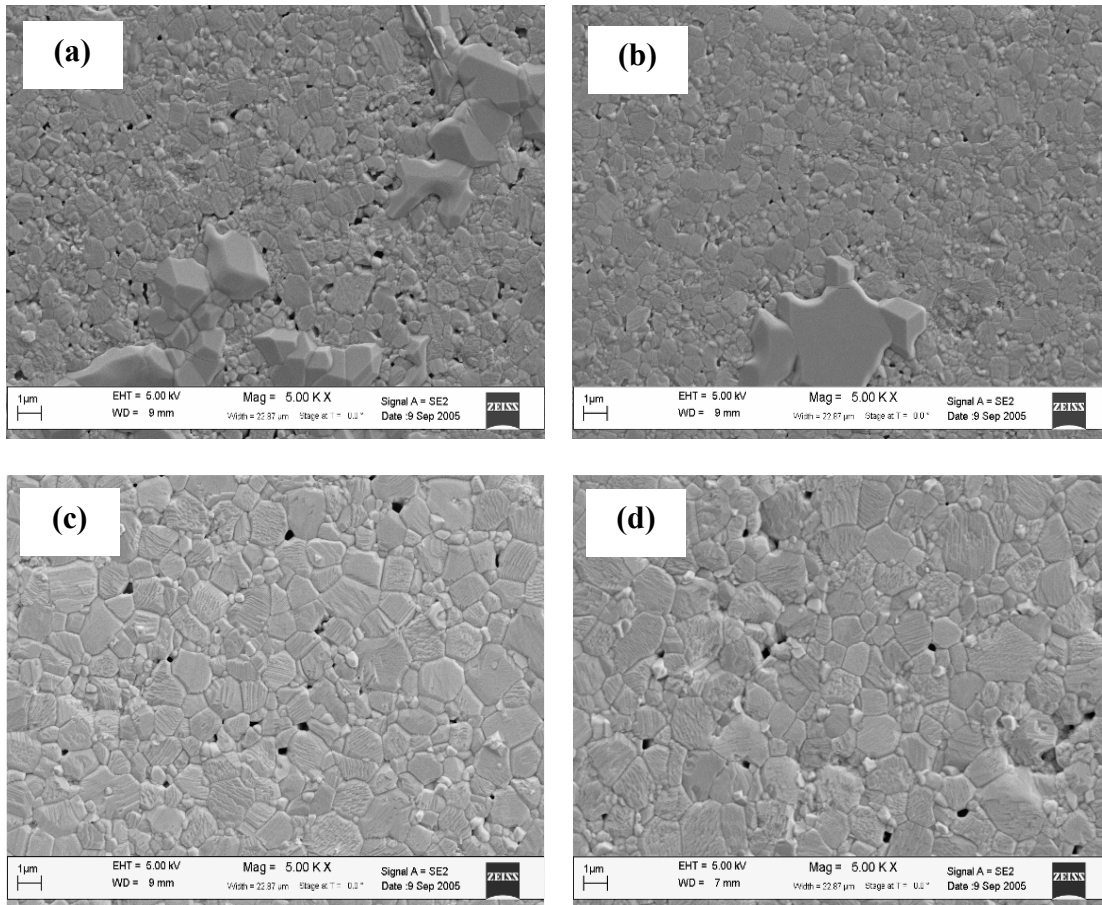


Figure 4.44 SEM micrographs for 5 mol% Nb modified  $\text{La}_{0.8}\text{Sr}_{0.2}\text{MnO}_3$  after sintering at  $1300^\circ\text{C}$  for 4 hrs pressed at (a) 30 ksi, (b) 40 ksi and  $1400^\circ\text{C}$  for 4 hrs pressed at (c) 30 ksi, (d) 40 ksi CIP pressure.

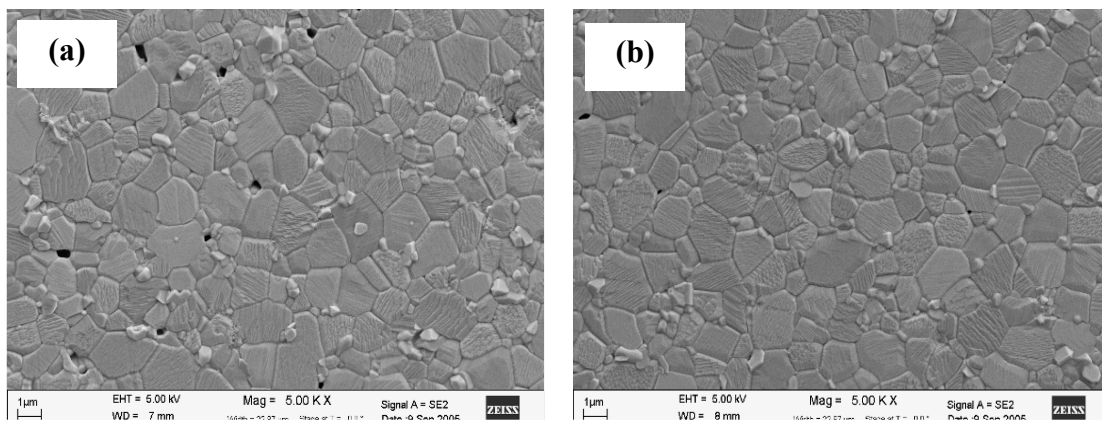


Figure 4.45 SEM micrographs of 5 mol% Nb modified composition sintered at  $1400^\circ\text{C}$  for 6 hrs and pressed at (a) 30 ksi and (b) 40 ksi CIP pressure.

parameters were optimized as 1400°C for 6 hrs with a CIP pressure of 40 ksi, as shown in Fig. 4.41 <sup>[17]</sup>.

#### *4.3.2.3 Magnetic properties*

The zero field cooled temperature dependence of magnetic moment was measured in the temperature range of 4 K – 390 K. A large drop in the Curie temperature was found. The effect of doping 2 mol% Nb was to decrease the Curie temperature to 290 K, and when the Nb concentration was increased to 5 mol% the Curie temperature further dropped to 220 K. A comparison of the magnetic properties of Nb modified compositions with pure LSMO is shown in Fig. 4.42. A room temperature magnetic hysteresis loop with a maximum magnetic field of 1 Tesla is shown in Fig. 4.43. The hysteresis loops confirm the fact that the material is paramagnetic at room temperature. Similar results have been reported by Huang et al.<sup>[18]</sup> for the magnetic property dependence with Nb concentration.

#### *4.3.2.4 Piezoresistivity*

A giant enhancement in the piezoresistive properties of LSMO was observed in the compositions with Nb. Similar to the effect of doping copper ions on the Mn-sites, a positive change in electrical resistivity with uniaxial stress was observed in case of niobium. The 2 mol% Nb doped composition showed an increase of fractional change in resistivity from +0.5% for pure LSMO to around +2.0%. Although the change is significant as compared to the pure LSMO, the change was non linear and the magnitude is not enough for being used as a force sensor material. A giant enhancement in the piezoresistivity of LSMO was observed after doping it with 5 mol% Nb. A



fractional change in resistivity of +3.0% was observed at a uniaxial stress of 19.2 MPa. The change was found to be linear with respect to external stress. This result is promising for application as a force sensor. To further explore the possibility of increase in piezoresistivity with dopant concentration, the Nb concentration was increased to 10 mol%. However, no significant improvement in the piezoresistivity was found although the observed change was linear. A comparison of the observed change in Nb modified compositions is shown in Fig. 4.44.

Table 5 Relative density values of B-site modified LSMO ceramics.

Composition	Density(g/cc)
$\text{La}_{0.8}\text{Sr}_{0.2}\text{MnO}_3$	5.87
$\text{La}_{0.8}\text{Sr}_{0.2}\text{Cu}_{0.02}\text{Mn}_{0.98}\text{O}_3$	5.83
$\text{La}_{0.8}\text{Sr}_{0.2}\text{Nb}_{0.02}\text{Mn}_{0.98}\text{O}_3$	5.88
$\text{La}_{0.8}\text{Sr}_{0.2}\text{Nb}_{0.05}\text{Mn}_{0.95}\text{O}_3$	6.32

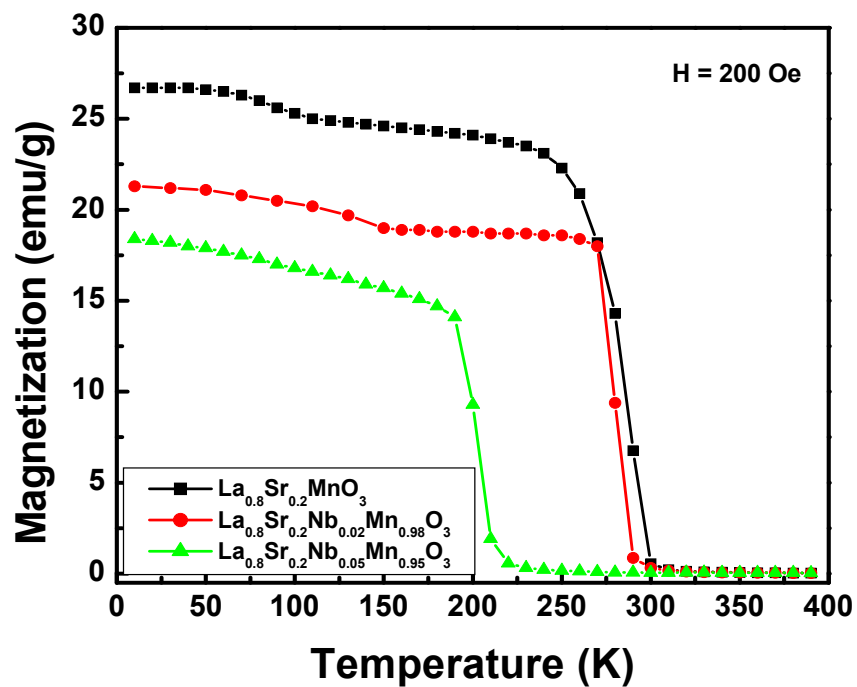


Figure 4.46 Temperature dependence of magnetization for Nb modified  $\text{La}_{0.8}\text{Sr}_{0.2}\text{MnO}_3$  compositions.

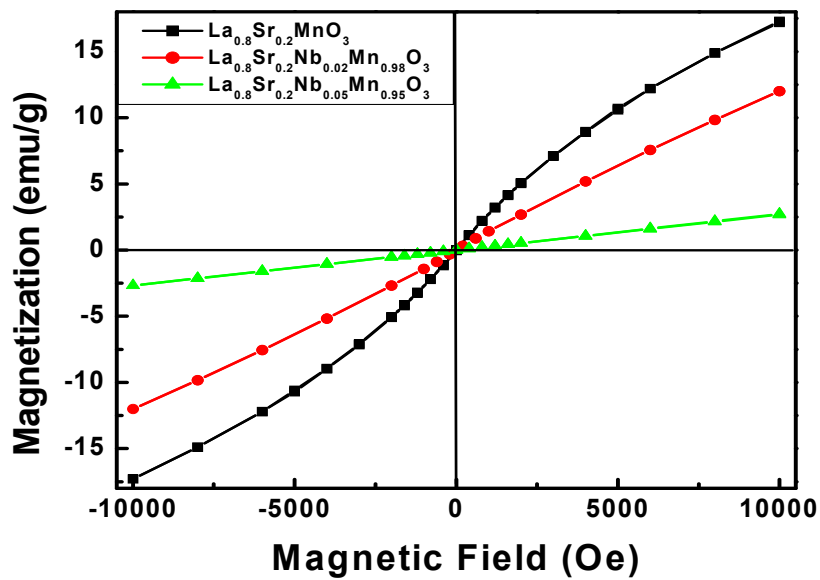


Figure 4.47 Room temperature magnetic hysteresis loops for Nb modified  $\text{La}_{0.8}\text{Sr}_{0.2}\text{MnO}_3$  compositions.

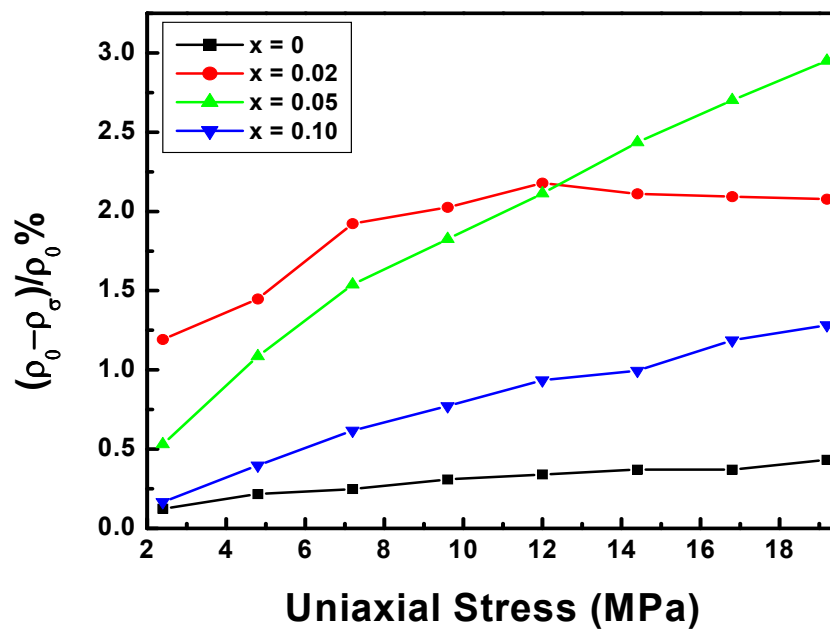


Figure 4.48 Piezoresistivity in Nb-modified  $\text{La}_{0.8}\text{Sr}_{0.2}\text{MnO}_3$  ceramics at different concentrations of Nb

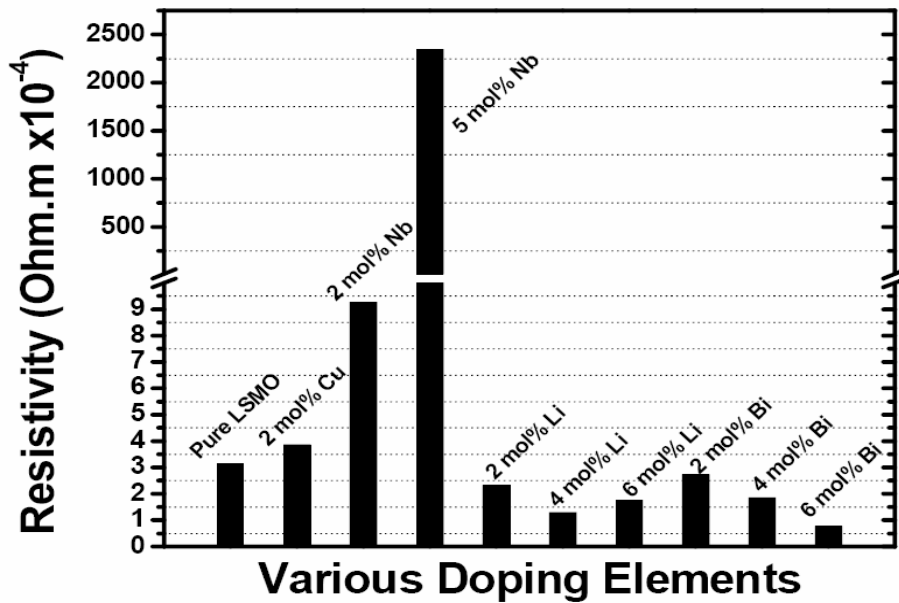


Figure 4.49 Comparison of the resistivity values after A and B site modification in  $\text{La}_{0.8}\text{Sr}_{0.2}\text{MnO}_3$  ceramics.

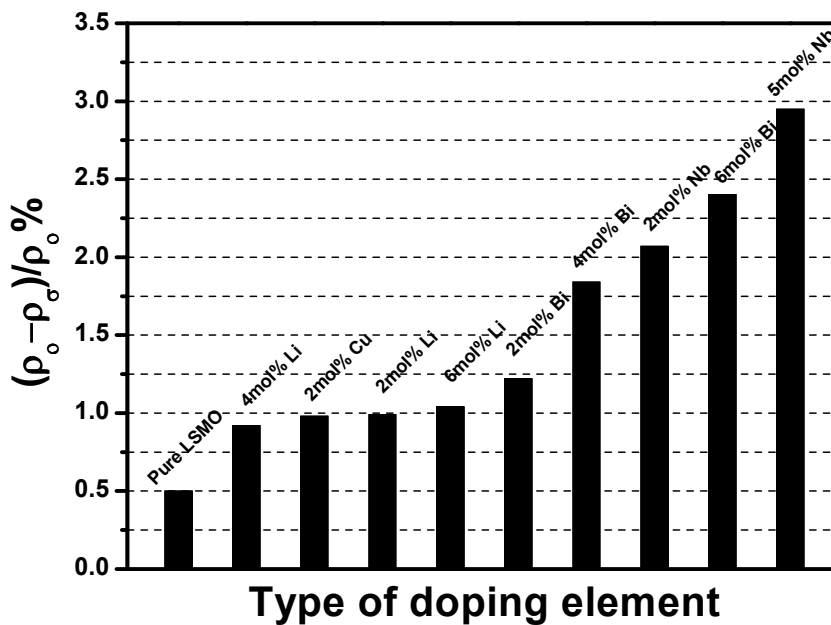


Figure 4.50 Comparison of the piezoresistive behavior after A and B site modification in  $\text{La}_{0.8}\text{Sr}_{0.2}\text{MnO}_3$  ceramics.

## CHAPTER 5

### PIEZORESISTIVITY BEHAVIOR OF $\text{La}_{0.8}\text{Sr}_{0.2}\text{MnO}_3$ – PARTIALLY STABILIZED ZIRCONIA COMPOSITE

#### 5.1 Mechanical properties of ceria stabilized $\text{ZrO}_2$

Pure zirconium oxide exists as a monoclinic phase at room temperature. However, for practical applications, the monoclinic phase is unsuitable due to a monoclinic to tetragonal phase transformation occurring at  $1170^\circ\text{C}$ . This phase transformation is accompanied by a 5% change in volume, which limits the use of this material. However the tetragonal phase can be stabilized at room temperature by addition of certain metal oxides as stabilizers. Ceria stabilized zirconia polycrystalline ceramics have been shown to exhibit extremely high mechanical strength. It has been observed that the transformable metastable tetragonal phase increases with the  $\text{CeO}_2$  content and has significant effects on the mechanical properties of Ceria stabilized zirconia.

Figure 5.1 shows the microstructures of the 12 mol%  $\text{CeO}_2$  stabilized  $\text{ZrO}_2$  after sintering at  $1350^\circ\text{C}$  and  $1400^\circ\text{C}$  for 6 hrs. The two compositions were found to have a tetragonal crystal structure as shown in Fig. 5.2. The effect of  $\text{CeO}_2$  content on the fracture toughness and hardness of these ceramics studied by Sharma et al <sup>[35]</sup> is shown in Fig. 5.3. They observed that at 12 mol%  $\text{CeO}_2$  the flexural strength and fracture toughness is maximum, and is around 725 MPa and  $15 \text{ MPa}\sqrt{\text{m}}$  respectively.

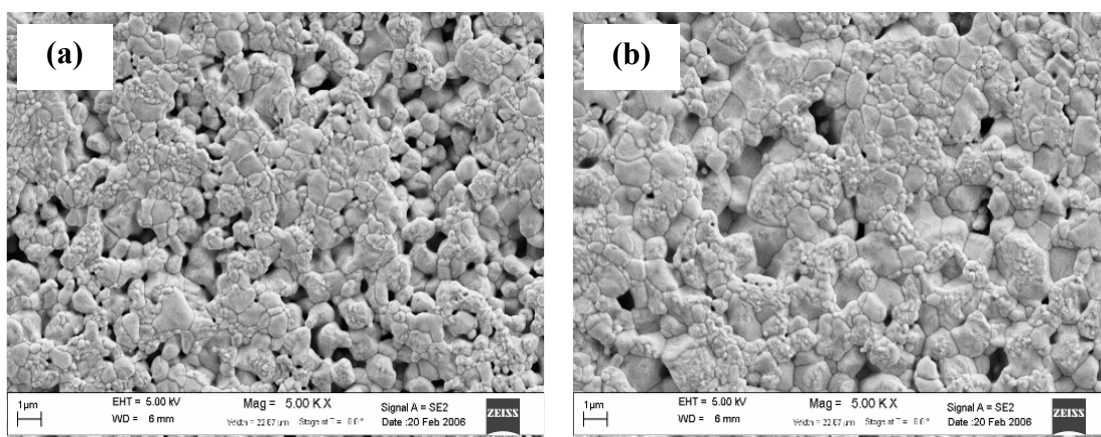


Figure 5.1 12 mol% CeO<sub>2</sub> stabilized ZrO<sub>2</sub>, after sintering at (a) 1350°C and (b) 1400°C for 6 hrs.

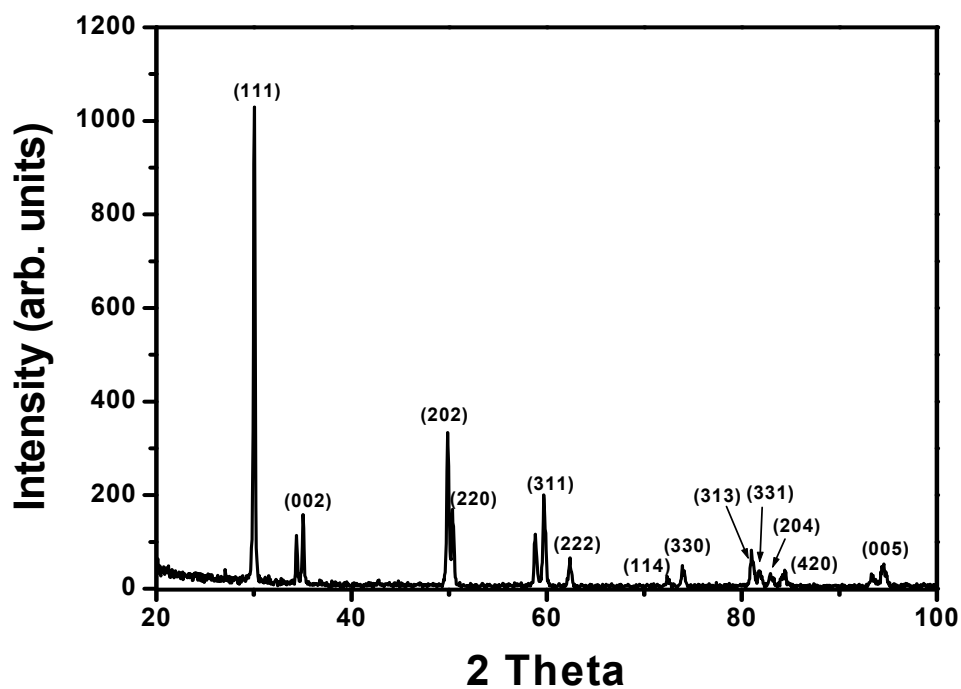


Figure 5.2 X-ray diffraction pattern for partially stabilized zirconia showing a tetragonal structure.

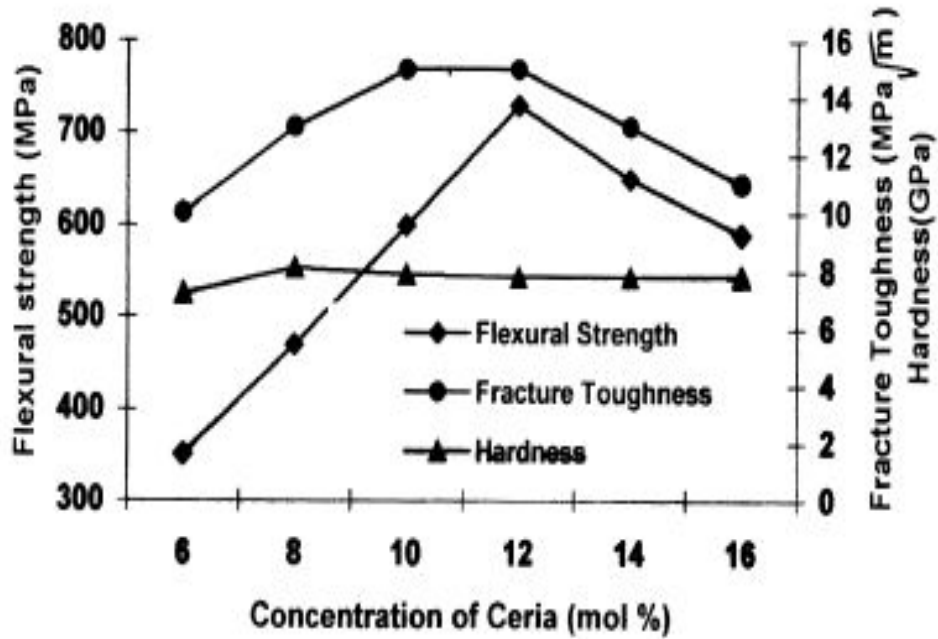


Figure 5.3 Variation of mechanical properties with CeO<sub>2</sub> concentration in CeO<sub>2</sub> stabilized ZrO<sub>2</sub> ceramics <sup>[35]</sup>.

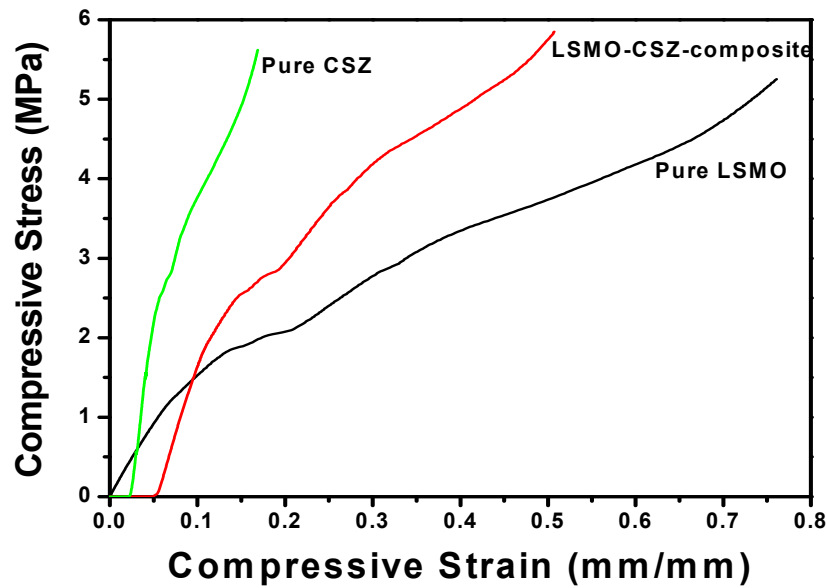


Figure 5.4 A comparison of the stress-strain behavior of pure LSMO, partially stabilized zirconia and LSMO-ZrO<sub>2</sub> composite.

However, there was a little effect on the hardness values. The high strength and toughness in these ceramics is related to the transformation toughening mechanism.

## 5.2 Properties of $\text{La}_{0.8}\text{Sr}_{0.2}\text{MnO}_3$ – partially stabilized $\text{ZrO}_2$ composite

### *5.2.1 Mechanical properties*

A mechanically tough composite material showing excellent force sensing capabilities was synthesized by mixing  $\text{La}_{0.8}\text{Sr}_{0.2}\text{MnO}_3$  ceramic powder and a  $\text{CeO}_2$  stabilized  $\text{ZrO}_2$  powder. High strength and toughness is required due to the harsh environments faced in automotive applications. Also, a high force sensing material is highly desirable in these conditions. The composite of LSMO and partially stabilized  $\text{ZrO}_2$  is expected to have high fracture toughness and strength. A non-standard compressive test using an Instron<sup>®</sup> microtester was conducted for the pure LSMO, partially stabilized  $\text{ZrO}_2$  and the LSMO- $\text{ZrO}_2$  composite. The results are shown in the Fig. 5.4. These results indicate a trend that shows that the composite material has adequate toughness and strength as compared to its parent counterparts.

### *5.2.2 Microstructural properties*

Figure 5.5 shows the microstructure of the  $\text{La}_{0.8}\text{Sr}_{0.2}\text{MnO}_3$  - partially stabilized zirconia composite. It can be seen that the LSMO grains are well dispersed in a partially stabilized zirconia matrix. Although the grain boundaries seem to be fractured, the morphology of the grain boundaries was uniquely thick and distinct. The soft LSMO grains existing in the grain boundaries and grain boundary triple junctions, in a tough matrix of partially stabilized tetragonal structure, are responsible for the high fracture toughness and mechanical compressive strength of the composite material.



The presence of a partially stabilized zirconia and LSMO phase was confirmed by x-ray diffraction. The XRD pattern for pure LSMO- partially stabilized zirconia composite is shown in Fig. 5.6. The 12 mol% ceria- doped zirconia was found to exist in a tetragonal partially stabilized state. It was found that there was some degree of inter-diffusion between the LSMO and the ZrO<sub>2</sub> rich phases, as a result, the grains of LSMO at the grain boundaries showed the presence of Zr, and Ce in minor amounts. Similarly, a small amount of La, Sr, and Mn, was found in the ZrO<sub>2</sub> matrix. This fact is confirmed by a TEM analysis, as shown in the section 7.3. Also, the surface of this composite material showed the presence of a nanoporous layer, discussed in detail in later. For the mechanical property and piezoresistivity studies, the surface nanoporous layer was polished and removed.

### *5.2.3 Piezoresistivity*

Piezoresistivity in the LSMO – partially stabilized zirconia composite was studied using the same methods and techniques as discussed earlier. The La<sub>0.8</sub>Sr<sub>0.2</sub>MnO<sub>3</sub> – partially stabilized zirconia had a resistivity of about  $8.5 \times 10^{10}$  Ωcm. The results for the piezoresistivity measurements are as shown in Fig. 5.7 and seemed to show an ambiguity because an extremely large change in resistivity of the order of -200% was observed, which needs further investigation and confirmation. The results are shown for two different samples of same size, conducted in the same manner with a 3 min holding time and also a continuous test without any holding time was done. Large changes in resistivity values need further investigation for confirmation.

Although, the  $\text{La}_{0.8}\text{Sr}_{0.2}\text{Nb}_{0.05}\text{Mn}_{0.95}\text{O}_3$  – partially stabilized zirconia showed more reliable results and a total change in resistivity at a uniaxial stress of 17.8 MPa was found to be around -10 % which is a dramatically large change. The resistivity of this composite was found to be around  $10.26 \times 10^8 \Omega\text{cm}$ . The measurements conducted on two samples are shown in Fig. 5.8. It should be noted here that resistance values were measured using a high resistance electrometer and for a Tera-Ohm resistance range, accurate values of resistance can be obtained after applying a voltage between 400 V to 1000 V, and a low value of current in the nano-ampere range. At such high voltages, extraneous currents and losses can occur. So the data need to be further checked for accuracy. It is also to be noted that the change in resistivity with stress in this material was found to be negative, opposite to that of pure LSMO and 5 mol%Nb doped LSMO compositions. This result may be attributed to the unique microstructural properties and inter-diffusion phenomena in this material. But no conclusion can be drawn until this point and further investigations need to be done on this composite material.

#### *5.2.4 Problems and success of the composite*

It is evident from the above discussion, the tough composite synthesized for use as a force sensor material in harsh environments of high temperature and pressure, showed a remarkable strength and toughness. Extremely large changes in the resistivity values suggest that this material has potential applications as a force sensor material in harsh environments.

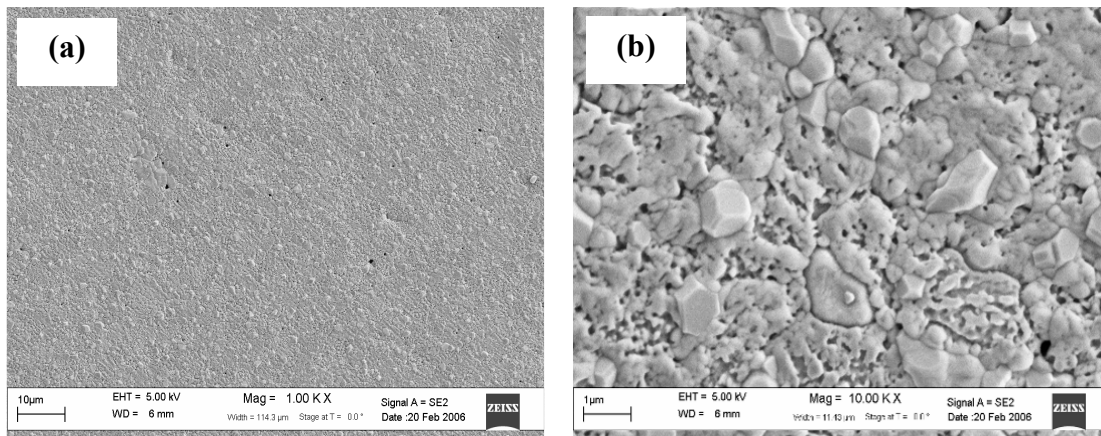


Figure 5.5 SEM micrographs of the LSMO- partially stabilized composite sintered at 1300°C for 6 hrs at (a) 1 kX and (b) 10 kX respectively.

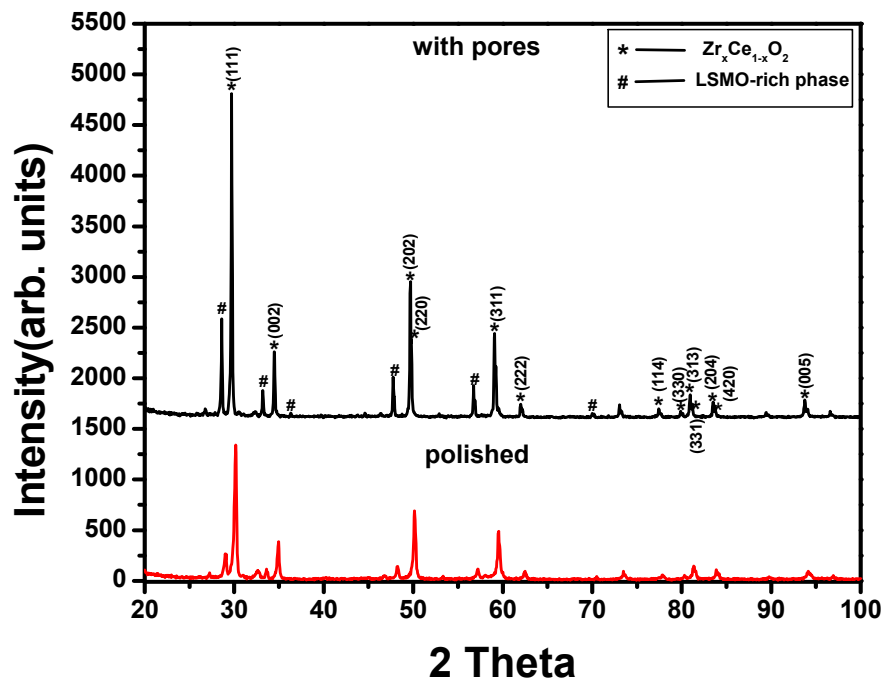


Figure 5.6 X-ray diffraction pattern of the composite material with and without porous surface layer.

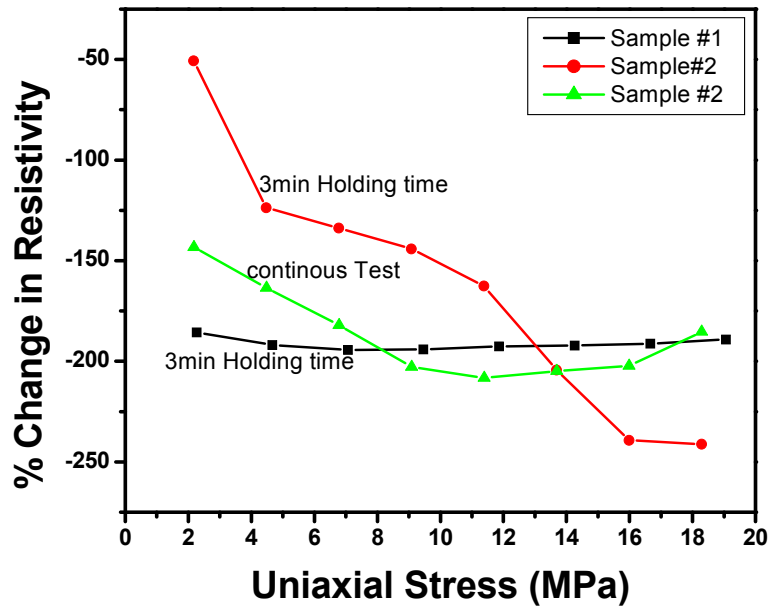


Figure 5.7 Piezoresistivity in  $\text{La}_{0.8}\text{Sr}_{0.2}\text{MnO}_3$  – partially stabilized  $\text{ZrO}_2$  composite.

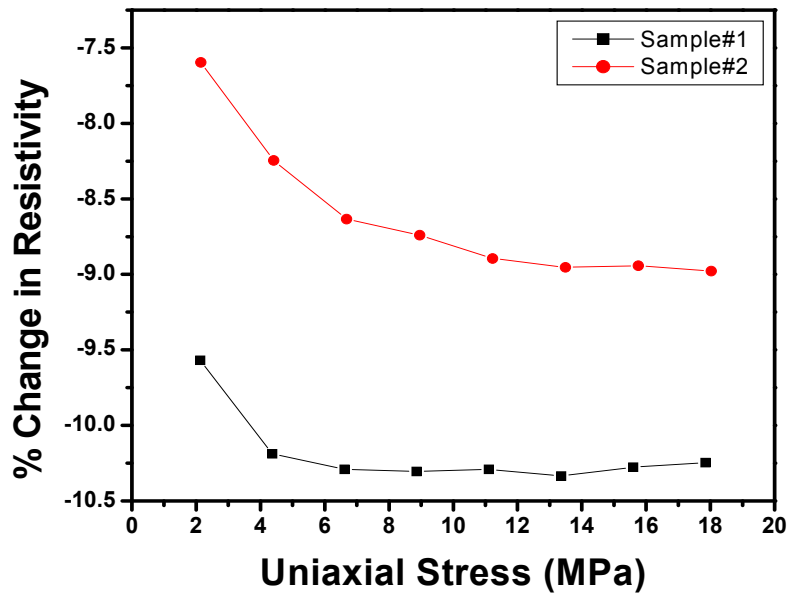


Figure 5.8 Piezoresistivity in  $\text{La}_{0.8}\text{Sr}_{0.2}\text{Nb}_{0.05}\text{Mn}_{0.95}\text{O}_3$  – partially stabilized  $\text{ZrO}_2$  composite.

But due to unreliability of the data and need for further investigation, the composite material was not selected as a force sensor material. The problems associated with the material, in spite of some success in terms of high compact strength, toughness, and observed changes in resistivity, are as summarized below and need to be resolved before any conclusion can be made.

- (1) The resistivity of the composite is too high in the range of  $10^{10}$   $\Omega\text{cm}$  and the material can't be practically used as a sensor.
- (2) The observed extremely large changes in the resistivity with stress needs to be further investigated and confirmed before any conclusion can be drawn.
- (3) The effect of the surface nanoporous layer and inter-diffusion of ions between the matrix and the dispersed phase needs to be investigated.
- (4) The reason for a negative change in resistance needs to be confirmed.

## CHAPTER 6

### MINIATURE FORCE SENSOR FOR AUTOMOBILE APPLICATIONS

#### 6.1 Material Selection

As mentioned in the previous section, the composite material originally intended to be used a tough and high strength material for force sensor, had some inherent problems. Since the dopant study on the piezoresistivity of LSMO showed that a giant enhancement in the piezoresistive properties was observed for the 5 mol% Nb doped LSMO composition, with a maximum change in resistivity of around 3% at 19.2 MPa, this material can be effectively used as a force sensing material. This material was selected to design and fabricate a practical prototype of the force sensor.

#### 6.2 Force Sensor design

The force sensor prototype was constructed using a new design with  $\text{La}_{0.8}\text{Sr}_{0.2}\text{Nb}_{0.05}\text{Mn}_{0.95}\text{O}_3$  as a sensing element. Since this material shows temperature dependence the resistance values at room temperature are not stable. The material showed a decrease in resistance with increasing temperature and after applying some pre stress load, the values were found to be near stable. To insulate this material, the sensing ceramic element was sandwiched between two layers of tetragonal 12 mol% ceria stabilized zirconia, which improved its mechanical strength and at the same time insulated the top and bottom of the sensing element. The schematic of the sensing element is as shown in the Fig. 6.1. Figure 6.2 shows the design model of the force

sensor construction. The working principle of the sensor is as follows. The sample as an active element is incorporated with a wheatstone bridge circuit. A schematic circuit diagram of the wheatstone bridge circuit is shown in Fig. 6.3. Two resistors of 2 k $\Omega$  were used as  $R_1$  and  $R_4$  and a potentiometer  $R_3$  of an equivalent resistance range as that of the sample  $R_2$  was selected and adjusted to the  $R_3$  value. For a balanced wheatstone bridge, the output voltage  $V_o = 0$  when the bridge is balanced, i.e.  $V_o = 0$ , if  $R_1 / R_4 = R_2 / R_3$ . For this reason,  $R_1$  was kept equal to  $R_4 = 2 \text{ k}\Omega$ ; and the  $R_2 = R_3 = 240 \Omega$ . An input supply voltage of 5 Vdc was supplied and the output voltage  $V_o$  measured as the resistance of the sample changed with applied force.

### 6.3 Force Sensor characterization

The output of the force sensor is as shown in the Fig. 6.6. A preload of 6 Newton was applied before taking any measurements. The preload was required so as to make the resistance of the sensing element to a near constant. A voltage offset in a balanced bridge configuration was around  $- 0.66 \text{ mVdc}$ . The force sensor was calibrated between the force ranges of 0 to 480 Newton. A maximum voltage output of about 4 mVdc at 480 N was observed.

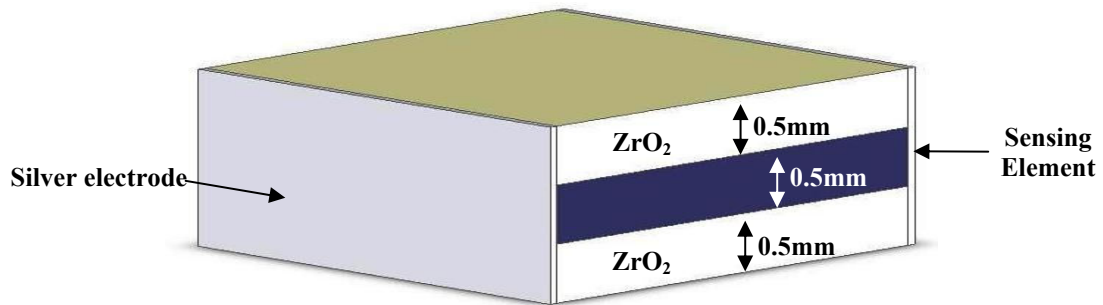


Figure 6.1 Schematics of the force sensing element.

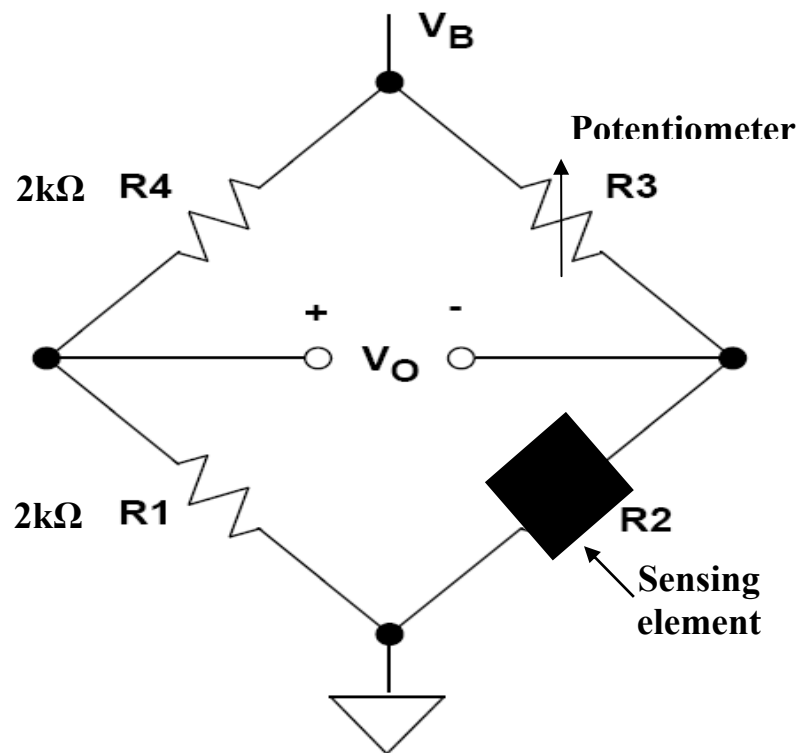


Figure 6.2 Wheatstone bridge arrangement used in the force sensor circuit.



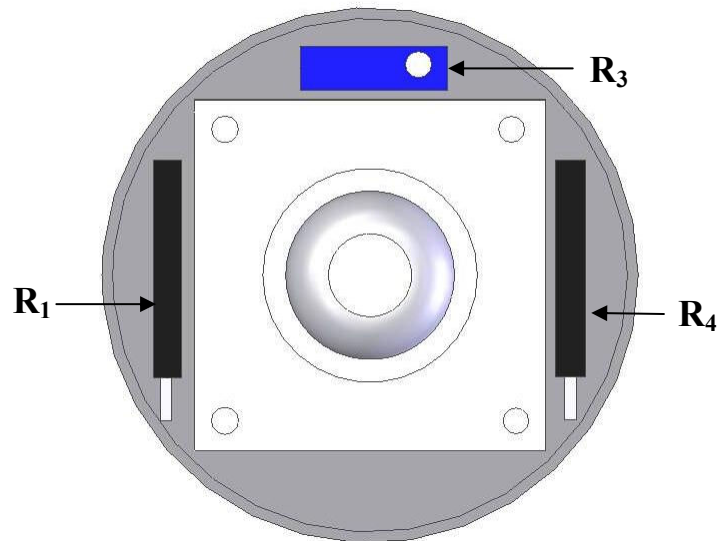


Figure 6.3 Force sensor design (top view)

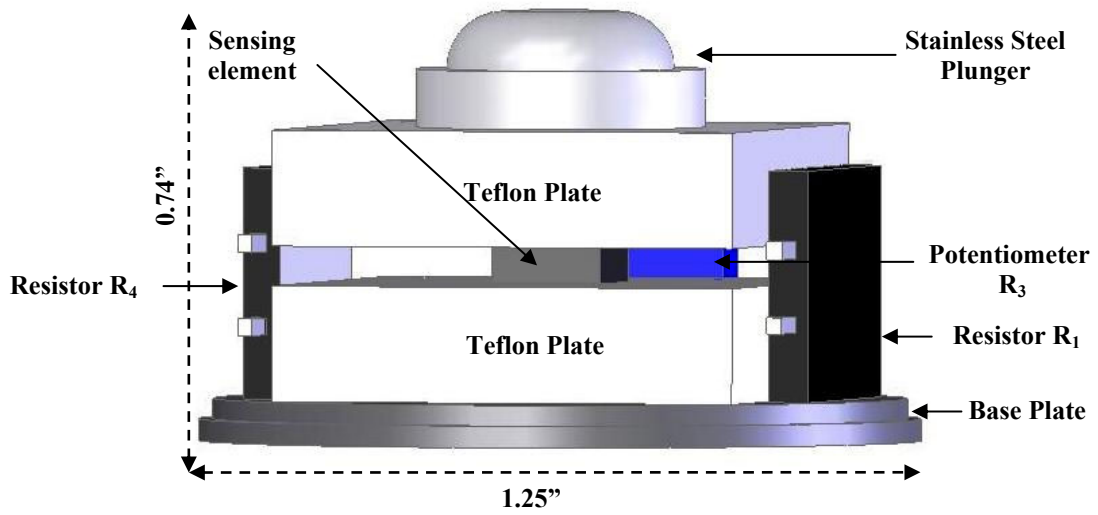


Figure 6.4 Schematic construction of the force sensor prototype (internal view).

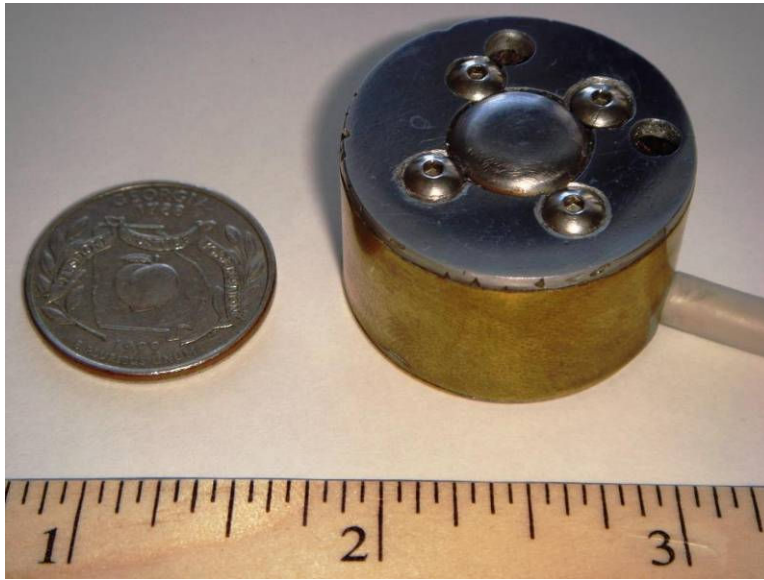


Figure 6.5 Picture of the miniature force sensor prototype.

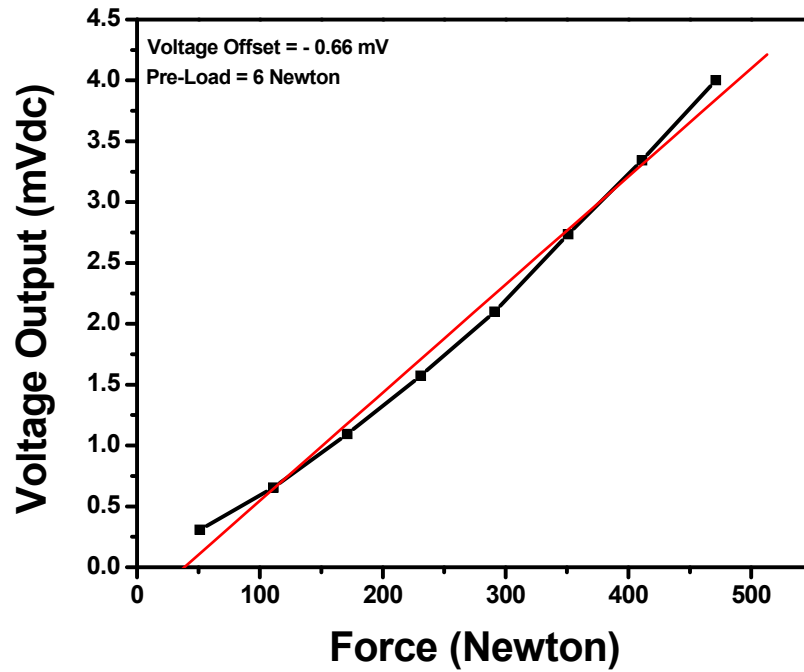


Figure 6.6 Voltage output characteristics of the miniature force sensor prototype.

## CHAPTER 7

### NANOPOROUS MATERIAL FOR OXYGEN GAS SENSOR

#### 7.1 Phase transformation as self assembly technique

Self assembly is a generic term for a system conforming itself in a minimum energy configuration. On a molecular level, the arrangement of individual molecules of a material, layer by layer is an extremely complicated process. But with a need for the development of nanostructures, these methods have been discovered and used to produce extremely complex nanostructures. The microbiology and nanotechnology combination has resulted in the development of new sophisticated techniques, including molecular self assembly of molecules, to form complex, functional structures<sup>[36, 37]</sup>. The electronic industry also sees a major scope in the use of self assembled nanostructures, including self assembled carbon nanotubes. Moreover, self assembled nanoporous structures are also equally important in the inorganic materials for a wide variety of applications<sup>[38, 39]</sup>.

In this research, a simple technique was found to produce a self assembled nanoporous surface network in conventional ceramic material. The technique involves the use of simple phase transformation in CeO<sub>2</sub> doped partially stabilized ZrO<sub>2</sub> ceramics. ZrO<sub>2</sub> has three polymorphic phases, monoclinic (T<1170°C), tetragonal (1170 < T < 2370°C) and cubic (T>2370°C). The monoclinic-tetragonal transformation is accompanied by a contraction in volume of ~5% which easily leads to mechanical

fracture in the ceramic. An addition of 12 mol% CeO<sub>2</sub> stabilizes the tetragonal phase at room temperature by creating oxygen vacancies [Ce<sup>3+</sup> (r<sub>8</sub> = 114 pm) on the Zr<sup>4+</sup> (r<sub>8</sub> = 84 pm) site] which leads to the decrease in the strain energy [40, 43]. However, investigations have revealed that in absence of the sintering aids the conventional ceramic processing technique did not retain the tetragonal phase at the room temperature [41]. Foschini et al [42] have shown that the unmodified sample of (Zr<sub>0.88</sub>Ce<sub>0.12</sub>)O<sub>2</sub> ceramics sintered at 1450°C retains only 18% of the tetragonal phase at the room temperature. On the other hand modification with very low amounts of Fe<sup>3+</sup> and Ni<sup>2+</sup> ions leads to retention of >90% tetragonal phase at room temperature [41]. The reason for this enhancement in the phase transformation has been associated to the increased diffusion pathway caused by oxygen vacancies. These results indicate that (Zr<sub>0.88</sub>Ce<sub>0.12</sub>)O<sub>2</sub> synthesized using conventional ceramic processing technique at temperatures of 1400°C undergoes tetragonal to monoclinic transformation.

The LSMO dispersed in the zirconia matrix, also stabilizes the ZrO<sub>2</sub> to retain a tetragonal structure, as evident from Fig. 5.6. The degree of this transformation is affected by the concentration of LSMO which aids in the formation of tetragonal phase. This result indicates that the surface nanoporous structure is formed from the competition between the tetragonal/monoclinic/cubic phases leading to the assembly of the heterogeneous components in minimum strain configuration.

## 7.2 Experimental procedure

The above mentioned gas sensor material was synthesized using the conventional ceramic processing route. The piezoresistive material La<sub>0.8</sub>Sr<sub>0.2</sub>MnO<sub>3</sub> was

dispersed in a ceria-doped partially stabilized zirconia matrix. For this purpose, the pre calcined powders of  $\text{La}_{0.8}\text{Sr}_{0.2}\text{MnO}_3$  and 12 mol% ceria doped zirconia powders were mixed in a polyethylene bottle and ball milled for 36 hrs to obtain a well-dispersed composite powders. The powder was then pressed into small round pellets of 0.5 inch diameter in hardened steel die and then in CIP at a pressure of 40 ksi. The green body was sintered at  $1400^\circ\text{C}$  for 6 hrs. The sintered composite material was found to have a self assembled nanoporous network on the surface and has been discussed in the following section.

### 7.3 Self-assembled nanoporous surface network

A self-assembly of nanometer sized pores was observed in the  $\text{La}_{0.8}\text{Sr}_{0.2}\text{MnO}_3$  –  $\text{CeO}_2$  stabilized  $\text{ZrO}_2$  composite. Figure 7.1 shows the SEM images of the self assembled nanoporous surface layer structure. The grains of the dispersed phase, which is  $\text{La}_{0.8}\text{Sr}_{0.2}\text{MnO}_3$ , were found to exist at the grain boundaries and the grain boundary junctions. The matrix phase which is partially stabilized  $\text{ZrO}_2$  was found to possess a porous layer with a periodic, self assembly of nanometer sizes pores. The nanoporous layer was examined using a Ga-ion, Focused Ion Beam (FIB) combined with SEM, to find the depth of the porous layer and to determine the periodicity in pore distribution and the size of the pores. The pores were found to have diameter in the range of 150 – 200 nm, while the thickness of the porous layer was around 100 nm. The pore distribution was quite periodic with average spacing in the range 50 – 150 nm.

The bulk of the material was found to be pore free. TEM analysis on the surface layer indicates the existence of this layer on the surface only, while it was found that the

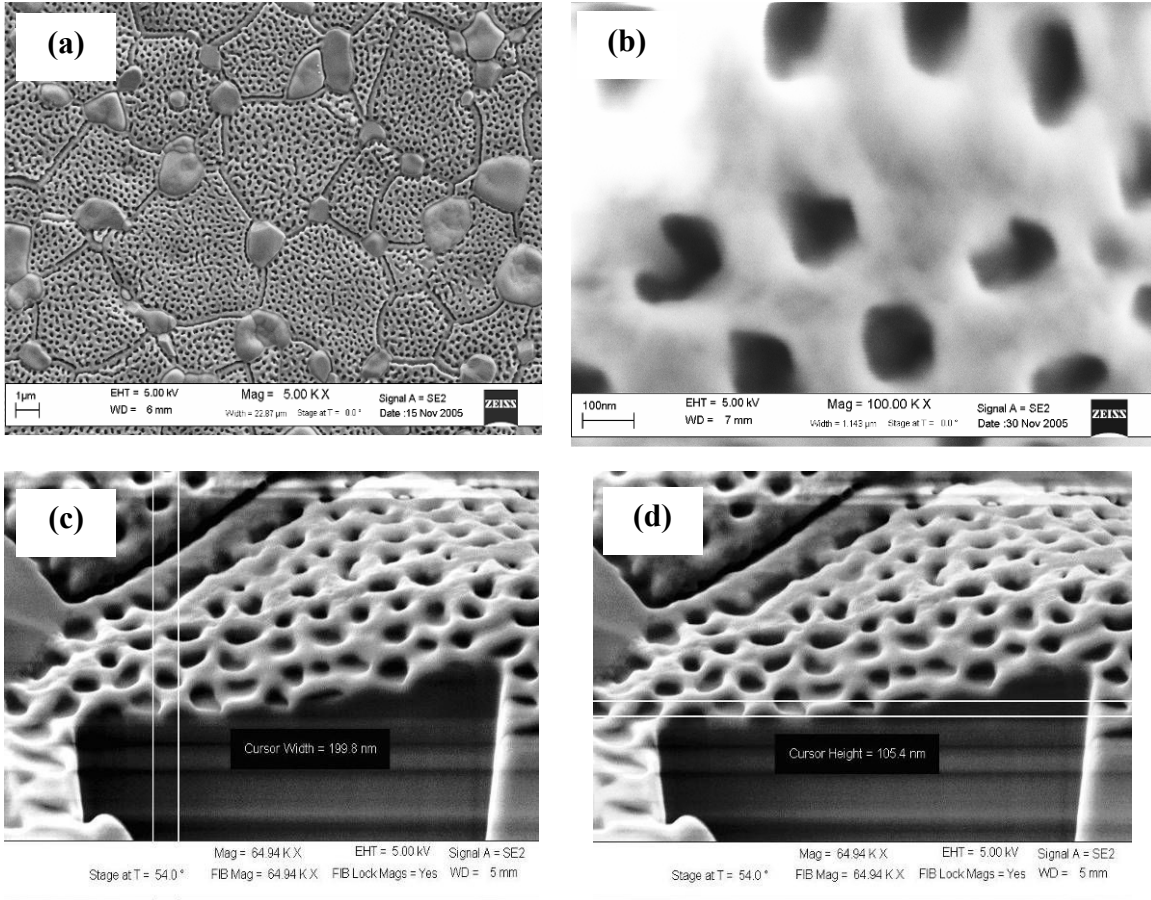


Figure 7.1 Self assembled nanoporous network in the  $\text{La}_{0.8}\text{Sr}_{0.2}\text{MnO}_3$  – partially stabilized  $\text{ZrO}_2$  composite. (a) at 5 kX (b) pore morphology at 100 kX. (c) diameter of the pores (d) thickness of the porous layer.

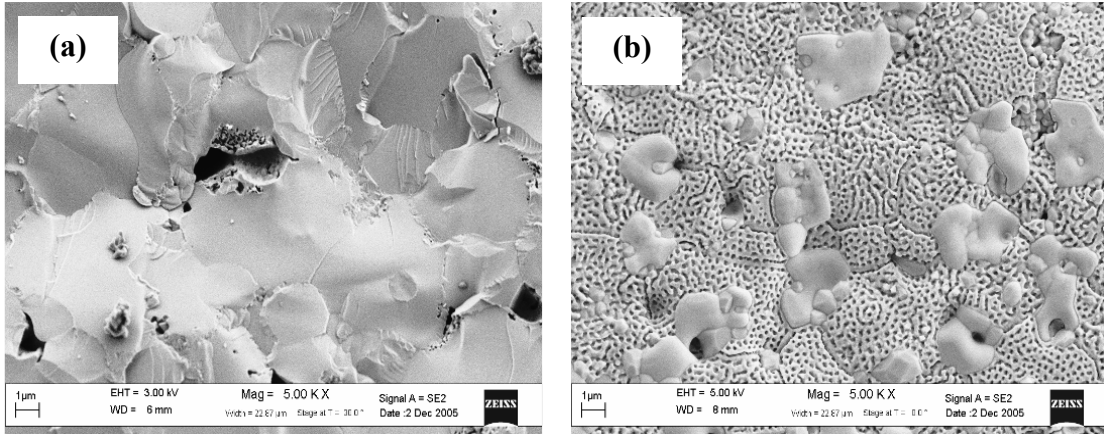


Figure 7.2 (a) Fractured cross section and (b) cross section after polishing and etching.

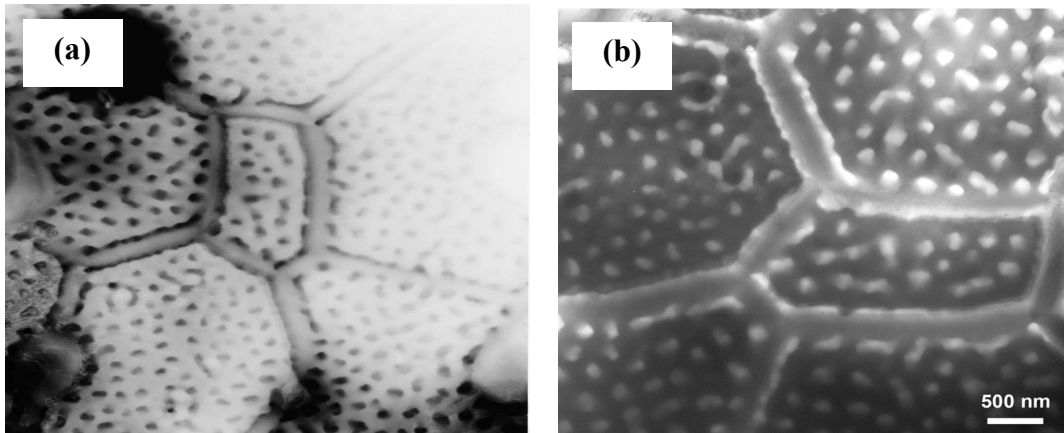


Figure 7.3 TEM images of the surface nanoporous layer in LSMO-ZrO<sub>2</sub> composite, (a) and (b).

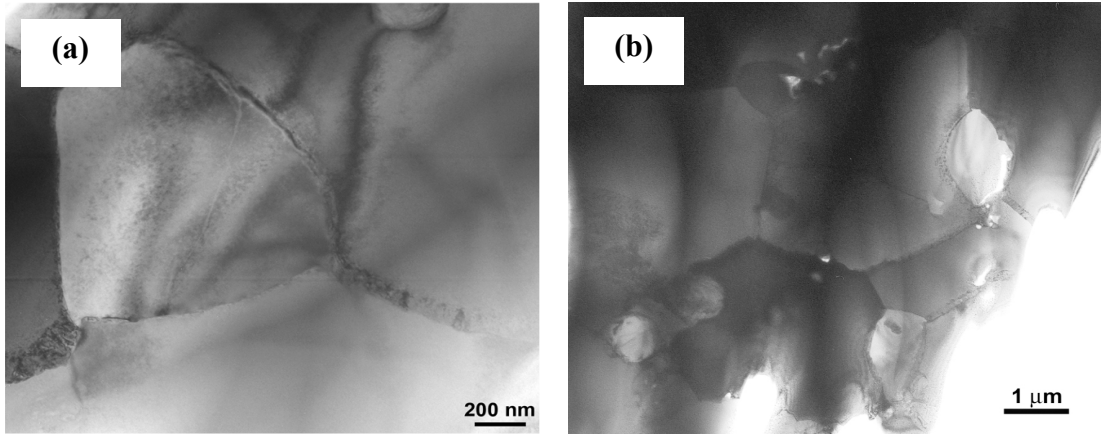


Figure 7.4 TEM images of the bulk of the LSMO- ZrO<sub>2</sub> composite.

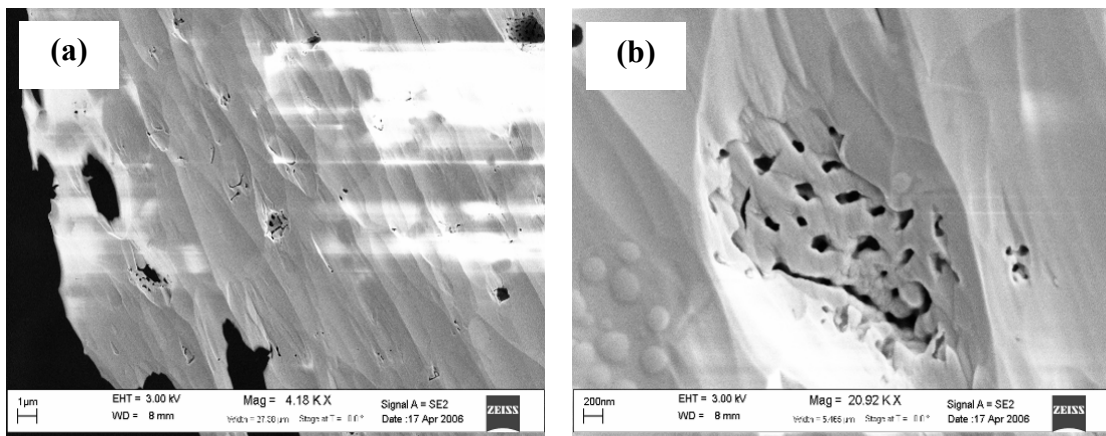


Figure 7.5 SEM micrograph of a TEM sample prepared after polishing (a) and (b).



bulk was pore free. Figures 7.3 (a) and 7.3(b) show the bulk grain structure and the surface nanoporous layer of the composite respectively. It is to be noted that the TEM sample prepared by polishing off the surface layer, did not reveal a porous structure and this is confirmed by SEM on the TEM sample prepared after polishing. The Figures 7.4 (a) and 7.4(b) confirm that the nanoporous layer exists on the surface.

The existence of the self assembled structure was checked under different sintering conditions. The effect of sintering temperature on the formation of the porous structure was studied, and it was found that the pore structure improved significantly with an increasing temperature. The effect of sintering temperature ranging from 1300°C to 1450°C with a sintering time of 6 hrs, on the pore structure is as shown in Fig. 7.5

#### 7.4 Crystal structure and phase determination

The crystal structure and the phase analysis on the nanoporous composite material were done using x-ray diffraction and selected area electron diffraction (SAED), using a TEM. The x-ray diffraction revealed interesting results for the nanoporous composite. It was found that the XRD pattern of a polished, surface nanoporous layer-free composite was quite different than the material with a nanoporous layer on the surface.

The composite material was found to contain a ZrO<sub>2</sub> rich phase, and the peaks corresponded to a tetragonal ZrO<sub>2</sub> phase. As shown in the Fig. 7.6, the major peaks correspond to ceria stabilized ZrO<sub>2</sub> marked with an asterisk, and the rest of the peaks

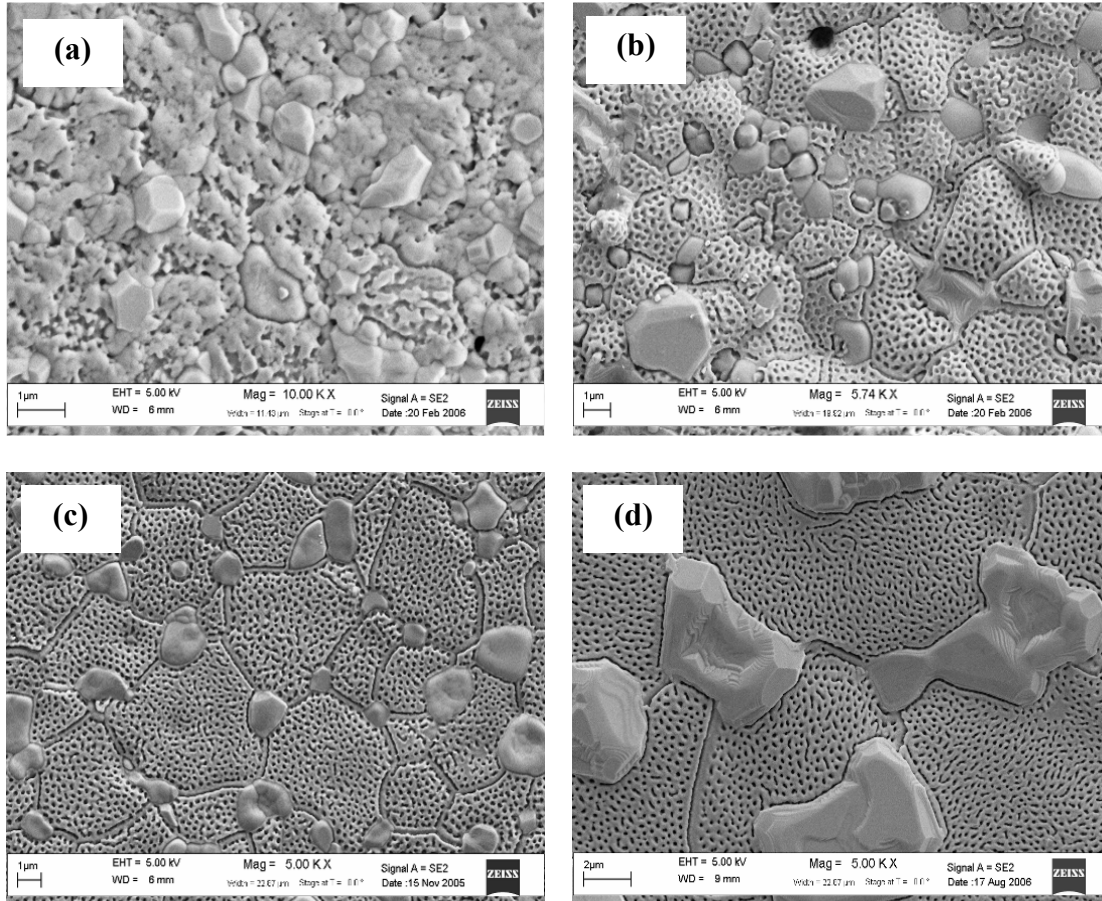


Figure 7.6 Nanoporous composite after varying the sintering temperature (a) 1300°C, (b) 1350°C, (c) 1400°C, and (d) 1450°C for 6 hrs respectively.

corresponded to a LSMO rich phase, with considerable peak shifts as compared to pure LSMO, due to inter-diffusion of Zr and Ce ions. The SAED patterns for the grain boundary island grains and the porous region are shown in Fig. 7.7

Elemental analysis was done for studying the composition of the phases present in the composite material. The elemental analysis done using the EDAX combined with SEM, showed appreciable results and the results are shown in Fig. 7.8. The elemental mapping done on the island grains at grain boundary and the porous region reveal that the nanoporous network is composed of a ZrO<sub>2</sub> rich phase and the island grains are a LSMO rich phase.

In order to get even more accurate results, an EDX using TEM was done and it indicated similar results. The EDX patterns of the island grains and the porous network region are as shown in Figs. 7.9 and 7.10 respectively. The Curie temperature of the composite material was found to be high, near 330 K. Figures 7.11(a) and (b) depict the temperature dependence of magnetic moment and the room temperature magnetic hysteresis loops for the samples with and without the porous layer. No appreciable change in the magnetic behavior was found.

## 7.5 Composition modifications

### *7.5.1. LSMO variation*

The effect of compositional change on the surface nanopore formation and the morphology of the pores were studied. For this reason, the amount of LSMO in the composite was varied and the microstructural aspects were studied. The LSMO content was varied ranging from 5.38 mol% LSMO to 35.8 mol% LSMO.

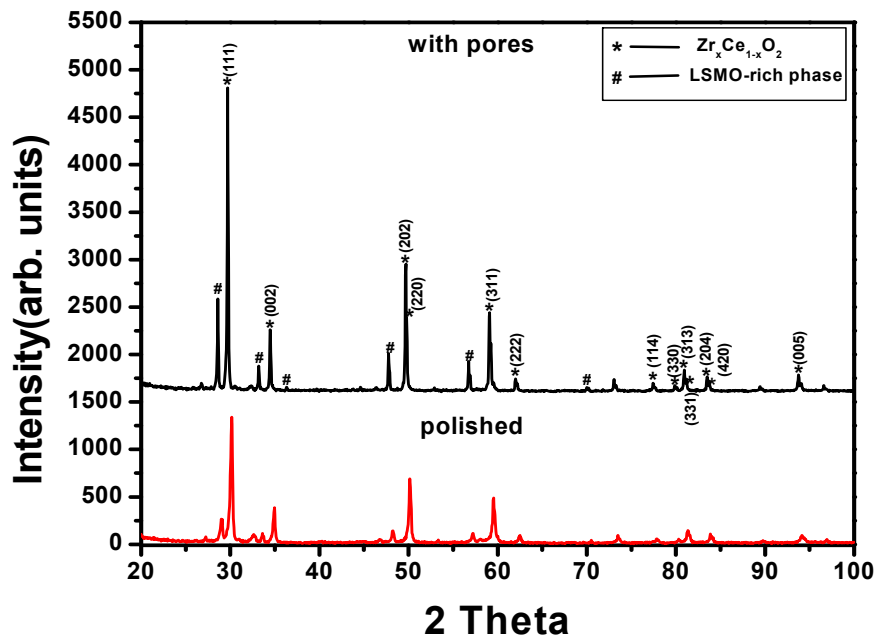


Figure 7.7 X-ray diffraction results for samples with porous layer and after polishing off the layer.

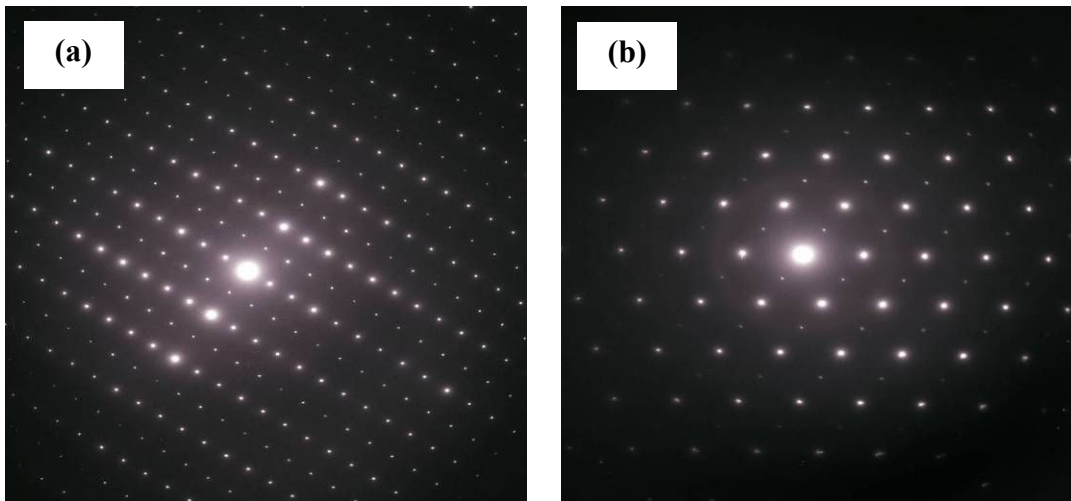


Figure 7.8 SAED patterns of (a) the grain boundary islands and (b) porous network regions.

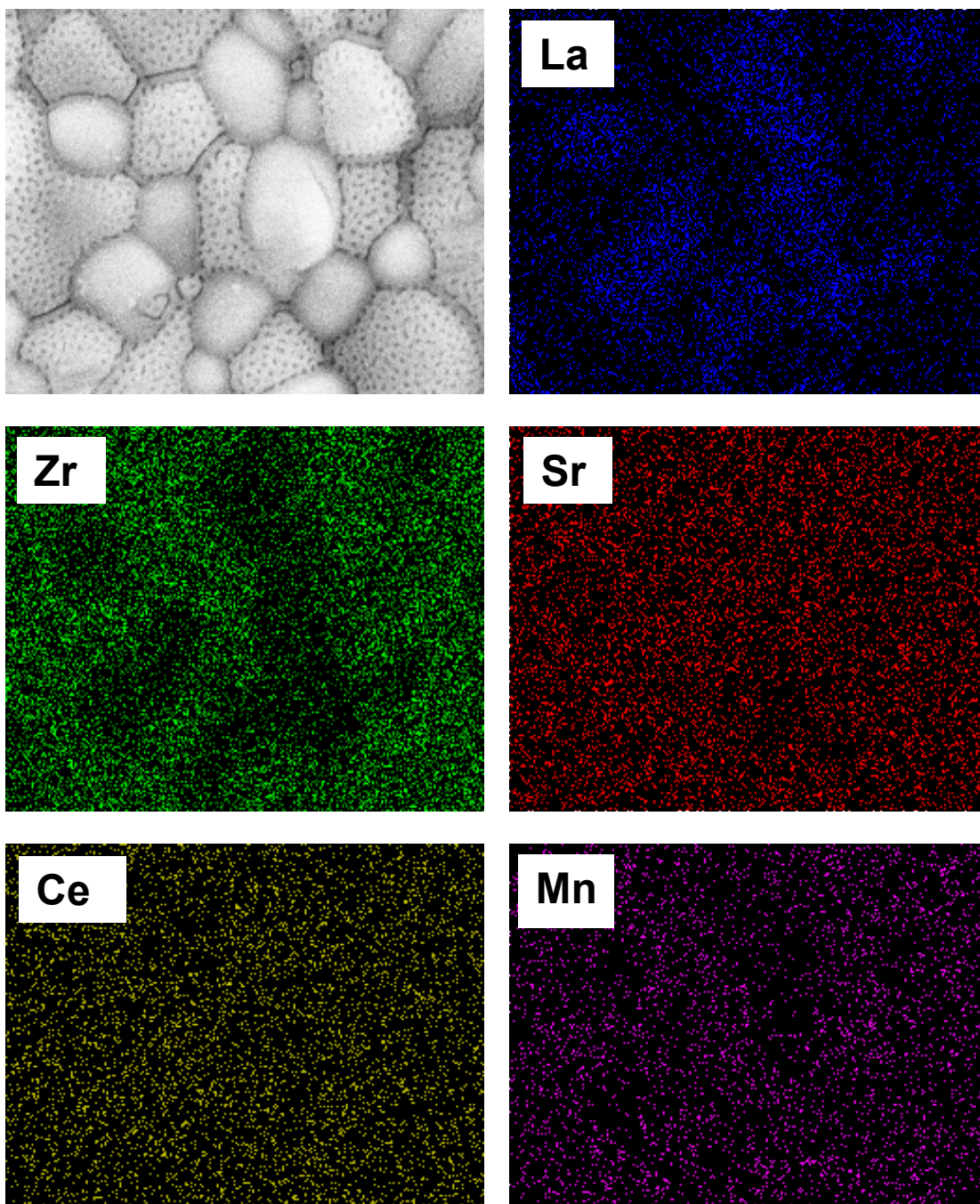


Figure 7.9 Elemental maps for 25 wt% LSMO-ceria stabilized ZrO<sub>2</sub>.

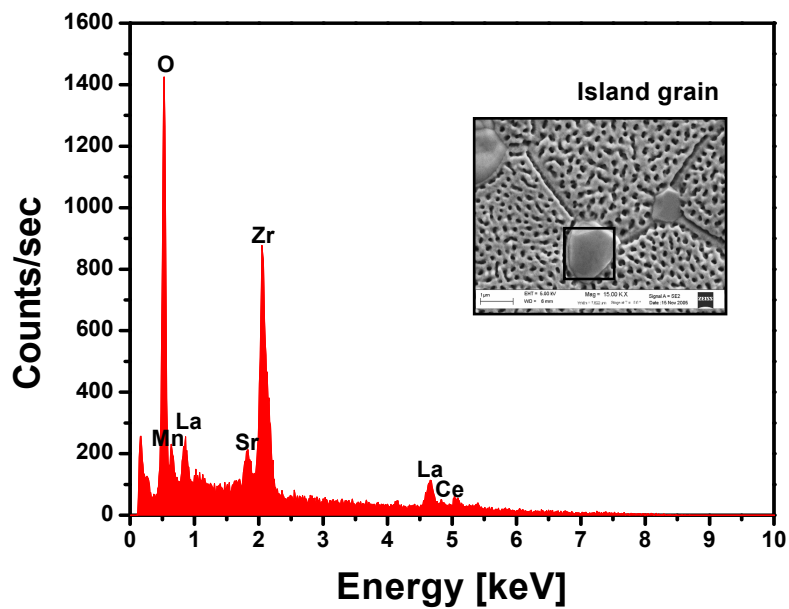


Figure 7.10 SEM EDAX pattern for the island grain in LSMO-ZrO<sub>2</sub> nanoporous composite.

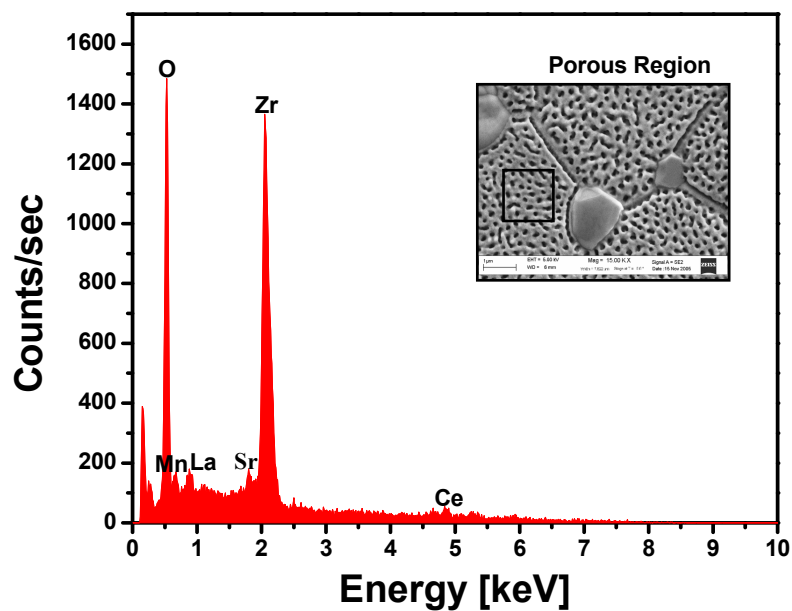


Figure 7.11 SEM EDAX pattern for the porous region of LSMO-ZrO<sub>2</sub> nanoporous composite.

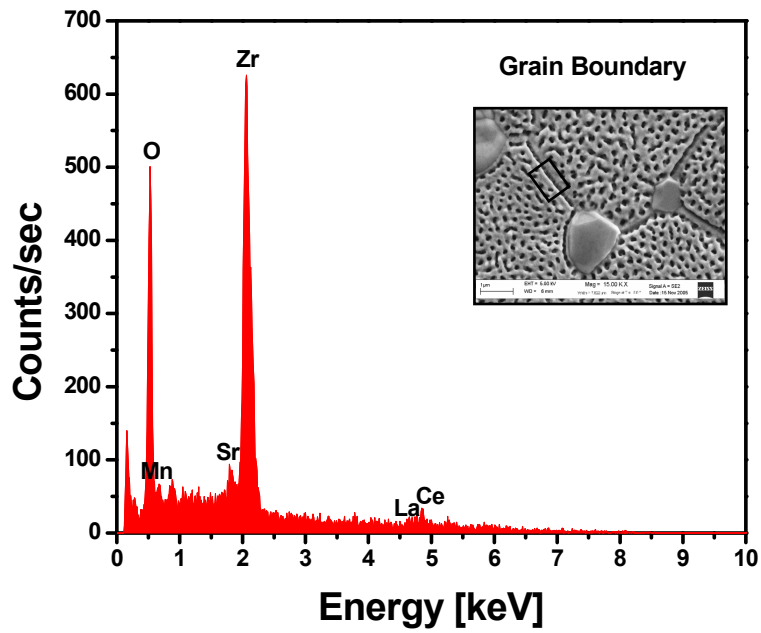


Figure 7.12 SEM EDAX pattern for the grain boundary in the LSMO-ZrO<sub>2</sub> nanoporous composite.

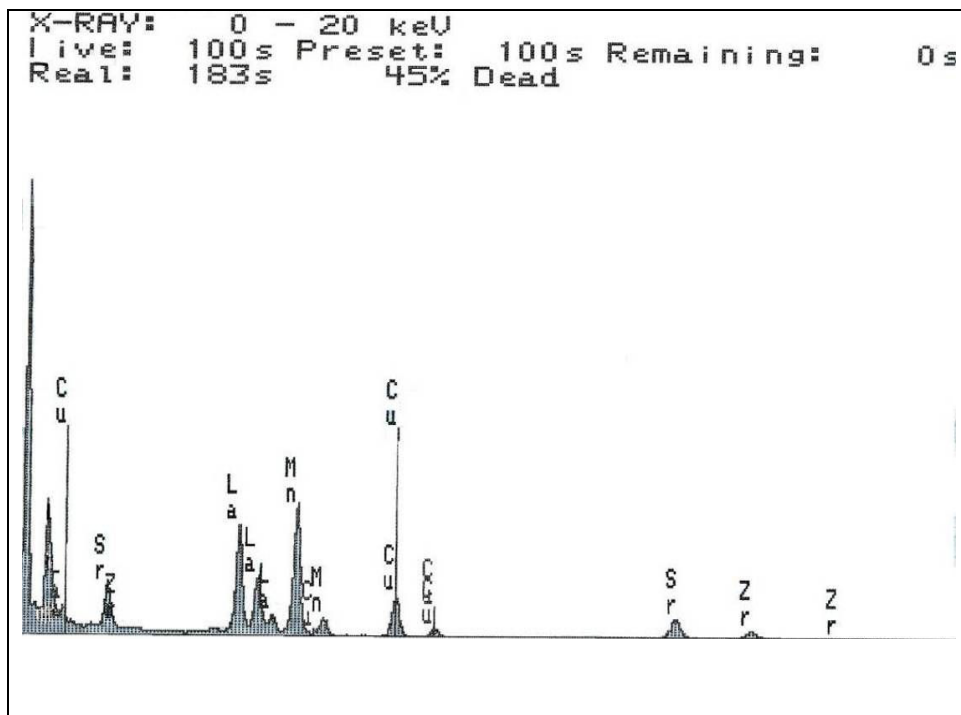


Figure 7.13 TEM - EDX analysis on the island grains.





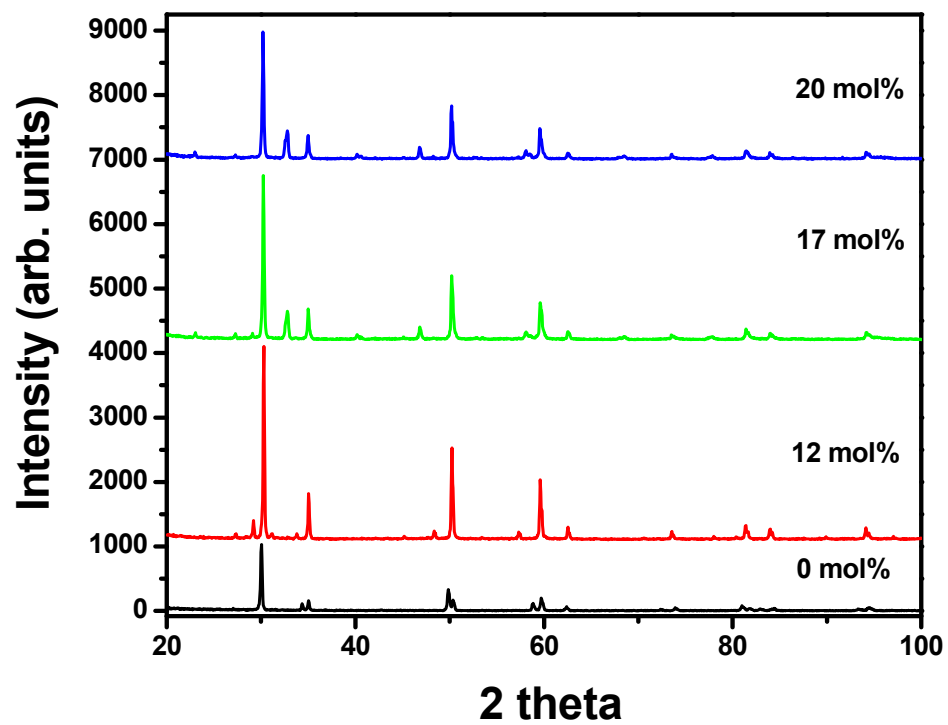


Figure 7.16 XRD patterns of  $\text{La}_{0.8}\text{Sr}_{0.2}\text{MnO}_3 - (\text{Ce}_{0.12}\text{Zr}_{0.88})\text{O}_2$  composite with varying LSMO content.

A result of significant information was found. At 5.38 mol% LSMO, there were no surface pores in the material.

### *7.5.2 Ceria variation*

In order to study the effect of second type of compositional variation, the amount of stabilizing CeO<sub>2</sub> was varied. Originally, 12 mol% CeO<sub>2</sub> has been used to stabilize ZrO<sub>2</sub> powders to obtain partially stabilized ZrO<sub>2</sub>. The effect of varying the CeO<sub>2</sub> amount to 10 mol% and 14 mol% was studied. The Fig. 7.25 and Fig. 7.26 show that the CeO<sub>2</sub> content had an effect on the thickness of the grain boundaries of the nanoporous surface layer composite. The grain boundaries become more distinct and thicker as the ceria content was increased. For a 10 mol% CeO<sub>2</sub> content, an approximate thickness of 0.3 μm was observed and at 14 mol% CeO<sub>2</sub> the grain boundaries were quite thick (0.5 μm) on an average.

## 7.6 Oxygen gas sensor

### *7.6.1 Gas sensor design*

The nanoporous composite material with a composition of (LSMO)<sub>0.15</sub> – (Ce<sub>0.12</sub>Zr<sub>0.88</sub>O<sub>2</sub>)<sub>0.85</sub> or 15 mol% LSMO- CeO<sub>2</sub> doped zirconia composite as mentioned earlier was tested for oxygen gas sensing. For this purpose, a simple design of the oxygen gas sensor was made<sup>[47]</sup>, the schematics of which are shown in the Fig. 7.29. It consists of a ceramic enclosure with a small hole of diameter 0.02 inch at the top for purging oxygen gas.

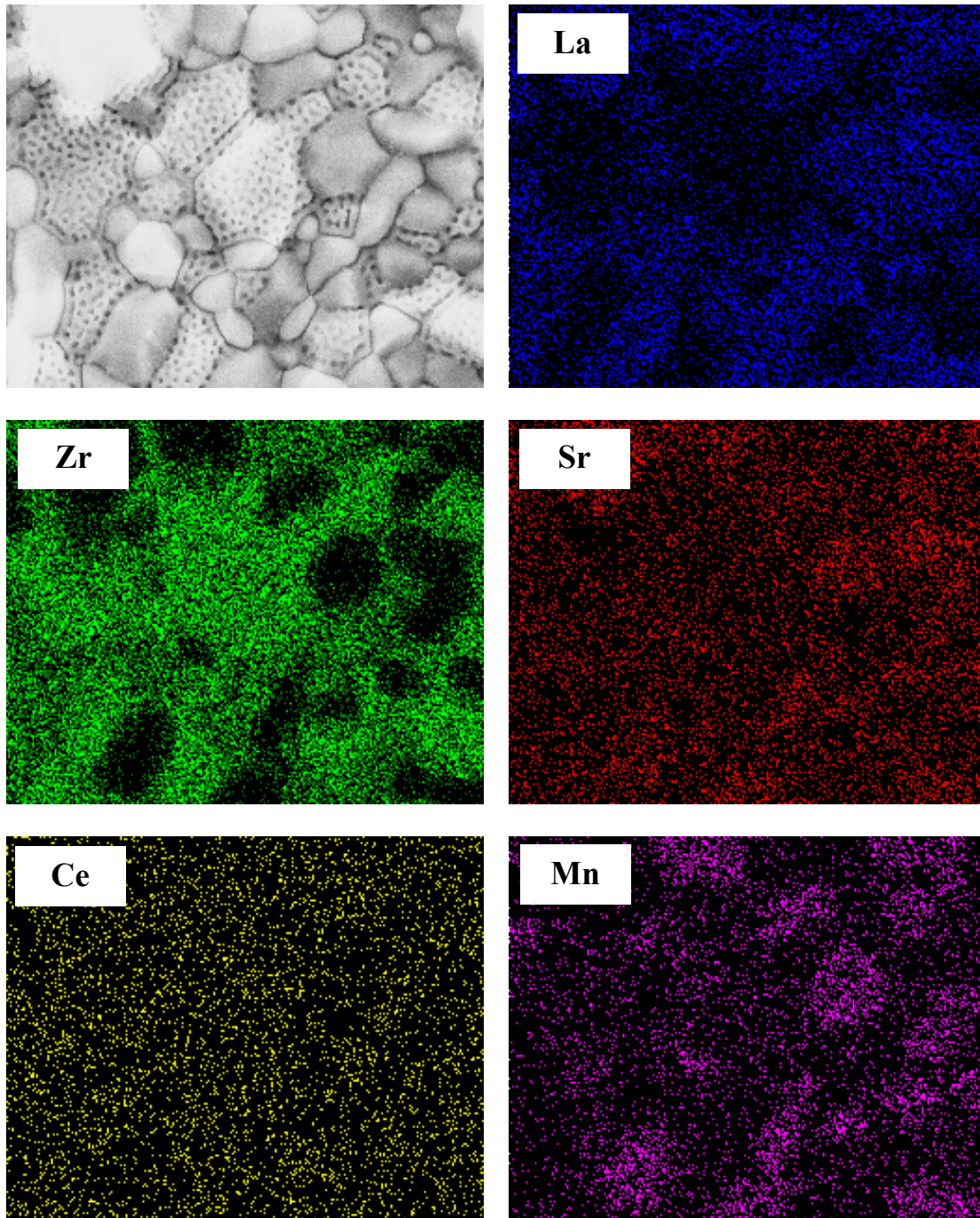


Figure 7.17 Elemental maps for 35.8 mol%LSMO – (Ce<sub>0.12</sub>Zr<sub>0.88</sub>)O<sub>2</sub> composite.

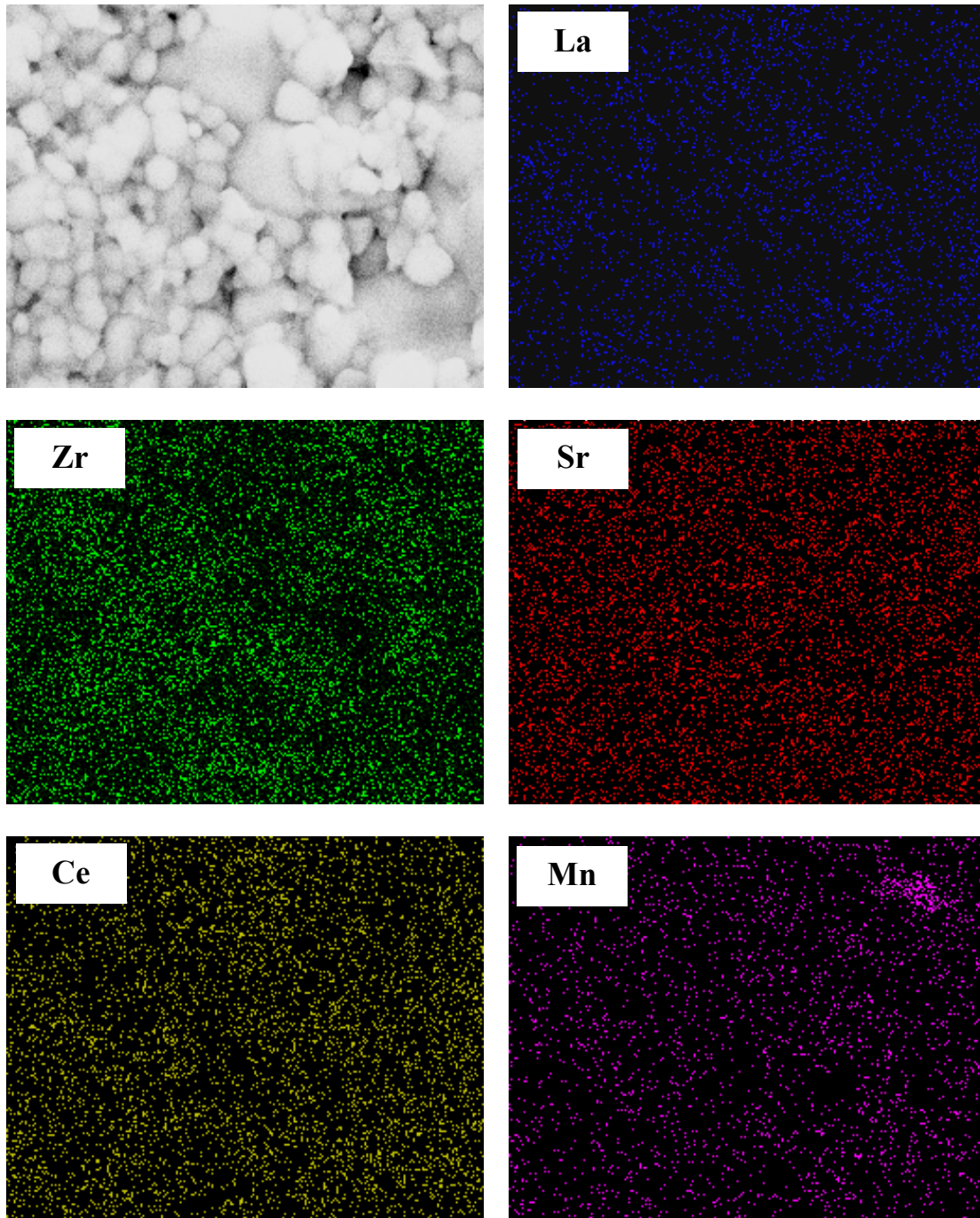


Figure 7.18 Elemental maps for 5.83 mol% LSMO –  $(\text{Ce}_{0.12}\text{Zr}_{0.88})\text{O}_2$  composite.

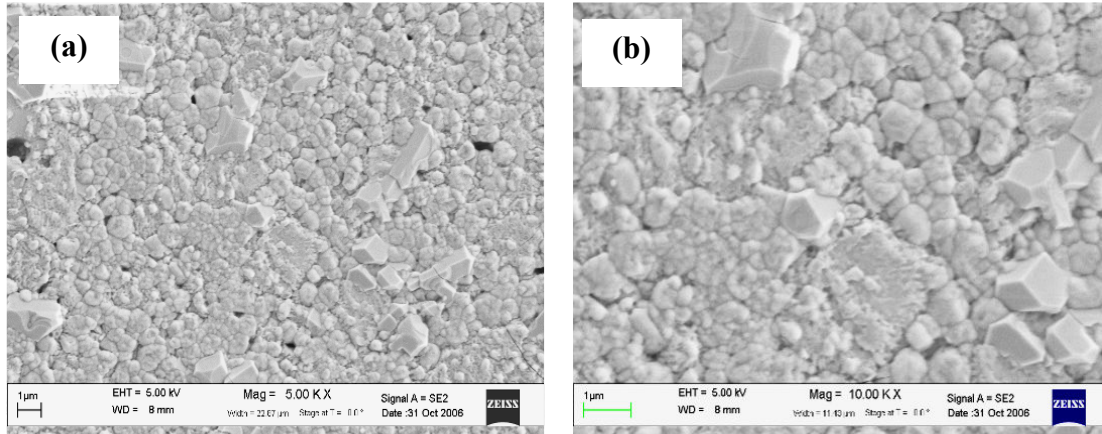


Figure 7.19 SEM micrograph of the 5.83 mol% LSMO – (Ce<sub>0.12</sub>Zr<sub>0.88</sub>)O<sub>2</sub> composite sintered at 1400°C for 6 hrs, (a) at 5 kX and (b) at 10 kX.

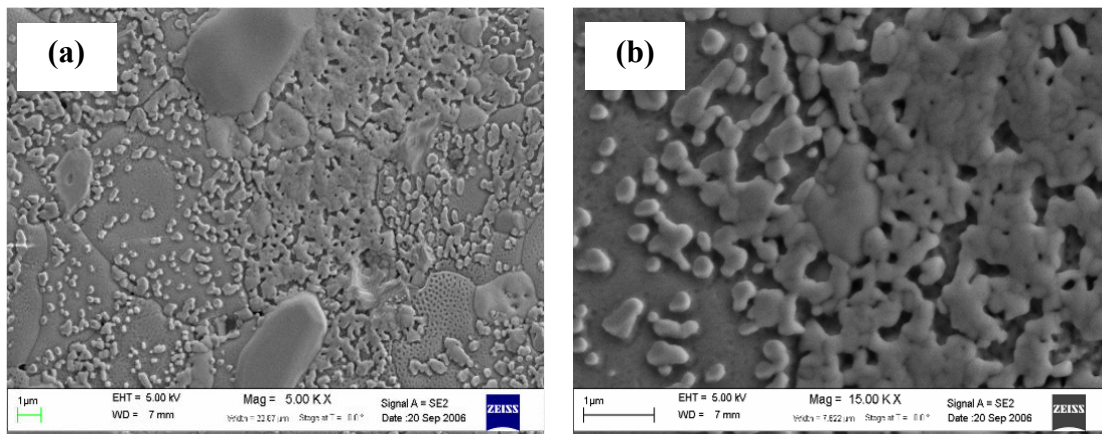


Figure 7.20 SEM micrograph of the 12 mol% LSMO – (Ce<sub>0.12</sub>Zr<sub>0.88</sub>)O<sub>2</sub> composite sintered at 1400°C for 6 hrs, (a) at 5 kX and (b) at 15 kX.



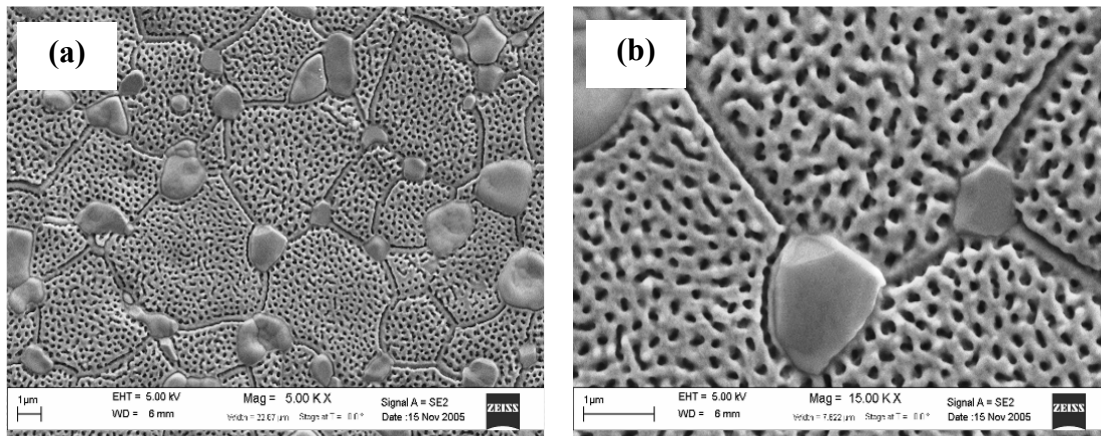


Figure 7.21 SEM micrograph of the 15.66 mol% LSMO –  $(\text{Ce}_{0.12}\text{Zr}_{0.88})\text{O}_2$  composite sintered at 1400°C for 6 hrs, (a) at 5 kX and (b) 15 kX.

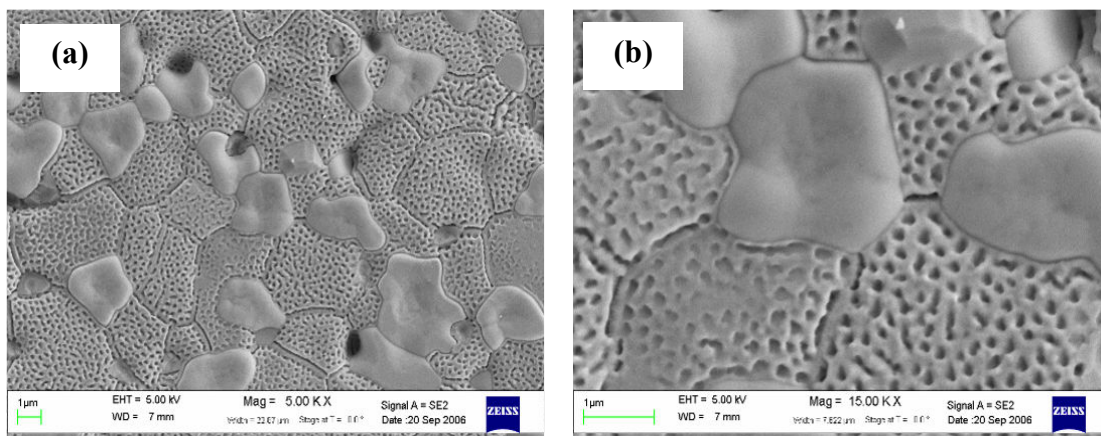


Figure 7.22 SEM micrograph of the 17 mol% LSMO –  $(\text{Ce}_{0.12}\text{Zr}_{0.88})\text{O}_2$  composite sintered at 1400°C for 6 hrs, (a) at 5 kX and (b) 15 kX.

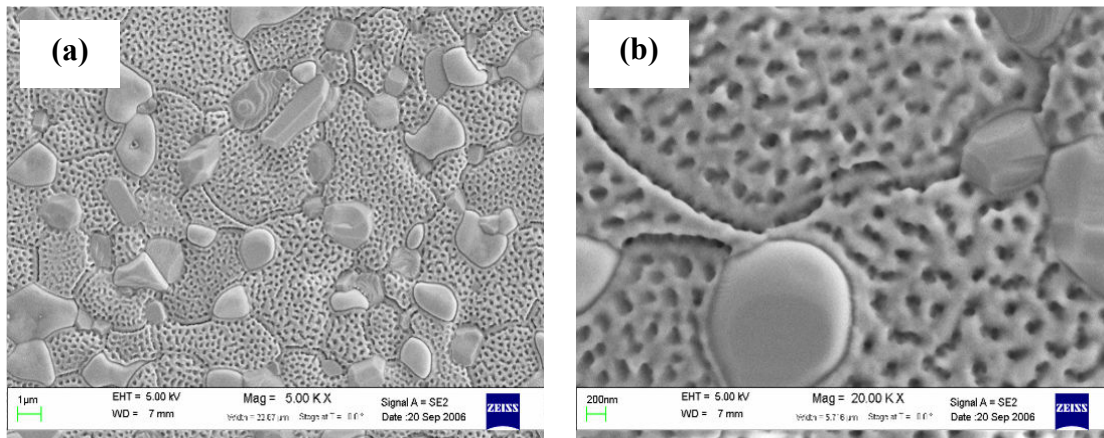


Figure 7.23 SEM micrograph of the 20 mol% LSMO – (Ce<sub>0.12</sub>Zr<sub>0.88</sub>)O<sub>2</sub> composite sintered at 1400°C for 6 hrs, (a) 5 kX and (b) at 20 kX.

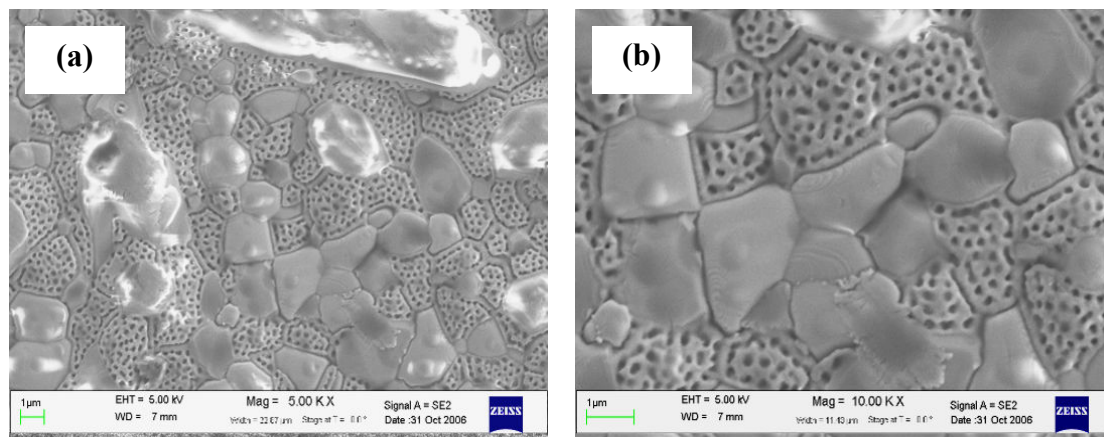


Figure 7.24 SEM micrograph of the 35.8 mol% LSMO – (Ce<sub>0.12</sub>Zr<sub>0.88</sub>)O<sub>2</sub> composite sintered at 1400°C for 6 hrs, (a) at 5 kX and (b) at 10 kX

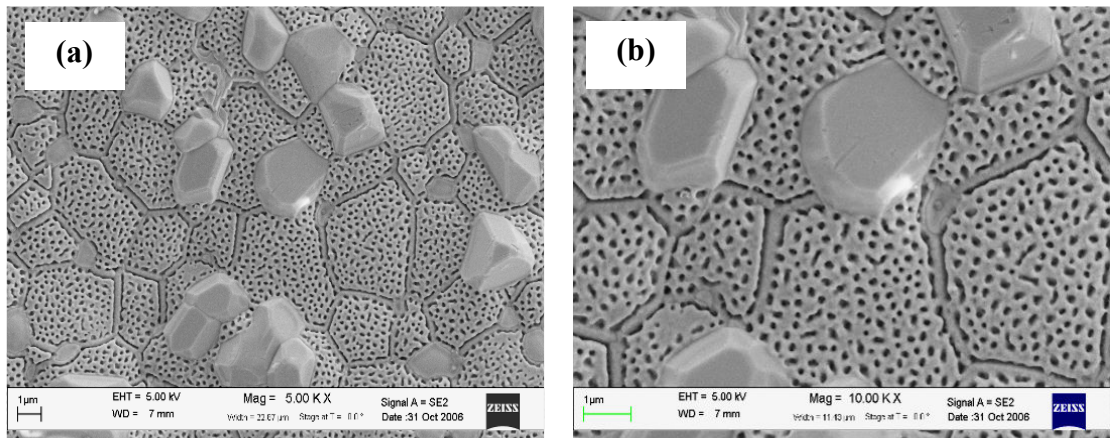


Figure 7.25 SEM micrograph of the LSMO – 10mol% CeO<sub>2</sub> stabilized ZrO<sub>2</sub> composite, (a) at 5 kX and (b) at 10 kX.

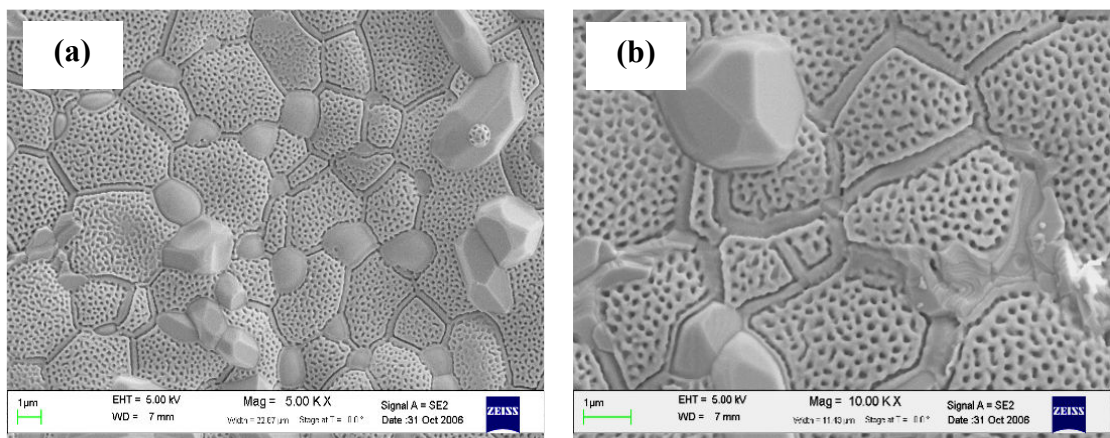


Figure 7.26 SEM micrograph of the LSMO – 14 mol% CeO<sub>2</sub> stabilized ZrO<sub>2</sub> composite, (a) at 5 kX and (b) at 10 kX.



A bottom hole exposes the sample which is in the form of a disc of diameter 0.5 inch, to a reference gas, which is air in this case. The top surface of the sample and the bottom surface of the sample are perfectly isolated from each other. Two electrode connections using a ring pattern of metal disc are made for top and bottom. It is to be mentioned here that the top and bottom surface of the ceramic sample painted with a thin layer of silver electrodes, fired at 850°C. The two electrode connections are then connected to a digital multimeter for voltage output signal.

#### *7.6.2 Gas sensor working principle*

Conventional  $ZrO_2$  gas sensors are based on the principle of ionic conduction that takes place in  $ZrO_2$  at temperatures ranging from 500°C and above [44 - 51]. In this research the sample is composed of a  $ZrO_2$  matrix, with a dispersed  $La_{0.8}Sr_{0.2}MnO_3$  phase which is a metallic conductor. As mentioned in the previous section this composite material has a periodic self-assembled surface nanoporous layer. This significantly increases the exposed surface area of the sample under test. Since the system of  $La_{0.8}Sr_{0.2}MnO_3$  and  $CeO_2$  doped  $ZrO_2$  is an oxygen deficient system, the composite is expected to show oxygen ion conductivity. As mentioned in Sec. 7.6.1, the top surface of the sample is exposed to varying concentration of oxygen while the bottom surface is exposed to a reference gas, which is air, in this case. As a result of a difference in oxygen partial pressure, a potential difference exists between the top and bottom surface. At a suitable temperature, the  $ZrO_2$  matrix, conducts oxygen ions, and an output emf can be observed which is related to the oxygen partial pressure difference by the following Nernst equation.

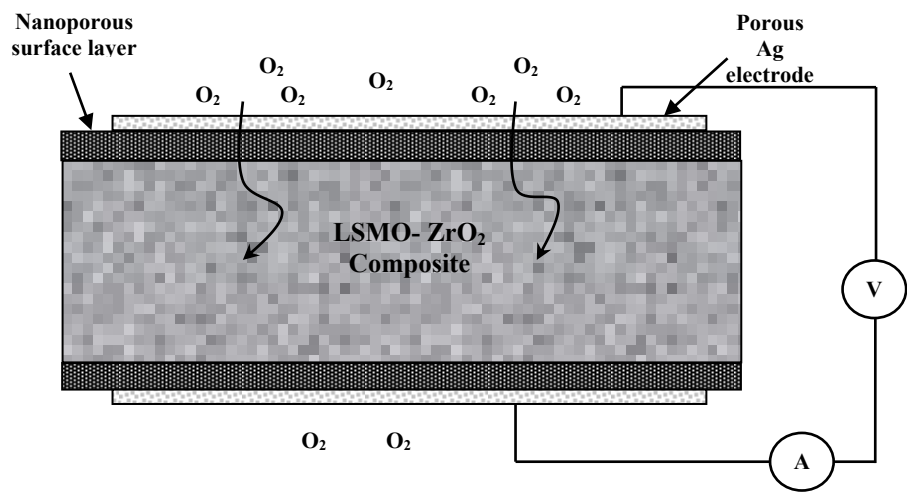


Figure 7.27 Mechanism of oxygen ion conduction in the LSMO-partially stabilized ZrO<sub>2</sub> composite with a nanoporous surface layer.

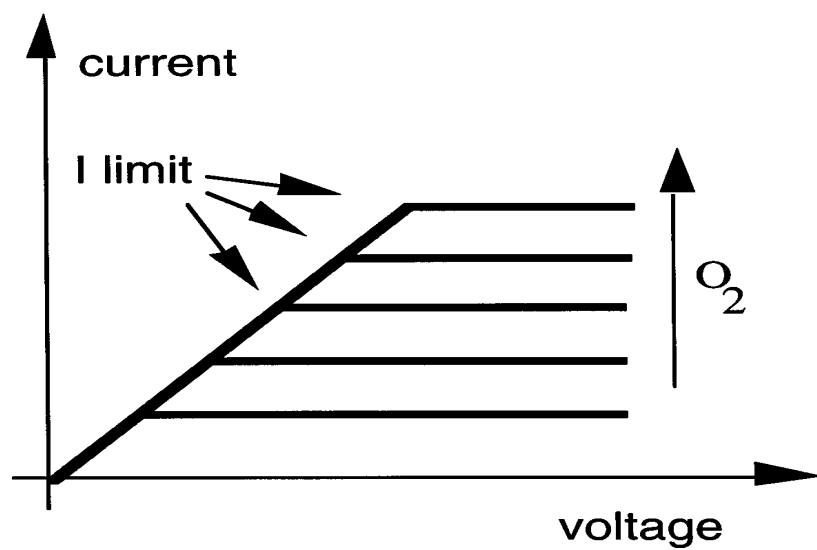


Figure 7.28 Voltage-current characteristics of a limiting-current type oxygen sensor<sup>[47]</sup>.

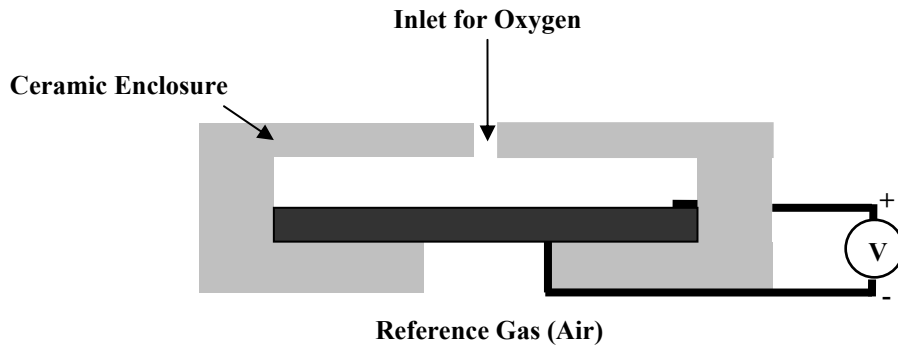


Figure 7.29 Schematics of the oxygen gas sensor tested in this research work.

Table 6 Response of the nanoporous surface layer composite oxygen sensor.

<b>Temperature (°C)</b>	<b>Oxygen Concentration</b>			<b>Output Voltage(mVdc)</b>
100	10%	50%	90%	0.00
200	10%	50%	90%	0.00
300	10%	50%	50%	0.00

$$U = (RT/4F) \ln(p_{\text{ref}} / p(\text{O}_2))$$

where U is the generated emf, R= Universal gas constant, F= Faradays constant,  $p_{\text{ref}}$  is the partial pressure of the reference gas, and  $p(\text{O}_2)$  is the partial pressure of  $\text{O}_2$  gas. A schematic of the oxygen conduction mechanism in the composite is shown in Fig. 7.27.

### *7.6.3 Gas sensor data*

Voltage-current characteristics of a typical oxygen sensor is shown in Fig. 7.28<sup>[47]</sup>. The oxygen gas sensor described above using the nanoporous surface layered composite was tested for oxygen gas conduction at temperatures ranging from 100°C to 300°C. No output voltage signal was observed, in these temperature ranges. The results are summarized in the table 6.

### *7.6.4 Discussion*

The above mentioned results indicate that a high temperature is required to bring the sensing element within the working range. This can be estimated from the fact of conventional  $\text{ZrO}_2$  oxygen sensors utilized in automobiles operates at a temperature range of 500-800°C. Due to the unavailability of necessary supplies, the high temperature measurements were not conducted. This material is expected to show a good response to oxygen ion conduction, owing to the fact of a large surface area and oxygen deficient system. So, further investigations are required to be done in order to explore this material for oxygen gas sensing for automobile applications.

## CHAPTER 8

### CONCLUSION

The objectives of the present research work were accomplished and are as summarized below:

1. The piezoresistivity in the bulk polycrystalline  $\text{La}_{0.8}\text{Sr}_{0.2}\text{MnO}_3$  was successfully studied for the effect of composition, doping elements, their concentration, uniaxial pressure, and synthesizing conditions on the microstructural, magnetic, electrical, and piezoresistive properties of these materials.
2. A mechanically tough composite material with excellent piezoresistive properties was synthesized for force sensing applications and the effects of compositional variation and synthesis conditions on the microstructural and piezoresistive properties were successfully studied.
3. A miniature force sensor prototype was designed, fabricated and characterized.
4. A nano-porous composite material with a self-assembled nanoporous surface network was synthesized for oxygen gas sensing.

## CHAPTER 9

### FUTURE WORK

#### 9.1 (Ba,Sr)TiO<sub>3</sub>– CoFe<sub>2</sub>O<sub>4</sub> composite for force sensor

A new idea for a piezoresistive material with high piezoresistive coefficient has been presented. The positive temperature coefficient of resistance (PTCR) Barium strontium titanate has been found to possess an extremely large piezoresistive coefficient near  $2500 \times 10^{-12} \text{ MPa}^{-1}$  [15, 57, 58]. Such a large coefficient can be utilized for piezoresistive force sensors. Improvements in the temperature characteristics of this material are suggested. A material with a large magnetostriction can be used to provide strain in this material internally either by making a particulate composite or a multilayered composite. Cobalt ferrite has been known to have a large magnetostrictive coefficient. Combining the piezoresistive effects in Barium strontium titanate and the magnetostriction in Cobalt ferrite, a new material with enhanced piezoresistive properties can be discovered.

We have proposed an idea for a multilayered composite material for extremely large piezoresistive response. Lanthanum doped (Ba,Sr)TiO<sub>3</sub> and CoFe<sub>2</sub>O<sub>4</sub> powders were synthesized by the calcination at 1000°C for 2 hrs and 6 hrs respectively. The X-ray diffraction patterns are shown in Fig. 9.1. The two powders were then pressed in a die layer by layer and co-sintered at 1300°C for 5 hrs. An optical microscopic image of the sintered sample is shown in Fig. 9.2. A schematic diagram showing the response of

the material under magnetic field is shown in Fig. 9.3. The material was tested for magneto-electric behavior. The variation magneto-electric coefficient with dc bias and frequency is shown in Fig. 9.4. The magnitude of the magneto-electric coefficient was found to be quite low, and the material is found to show high dielectric loss.

### 9.2 Problems associated with LSMO-partially stabilized ZrO<sub>2</sub> composite

There are many problems associated with the LSMO-partially stabilized composite, which has been synthesized and studied in this research. They are as described below:

- (1) The resistivity of the material is too high around  $8.5 \times 10^{10} \Omega\text{cm}$  to be utilized practically for force sensing applications and a suitable composition where percolation conduction can occur needs to be found.
- (2) There is an ambiguity in the observed piezoresistance behavior. The material showed extremely large changes in resistance of the order of 200%. But the results need to be verified.
- (3) The mechanism of formation of the nanoporous surface layer and a precise determination of the elemental composition and crystal structure of the phases needs to be done.
- (4) The material needs to be studied more for the effect of compositional variation with regard to LSMO content and the amount of CeO<sub>2</sub> used to stabilize zirconia.
- (5) The capacitive properties of the material needs to be verified.
- (6) The composite possesses excellent strength with no inherent porosity and the exact value of the compressive modulus of this material with ASTM standards needs to be found.

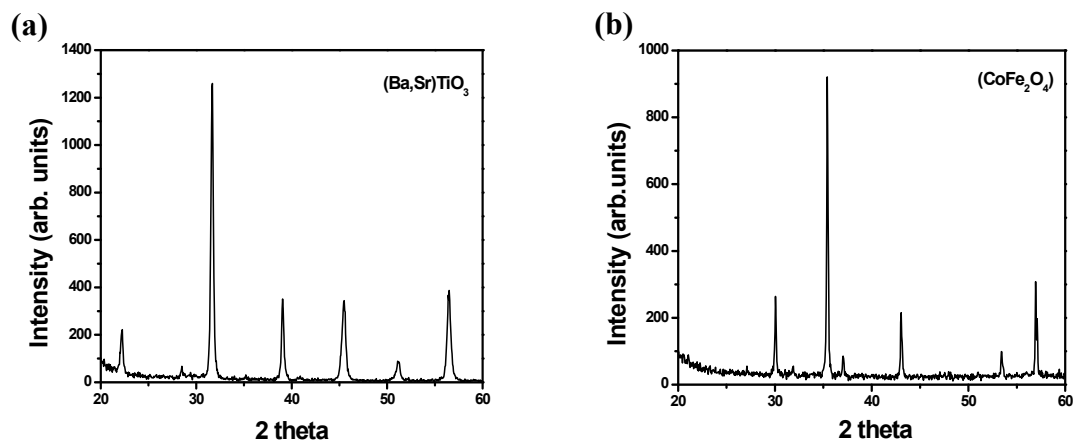


Figure 9.1 (a) La-doped (Ba,Sr)TiO<sub>3</sub> after calcination at 1000°C for 2 hrs and (b) CoFe<sub>2</sub>O<sub>4</sub> after calcination at 1000°C for 6 hrs.

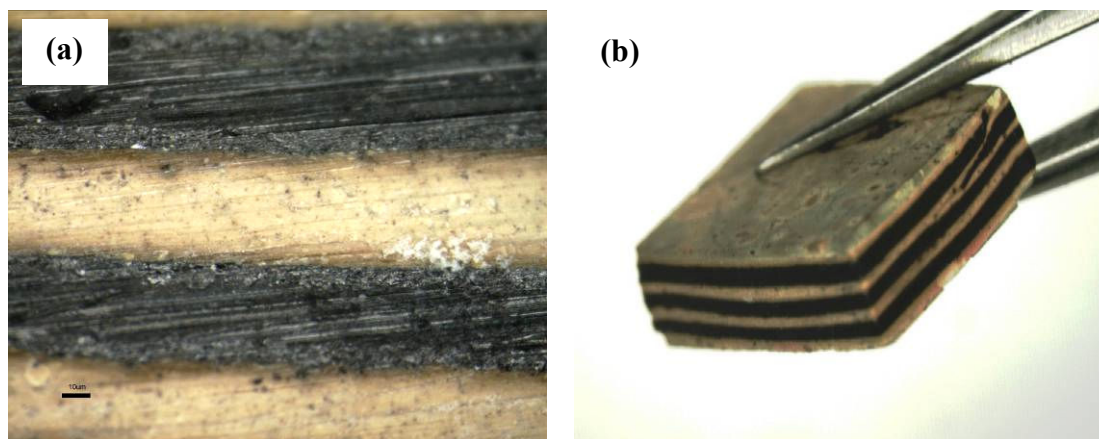


Figure 9.2 (a) and (b) Multilayered (Ba,Sr)TiO<sub>3</sub> – CoFe<sub>2</sub>O<sub>4</sub> composite co-sintered at 1300°C for 5 hrs.



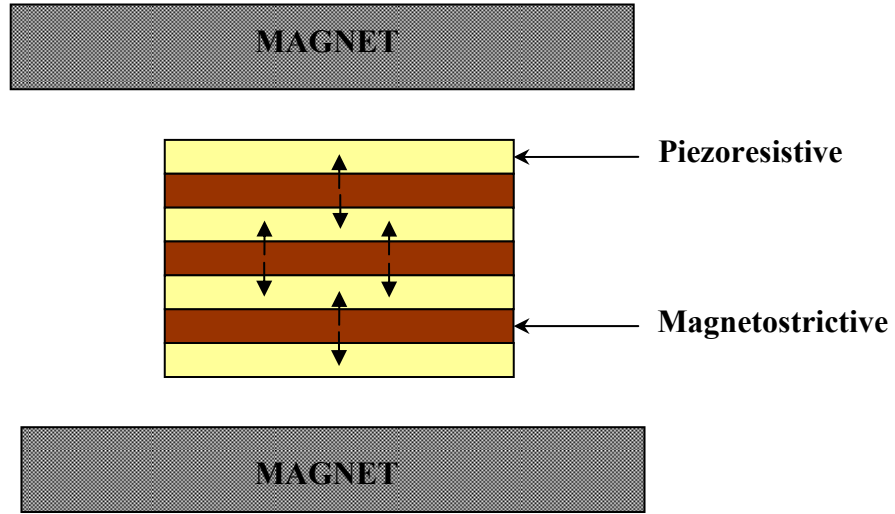


Figure 9.3 Schematics of the multilayered (Ba,Sr)TiO<sub>3</sub> – CoFe<sub>2</sub>O<sub>4</sub> composite.

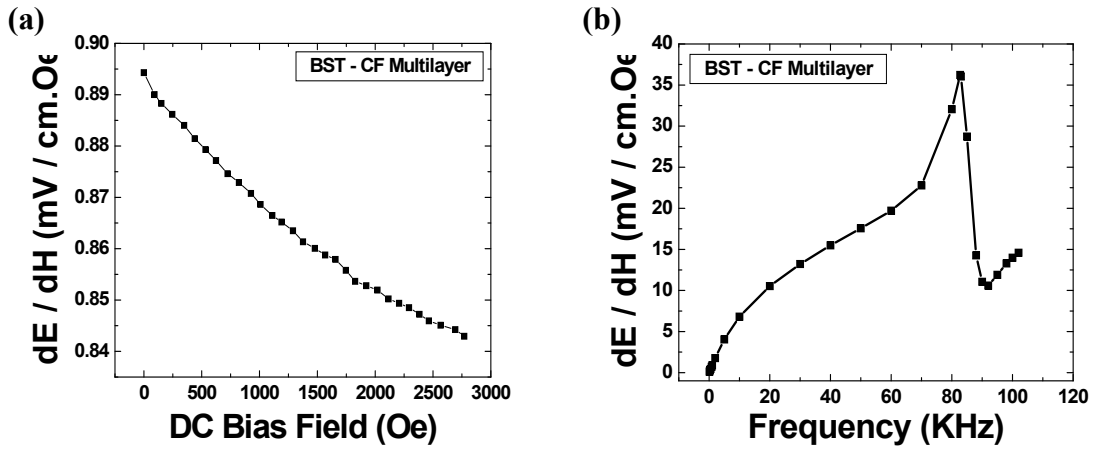
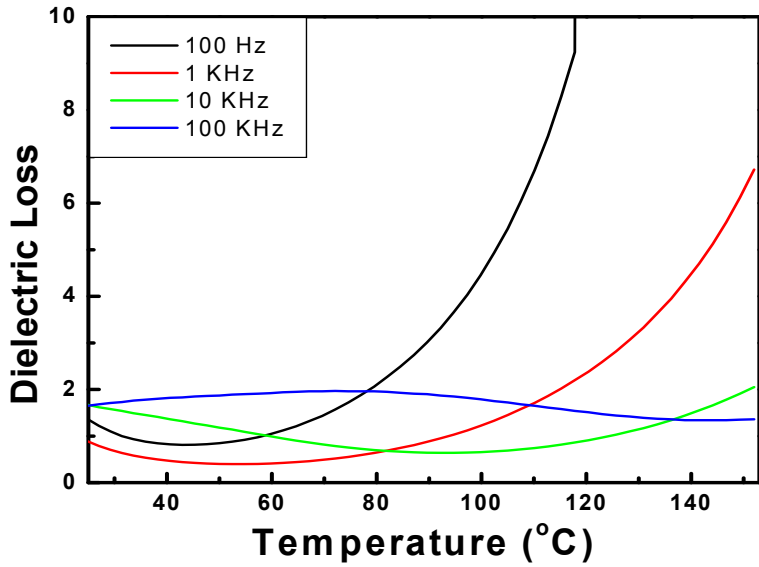
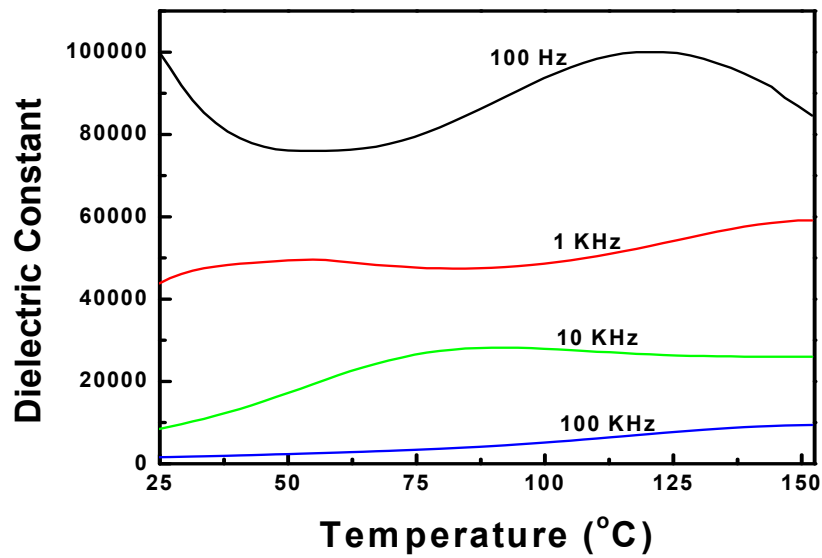


Figure 9.4 (a) Magnetolectric coefficient vs dc bias and (b) frequency for the BST-CF composite.



(a)



(b)

Figure 9.5 (a) Dielectric loss vs temperature and (b) dielectric constant vs temperature curves for BST-CF multilayer composite at different frequencies.

- (7) The temperature characteristics of the composite with respect to resistivity change needs to be studied.

### 9.3 Force sensor design modifications

The force sensor designed in this research is a first generation prototype demonstrating the capability of the 5 mol% Nb-modified  $\text{La}_{0.8}\text{Sr}_{0.2}\text{MnO}_3$  in force sensing applications. Significant improvements can be made in the present design or new design can be made to effectively use this material as a force sensor. The following points need to be considered for the future improvements:

- (1) The piezoresistive coefficient of the material is found to be maximum under a uniaxial stress, so the new design incorporating a mechanism to transmit a complete uniaxial stress can be made.
- (2) The effect of sample geometry on the sensitivity can be verified. A multilayer stack-type structure can be utilized using very thin layers of the bulk piezoresistive sensing material, or a ring type sensing element can be used as shown in Fig. 9.6.
- (3) A precise wheatstone bridge module can be used along with a signal conditioning chip to get a highly accurate and less temperature dependent output from the sensor.
- (4) The size of the sensor can be significantly reduced with the design and circuitry aspects.
- (5) An external wheatstone bridge completion module can be used to eliminate compensation problems. (Appendix D)

#### 9.4 Oxygen gas sensor modifications

The gas sensor design used in this research work is a basic design of an oxygen sensor, with the oxygen sensing element working in a limiting current mode. This design can further be improved by eliminating the use of a reference gas. The oxygen sensor shown in Fig. 9.7 incorporates a method where the same oxygen sensing element can be used as an oxygen pump, with a diffusion barrier <sup>[52, 53]</sup>. The pump gauge is supplied an external voltage and when in operation, it pumps oxygen into an internal volume formed by the pump gauge and the measuring gauge. This eliminates the use of a reference gas, as a reference gas may not be available in all circumstances. Proper use of glass or gold seals is suggested to prevent any leakage. The design suggested below can be used to make a miniature oxygen sensor.

#### 9.5 Carbon nanotube- LSMO-ZrO<sub>2</sub> multifunctional composites

The multifunctional properties of multiwalled and single walled carbon nanotubes have previously been reported. Carbon nanotubes offer a wide scope in imparting multifunctional properties when incorporated in a composite material <sup>[54, 55]</sup>. The semiconducting and metallic behavior of carbon nanotubes based on the structure has been reported in the past decade. The carbon nanotubes have been found to possess piezoresistive properties <sup>[18]</sup>. The carbon nanotubes are known to have extremely high strength, with tensile strength near about 63 GPa, as compared to high carbon steel of 1.2 GPa, and an elastic modulus of the order of 1 TPa. Such high strength combined with high toughness, along with multifunctional properties; make them a promising candidate for use in composite materials.

Here, we suggest a new idea, the carbon nanotubes can be dispersed in the multifunctional ceramic composite material studied in this research, to form a multifunctional material which can improve the piezoresistive properties of the composite significantly and at the same time will improve its strength. A schematic of this idea is shown in Fig. 9.8.

### 9.6 Thin film $\text{La}_{0.8}\text{Sr}_{0.2}\text{MnO}_3$ force sensors

The piezoresistive  $\text{La}_{0.8}\text{Sr}_{0.2}\text{MnO}_3$  sensing element used in this research work is based on the use of a bulk ceramic material for the fabrication of a force sensor. However, use of this material in the form of thin film MEMS piezoresistive force sensor, can significantly improve the sensitivity of the fabricated device. A design similar to the typical MEMS pressure sensor shown in figure for silicon micro-machined pressure sensor can be used to make a thin film LSMO force sensor. The LSMO thin films can be sputtered on a silicon substrate to form a diaphragm. Thin film piezoresistors of LSMO can then be arranged in a wheatstone bridge arrangement. Alternatively, a cantilever beam structure can also be made. An example of a thin film piezoresistive force sensor is shown in Fig. 9.9 <sup>[56]</sup>. Thin film LSMO-ZrO<sub>2</sub> composite force sensor can result in a highly robust as well as a highly sensitive force sensor, with extremely small size, suitable for automotive applications.

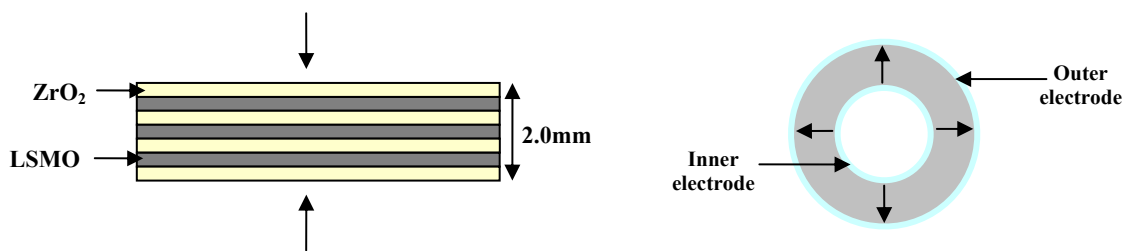


Figure 9.6 Sample geometry modifications, (a) multilayered and (b) ring type structure.

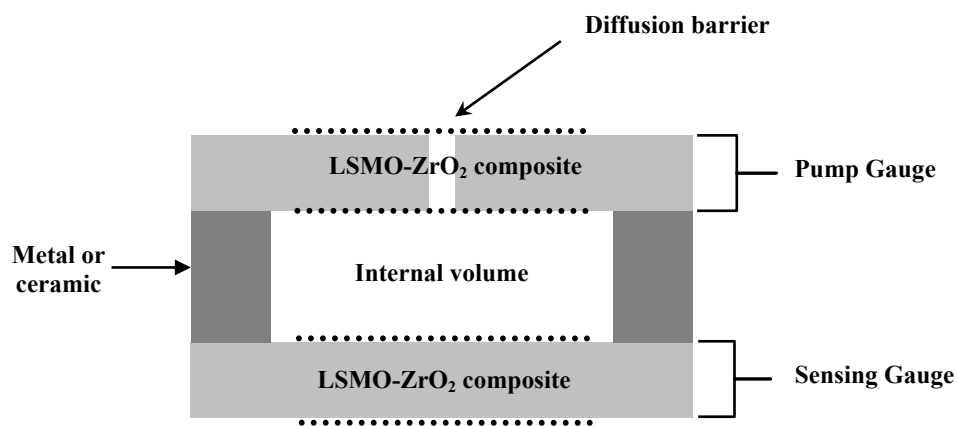


Figure 9.7 Oxygen sensor design with an internal volume.

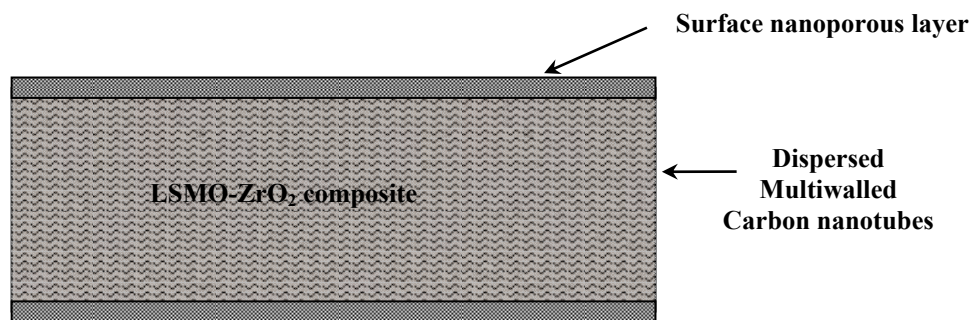


Figure 9.8 Carbon-nanotube LSMO- $ZrO_2$  multifunctional composites.

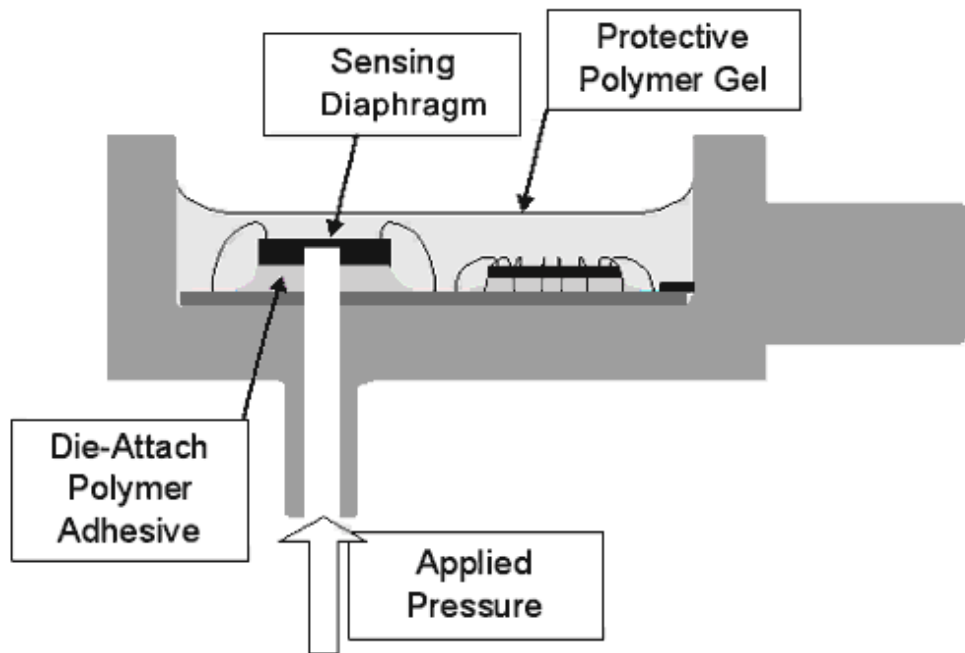


Figure 9.9 Piezoresistive LSMO thin film force sensor design example <sup>[56]</sup>.

## APPENDIX A

### AUTOMOTIVE FORCE AND GAS SENSOR INFORMATION



Table 7 Off-the-shelf force sensors available from various companies.












COMPANY	WEBSITE LINK	FORCE SENSOR TYPE
HoneyWell	<a href="http://content.honeywell.com/sensing/prodinfo/force/">http://content.honeywell.com/sensing/prodinfo/force/</a>	
Tekscan Inc.	<a href="http://www.tekscan.com/flexiforce/flexiforce.html">http://www.tekscan.com/flexiforce/flexiforce.html</a>	
Omega	<a href="http://www.omega.com/pressure/psc.html">http://www.omega.com/pressure/psc.html</a>	
Transducer Techniques	<a href="http://www.transducertechniques.com/Load-Cells-Force-Sensors.cfm">http://www.transducertechniques.com/Load-Cells-Force-Sensors.cfm</a>	
Cooper Instruments	<a href="http://www.cooperinstruments.com/">http://www.cooperinstruments.com/</a>	
PCB Piezotronics Inc.	<a href="http://www.pcb.com/">http://www.pcb.com/</a>	
Futek	<a href="http://www.futek.com/">http://www.futek.com/</a>	
Kistler	<a href="http://www.kistler.com/do.content.us.en-us?content=KistlerCountryHome">http://www.kistler.com/do.content.us.en-us?content=KistlerCountryHome</a>	
SensorOne	<a href="http://sensorone.com/AE801_Home.asp">http://sensorone.com/AE801_Home.asp</a>	

Table 8 Force Sensor design/ construction/principle information links.

		<p><a href="http://www.davidson.com.au/products/force/pcb/theory/force-theory.asp">http://www.davidson.com.au/products/force/pcb/theory/force-theory.asp</a></p>
	<p><a href="http://www.b-tek.com/digitalloadcell.htm">http://www.b-tek.com/digitalloadcell.htm</a></p>	
	<p><a href="http://sensorone.com/AE801_Home.asp">http://sensorone.com/AE801_Home.asp</a></p>	
	<p><a href="http://www.dlr.de/rm/Desktopdefault.aspx/tabid-426/569_read-78/">http://www.dlr.de/rm/Desktopdefault.aspx/tabid-426/569_read-78/</a></p>	
	<p><a href="http://www.sensorland.com/HowPage005.html">http://www.sensorland.com/HowPage005.html</a></p>	

Table 9 Commercially available automotive and other gas sensors.

COMPANY	WEBSITE LINK	GAS SENSOR TYPE
HIFLO Fuel Injection	<a href="http://www.hiflo.com.au/oxygen_sensors.cfm">http://www.hiflo.com.au/oxygen_sensors.cfm</a>	
DELPHI CORP.	<a href="http://www.delphi.com/manufacturers/auto/sensors/et/switchingoxy/">http://www.delphi.com/manufacturers/auto/sensors/et/switchingoxy/</a>	
DELPHI CORP.	<a href="http://www.delphi.com/manufacturers/auto/sensors/et/widerange/">http://www.delphi.com/manufacturers/auto/sensors/et/widerange/</a>	
alphasense	<a href="http://www.alphasense.com/alphasense_sensors/g_series_oxygen_sensors.html">http://www.alphasense.com/alphasense_sensors/g_series_oxygen_sensors.html</a>	
alphasense	<a href="http://www.alphasense.com/alphasense_sensors/co2_carbon_dioxide_sensors.html">http://www.alphasense.com/alphasense_sensors/co2_carbon_dioxide_sensors.html</a>	
SNG sensors	<a href="http://www.sngsensors.com/home.html">http://www.sngsensors.com/home.html</a>	
Dynamic Ceramic	<a href="http://www.dynacer.com/oxygen_sensors.htm">http://www.dynacer.com/oxygen_sensors.htm</a>	
Honeywell	<a href="http://content.honeywell.com/sensing/prodinfo/oxygen/">http://content.honeywell.com/sensing/prodinfo/oxygen/</a>	

## APPENDIX B

### SILICON MEMS AS FORCE SENSORS

### B.1 Silicon MEMS as pressure or force sensors

Pressure micro-sensors were the first type of silicon micro-machined sensors to be developed in the late 1950s and early 1960s. Consequently, the pressure micro-sensors represent probably the most mature silicon micromechanical device with widespread commercial availability today. The largest market is undoubtedly the automotive. The growth in the world market for automotive silicon micro-machined sensors from 1989 to 1999 is shown in table 10 <sup>[59]</sup>. The two most important silicon sensors are the pressure and micro-accelerometer sensors, with substantial growth expected for gyrometers.

The two most common methods to fabricate pressure micro-sensors are the bulk and surface micromachining of polysilicon. The basic working principle of a silicon micro-sensor can be piezoresistive or capacitive. A schematic construction of the piezoresistive silicon sensor is shown in Fig. B.1. The deflection in the diaphragm can be measured using piezoresistive strain gauges located in the appropriate region of maximum strain. The strain gauges are usually made from doped silicon and are designed in pairs with a readout circuit in the form of a wheatstone bridge. The change in the strain can be related to the applied pressure ( $P-P_0$ ) and stored in a look-up table. The following relationship describes the relationship between piezoresistive coefficient of the diaphragm material and applied pressure:

$$V_{\text{out}} \propto \Delta R \propto \Pi (P-P_0)$$

The piezoresistive coefficient ( $\Pi_{44}$ ) is typically +138.1 pC/N.

The arrangement of a single crystal silicon pressure sensor with a capacitive pickup is shown in Fig. B.2 in this case a capacitive bridge can be formed with two reference capacitors and the voltage output is related to the deflection of the membrane  $\Delta x$  and hence the applied pressure  $(P-P_0)$ .

$$V_{\text{out}} \propto \Delta C \propto \Delta x \propto (P-P_0)$$

However there are merits and demerits of capacitive against the piezoresistive pressure sensors as summarized in table 11.

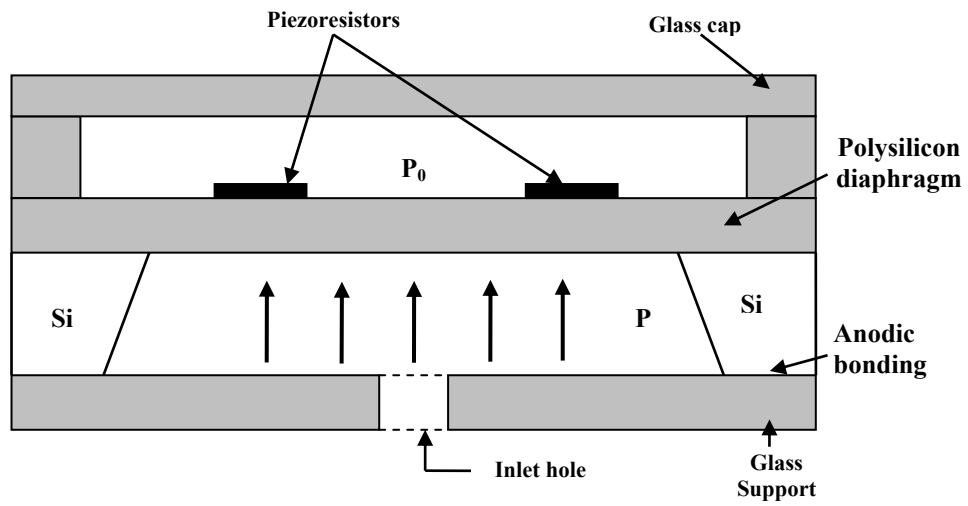


Figure B.1 Piezoresistive polysilicon pressure sensor <sup>[59]</sup>.

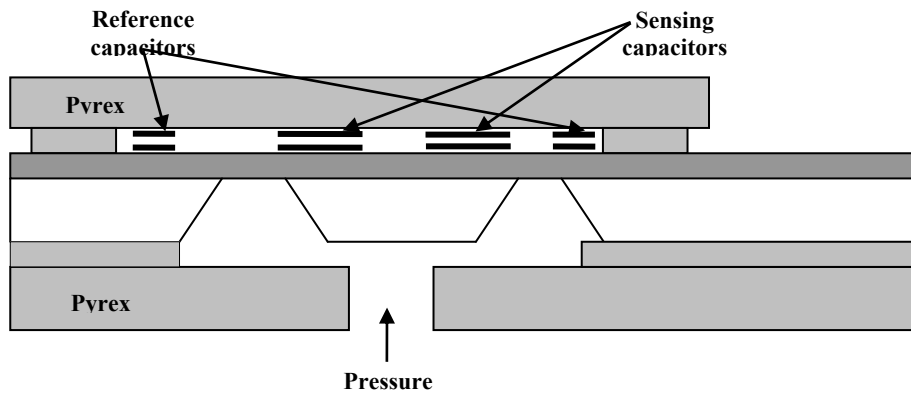


Figure B.2 Capacitive (single crystal silicon) pressure sensor <sup>[59]</sup>.

Table 10 Worldwide growth for automotive silicon micromachined sensors (from Sullivan1993) <sup>[59]</sup>.

Year	Revenue (MEuro)	Growth-rate (%)	Year	Revenue (MEuro)	Growth-rate (%)
1989	175	-	1995	376	21
1990	283	62	1996	463	23
1991	323	14	1997	564	22
1992	321	-1	1998	679	20
1993	285	-11	1999	804.2	18
1994	312	10			

Table 11 Relative merits and demerits of capacitive and piezoresistive silicon pressure sensors <sup>[59]</sup>.

	Advantages	Disadvantages
<b>Capacitive</b>	More sensitive-polysilicon Less temperature-sensitive More robust	Large piece of silicon for bulk micromachining Electronically more complicated Needs integrated electronics
<b>Piezoresistive</b>	Smaller structure than bulk capacitance No need for integration Simple transducer circuit	Strong temperature dependence Piezo-coefficient depends on the doping level



## APPENDIX C

### PIEZORESISTIVITY MEASUREMENT SYSTEM

### C.1 Piezoresistivity measurement system

A lab-scale automatic Piezoresistivity system is described here. The measurement system incorporates a stepper motor mechanism to precisely apply and control the load. A precision control stepper motor with micro-controller can produce a  $1.8^\circ$  rotation of the motor shaft. The rotational motion of the motor shaft is converted to linear motion with the help of spur gears and acme screw combination. As shown in Fig. C.1 the mechanical setup ensures a complete uniaxial load on the sample. The spur gears used in this system are a 10:1 gear ratio and increase the motor torque significantly. Depending on the gear ratio and the stepper motor torque rating, a high load application system can be made.

The stepper motor is controlled by a micro-controller and the load is measured by a load cell of 1000 lb. capacity. Alternatively, a load cell of a desired capacity can be used, depending on the maximum load intended from the system. The resistance of the samples is measured using a digital multimeter as described in App. F. The whole setup including the load cell, the microcontroller, and the digital multimeter are connected to a data acquisition system controlled by Labview<sup>®</sup> programming. With proper programming the system can automatically measure and record the output of the desired experiment. A block diagram of the measurement setup is shown in Fig. C.2.

This home built piezoresistivity measurement system can turn out to be a cheap option for uniaxial load application, for almost any measurement requiring a controlled application of uniaxial load and automatic data acquisition.

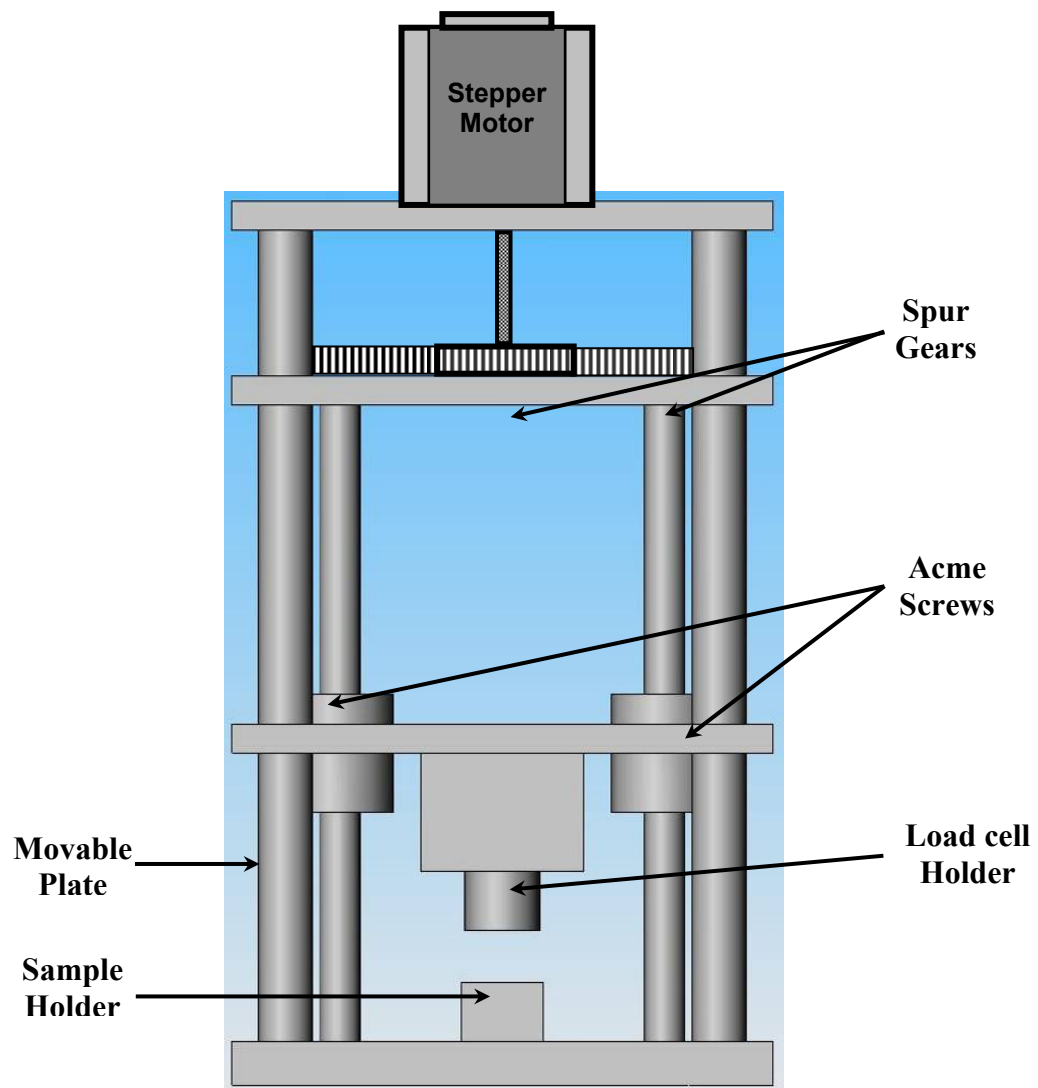


Figure C.1 Lab scale automatic piezoresistivity measurement system design.

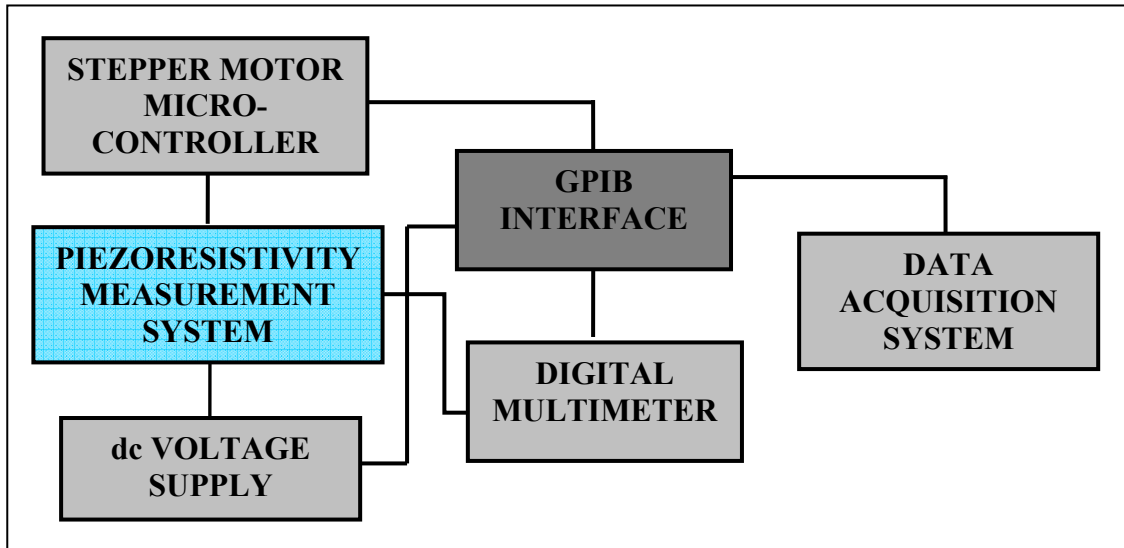


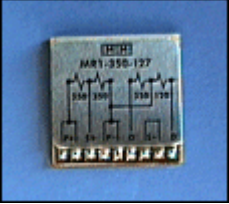
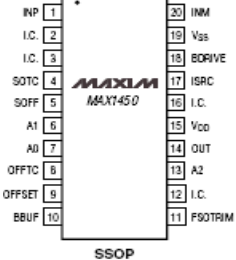



Figure C.2 Block diagram for the automatic piezoresistivity measurement system.

APPENDIX D

ELECTRONIC COMPONENTS

Table 12 List of electronic components for piezoresistive force sensors.

ELECTRONIC COMPONENT	PART No./STOCK No.
	<p><b>Make:</b> Caddock  <b>Type:</b> thick film resistor  <b>Mfr Part#:</b> MP850-2.00K-1%  <b>Allied Stk#:</b> 524-4400  <b>Order website:</b>  <a href="http://www.alliedelec.com/default.asp">http://www.alliedelec.com/default.asp</a></p>
	<p><b>Make:</b> Bourns  <b>Type:</b> cermet, multiturn, potentiometer  <b>Mfr Part#:</b> 3296W-1-102  <b>Allied Stk#:</b> 754-3112  <b>Order website:</b>  <a href="http://www.alliedelec.com/default.asp">http://www.alliedelec.com/default.asp</a></p>
	<p><b>Make:</b> Vishay  <b>Type:</b> Bridge Completion Module  <b>Mfr. Part# :</b> MR-350-127  <b>Order website:</b>  <a href="http://www.vishay.com/">http://www.vishay.com/</a></p>
	<p><b>Make:</b> Maxim® Dallas.  <b>Type:</b> Signal conditioning for piezoresistive force sensors  <b>Mfr. Part#:</b> MAX1450  <b>Order website:</b>  <a href="http://www.maxim-ic.com/">http://www.maxim-ic.com/</a></p>
	<p><b>Make:</b> National Semiconductor  <b>Type:</b> analog to digital convertor  <b>Mfr. Part#:</b> ADC0831  <b>Order website:</b>  <a href="http://www.national.com/">http://www.national.com/</a></p>

APPENDIX E  
CHEMICALS USED FROM ALFA AESAR

Alfa Aesar

26 Parkridge Road

Ward Hill, MA 01835,USA.

Telephone: 1-978-521-6300

Website: [www.alfa.com](http://www.alfa.com)

Customer Sales and Customer Service

Toll-free phone: 1-800-343-0600.

Table 13 List of chemicals obtained from Alfa Aesar.

<b>MATERIAL</b>	<b>CAS NO.</b>	<b>LOT NO.</b>	<b>STOCK NO.</b>
La <sub>2</sub> O <sub>3</sub> (99.9% REO)	1312-81-8	P2594	11272
Ce <sub>2</sub> O <sub>3</sub> (99.5% REO)	1306-38-3	A24M0F	12925
SrCO <sub>3</sub>	1633-05-2	D21P05	33392
ZrO <sub>2</sub>	1314-23-4	E17Q11	11395
MnO <sub>2</sub> (99.9% metal basis)	1313-13-9	L08P06	42250
Nb <sub>2</sub> O <sub>5</sub> (99.5% metal basis)	1313-96-8	L15N01	11365
Li <sub>2</sub> CO <sub>3</sub> (99% metal basis)	554-13-2	E27P27	13418
Bi <sub>2</sub> O <sub>3</sub> (99% metal basis)	1304-76-3	H14N03	12230
CuO	1317-38-0	J02L06	12299



## APPENDIX F

### MULTIMETER AND ELECTROMETER

(i) Agilent 34410A Digital Multimeter, 6½ digit high performance.

Website information link:

<http://www.home.agilent.com/agilent/product.jsp?cc=US&lc=eng&ckey=1000001295:epsg:pro&nid=-536902435.536880933.00&id=1000001295:epsg:pro>

Contact info:

Agilent Technologies (USA)

Service and technical Support

Toll-free: 1(800)829-4444



Figure F.1 Agilent 34410A 6½ digit, high performance digital multimeter.

(ii) KEITHLY Model 6517A Electrometer/High resistance meter.

Contact info:

Keithly Instruments Inc.

28775 Aurora Road

Cleveland, Ohio 44139

Phone: 1-440-248-0400

Toll- free: 1-800-552-1115

<http://www.keithley.com>



Figure F.2 KEITHLY Model 6517A Electrometer / High resistance meter.

## REFERENCES

- [1] N.Q. Minh, T. Takahashi, *Science and Technology of Ceramic Fuel Cells*, Elsevier, New York, 1995.
- [2] T. Tsai, S.A. Barnett, *Solid State Ionics*, **93**, 207 (1997).
- [3] A. J. McEvoy, *Solid State Ionics*, **132**, 159 (2000).
- [4] S. Jin, T.H. Tiefel, M. McCormack, R.A. Fastnacht, R. Ramesh, L.H. Chen, *Science*, **264**, 413 (1994).
- [5] C. N. R. Rao, R. Mahesh, A. K. Raychaudhuri, and R. Mahendiran, *J. Phys. Chem. Solids*, **59**, 487 (1998).
- [6] R. M. Kusters, J. Singleton, D. A. Keon, R. M. Greedy, and W. Hayes, *Physica B*, **155**, 362 (1989).
- [7] H. L. Ju, C. Kwon, Q. Li, R. L. Greene, and T. Venkatesan, *Appl. Phys. Lett.* **65**, 2108 (1994).
- [8] B. X. Huang, Y.-H. Liu, X. Yuan, C.-J. Wang, R.-Z. Zhang, L.-M. Mei, “*Journal of Magnetism and Magnetic Materials*, **280**, 176-183 (2004).
- [9] R. V. Wandekar, B. N. Wani, and S. R. Bharadwaj, *Materials Letters*, **59**, 2799-2803 (2005).
- [10] S. Kuharuangrong, T. Dechakupt, P. Aungkavattana, *Materials Letters*, **58**, 1964-1970 (2004).

- [11] V. Sharma, M.R. Hossu, W.H. Lee, A.R. Koymen, S. Priya, *Journal of Materials Science*, (submitted).
- [12] V. Sharma, M. R. Hossu, W. H. Lee, A. R. Koymen, and S. Priya, *Appl. Phys. Lett.* **89**, 202902 (2006).
- [13] V. Sharma, J. Jiang, M.R. Hossu, A.R. Koymen, S. Priya, *Applied Physics Letters*, (submitted).
- [14] C. S. Smith, *Phys. Rev.*, **94**(42), (1954).
- [15] H. A. Sauer, S. S. Flaschen, and D.C.Hoesterey, *J. Am. Ceram. Soc.*, **42**, 363 (1959)
- [16] C. Canali, D. Malavasi, B. Mortren, M.Prudenziati and A. Taroni, *J. Appl. Phys.*, **51**, 3282 (1980)
- [17] J. L. Davidson, W.P. Kang, Y. Gurbuz, K.C. Holmes, L.G. Davis, A. Wisitsorarat, D.V. Kerns, R.L. Eidson, and T. Henderson, *Diamond Related Mater.*, **8**, 1741-1747 (1999).
- [18] D. A. Gordon, S. Wang, and D. D. L. Chung, *Composite Interfaces*, **11**, 95-103 (2004).
- [19] R. E. Newnham, “*Properties of Materials*”, Oxford University Press, New York, (2005).
- [20] N. Zhang, W.P. Ding, Z.B. Guo, W. Zhong, D.Y. Xing, Y.W. Du, G. Li, Y. Zheng, *Z. Phys. Rev. B*, **102**, 461-465 (1997)
- [21] H. Makino, M. Asai, S.Tajima, N. Kamiya, *R&D Review of Toyota CRDL* **37**(3), 67-70 (2002).

- [22] Y. Moritomo, A. Asamitsu, and Y. Tokura, *Phys. Rev. B*, **51**, (1995).
- [23] <http://www.wmi.dadw.de/groups/spinpole/> (last viewed 12/17/2006).
- [24] P. Majewski, L. Epple, M. Rozumek, H. Schluckwerder, and F. Aldinger, *J. Mater. Res.*, **15**, 1161-1166 (2000).
- [25] Y. Du, M. A. Yashima, T. Koura, M. Kakihana, and M. Yoshimura, *Calphad*, **20**, 95-108 (1996).
- [26] E. Dagotto, T. Hotta, and A. Moreo, *Physics Reports*, **344**, (2001), 1-153.
- [27] A. Urushiba, Y. Moritomo, T. Arima, A. Asamitsu, G. Kido, Y. Tokura, *Physical Review B*, **51**, 14103-14109 (1995).
- [28] A. K. Sahu, A. Ghosh, A.K. Suri, P. Sengupta, and K. Bhanumurthy, *Materials Letters*, **58**, 3332-3336 (2004).
- [29] N. Zhang, W. Ding, Z. Guo, W. Zhong, D. Xing, and Y. Du, "Giant uniaxial piezoresistance in GMR perovskite  $\text{La}_{0.85}\text{Sr}_{0.15}\text{MnO}_3$ ", *Physics Letters A*, **219**, 319-323 (1996).
- [30] A. Ghosh, A. K. Sahu, A. K. Gulnar and A. K. Suri, *Scripta Materialia*, **52**, 1305-1309 (2005).
- [31] D. Grossin, J. G. Noudem, *Solid State Sciences*, **6**, 939-944 (2004)
- [32] D. L. Meixner, R. A. Cutler, *Solid State Ionics*, **146**, 273-284 (2002).
- [33] J.G. Noudem, A. Hassini, M. Gervais, F. Gervais, *Solid State Sciences*, **5**, 1001-1007 (2003)
- [34] M. G. Harwood, *Proc. Phys. Soc.*, **68**, 586-592 (1955).

- [35] S. C. Sharma, N. M. Gokhale, R. Dayal, and R. Lal, *Bulletin of Material Science*, **25**, 15-20 (2000).
- [36] G. M. Whitesides, J. P. Mathias, C.T. Seto, *Science*, **254**, 1312-1319 (1991).
- [37] G. M. Whitesides, B. Grzybowski, *Science*, **295**, 2418-2421 (2002).
- [38] J. Liu, A.Y. Kim, L. Q. Wang, B. J. Palmer, Y. L. Chen, P. Briunsma, B. C. Bunker, G. J. Exarhos, G. L. Graff, P. C. Reiki, G. E. Fryxell, J. W. Virden, B. J. Tarasevich, and L. A. Chick, *Advances in Colloid and Interface Science*, **69**, 131-180 (1996).
- [39] L. E. Depero, and M. L. Curri, *Current Opinion in Solid State and Material Science*, **8**, 103-109 (2004).
- [40] A. J. Moulson, and J. M. Herbert, *Electroceramics*, 2<sup>nd</sup> ed., John Wiley & Sons Inc., Hoboken, NJ, (2003).
- [41]] V. R. Mastelaro, V. Briois, D. P. F. De Souza, C. L. Silva, *J. Eur. Ceram. Soc.* **23**, 273 (2003).
- [42] C. R. Foschini, D. P. F. Souza, P. I. F. Paulin, J. A. Varela, *J. Eur. Ceram. Soc.* **21**, 1143 (2001).
- [43] L. Li, O. V. Der Biest, P. L. Wang, J. Vleugels, W.W. Chen, S.G. Huang, *J. Eur. Ceram. Soc.*, **21**, 2903-2910 (2001).
- [44] L. Z. -an, X. J. -zhong, Z. Feng, *Transactions of Nonferrous Metals Society of China*, **16**, s82-s87 (2006).
- [45] K.R. Sridhar, J. A. Blanchard, *Sensors and Actuators B*, **59**, 60-67 (1999).

- [46] A. D. Brailsford, E. M. Logothetis, *Sensors and Actuators B*, **52**, 195-203 (1998).
- [47] F. Garzon, I. Raistrick, E. Brosha, R. Houlton, B. W. Chung, *Sensors and Actuators B*, **50**, 125-130 (1998).
- [48] A. Q. Pham, R. S. Glass, *Electrochimica Acta.*, **43**, (18) 2699-2708 (1998).
- [49] A. D. Brailsford, M. Yussouff, E. M. Logothetis, *Sensors and Actuators B*, **44**, 321-326 (1997).
- [50] A. G. Mortimer, G. P. Reed, *Sensors and Actuators B*, **24-25**, 328-335 (1998).
- [51] H. -D. Weimhofer, *Solid State Ionics*, **75**, 167-178 (1995).
- [52] M. Benammar, *IEEE Sensors Journal*, **4**, (1) (2004).
- [53] I.S. Metcalfe, *Solid State Ionics*, **134**, 51-58 (2000).
- [54] E. Munoz, A.B. Dalton, S. Collins, M. Kozlov, J. Razal, J. N. Coleman, B. G. Kim, V. H. Ebron, M. Selvidge, J. P. Ferraris, R. H. Baughman, *Advanced Engineering Materials*, **6**(10), 801-804 (2004).
- [55] A. B. Dalton, S. Collins, E. Munoz, J. M. Razal, V. H. Ebron, J. P. Ferraris, J. N. Coleman, B. G. Kim, R. H. Baughman, *Nature*, **423**(6941), 703 (2003).
- [56] <http://www.maxim-ic.com/an762>, Application Note 762, (last viewed on 12/17/06)
- [57] A. Amin, *Phys. Rev. B*, **39**, 4350 (1989). Erratum *Phys. Rev. B*, **41**, 4787 (1990).
- [58] A. Amin, and E.K. Akdogan, *A tutorial Presentation for the IEEE- Ultrasonics, Ferroelectrics & Frequency Control Society.*”



- [59] J. W. Gardner, V. K. Varadan, and O. O. Awadelkarim, “*Microsensors, MEMS, and Smart Devices*”, John Wiley & Sons, Inc., New York, NY (2001).

## BIOGRAPHICAL INFORMATION

The author received his Bachelor of Engineering degree in Metallurgical Engineering, from Punjab Engineering College, India, in May, 2004. He received his Master of Science (M.S.) degree in Materials Science and Engineering, from The University of Texas at Arlington, Texas, USA, in December, 2006. The author has worked extensively in the field of materials synthesis and characterization, especially multifunctional ceramic materials and their applicability in devices. In future, the author would like to work towards the development and discoveries of new materials for space applications and for general public use.